Certificate

This is to certify that the thesis work entitled "**Digital Correlation Receivers For Radio Telescopes"** carried out by Mr. **Girish B. S**., USN **1RR03MEN02**, a bona-fide student of **Raman Research Institute, Bangalore,** in partial fulfillment for the award of **Master of Science (Engg.) by Research** in **Electrical Engineering** of the Visvesvaraya Technological University, Belgaum, during the year **2009**, to the best of my knowledge, has not been submitted by me elsewhere for the award of any degree and is not a repetition of the work carried out by others.

(B. S. Girish)
Candidate

To the best of my knowledge, the above statement made by the candidate Mr**. B. S. Girish** with university seat number **1RR03MEN02** is true.

(Prof. N. Udaya Shankar)
Guide

(Prof. Ravi Subrahmanyan)
(**Head of the Institution**)

Abstract

Radio astronomy is a branch of astronomy that deals with the study of radio emission from celestial sources. A radio astronomer studies radio emissions from the sky using a radio telescope- a single-dish or an array of antennas. Radio astronomers are interested in measuring the intensity of radio emission from the sky as a function of the angular coordinates in the sky, frequency of emission, polarization, and time. Since astronomical signals are extremely weak in nature, deeply buried in noise, they are extracted using the powerful correlation technique. In this thesis, we are concerned with measurement of intensity as a function of frequency of emission and angular coordinates in the sky leading to the two primary objectives of the thesis:

The Raman Research Institute (RRI) operates a 10.4 m radio telescope. This telescope was till recently operating at 6.667 GHz for studying Methanol maser lines emanating from celestial sources in our Galaxy. The front-end is now being upgraded to operate at around 50 GHz. One of the primary objectives of this thesis was to design and develop a general-purpose spectrometer with a capability to process a bandwidth of about 160 MHz (dual polarization) or 320 MHz (single polarization), with provision to trade-off bandwidth for spectral resolution. The primary task of the spectrometer is to carry out spectral-line survey using the RRI 10.4m radio telescope. It was for the first time that an autocorrelation spectrometer capable of processing such a bandwidth was being attempted at RRI. One of the most commonly used spectrometers to measure the intensity of the signal as a function of frequency is the digital autocorrelation spectrometer. Its principle of operation in based on the Wiener-Khinchin theorem which states that the power spectrum of a signal is the Fourier transform of its autocorrelation function. In the first version of the receiver, a wideband spectrometer, capable of processing a bandwidth of 320 MHz with a spectral resolution of about 50 kHz, has been designed, developed, tested and integrated with the 10.4 m radio telescope. The wideband spectrometer downconverts the received radio frequency (RF) signal to a convenient intermediate frequency (IF) signal of bandwidth equal to 40 MHz, centered around 80 MHz. Autocorrelation of the digitized signal is carried out using an Application Specific Integrated Circuit (ASIC) procured from the National Aeronautics and Space Administration (NASA). The ASIC, containing 1024 lags or channels, estimates the autocorrelation function from the signal of interest which has been digitized to a 2-bit, 3-

level format. The spectrometer has provision to trade off bandwidth for improved spectral resolution catering to both broadband and narrowband observations. The spectrometer was tested in the laboratory and was later integrated with other sub-systems at the 10.4 m radio telescope. To validate the spectrometer, test observations of Methanol maser sources were carried out, both in narrow band and broadband observation modes.

In the second version of the receiver, only the correlator unit of the wideband spectrometer was integrated with an analog-to-digital converter (ADC) capable of directly digitizing astronomical signals in the L-band (1 GHz to 2 GHz), thereby, minimizing the number of IF units in the spectrometer. Test observations on astronomical sources were carried out to realize the concept of a spectrometer based on direct digitization of signals up to 1.4 GHz.

Generally, a radio astronomer measures the intensity distribution as a function of angular coordinates by using an array of antennas and a correlation receiver. The fundamental idea behind this is the Fourier transform relationship that exists between the sky radio brightness distribution and the spatial coherence function of the wavefront received by the array of antennas. This theorem, a spatial analogue of the Wiener-Khinchin theorem, is known by the name: van Cittert-Zernike theorem. A correlation receiver measures spatial coherence function at a given spatial separation on the wavefront, sampled by any two antennas of the array. It basically measures one Fourier component of the sky brightness distribution. Thus, by measuring the Fourier components over a wide range of antenna spacings, the sky brightness distribution may be reconstructed with much higher resolution than is possible with a large filled aperture telescope. The Giant Metrewave Radio Telescope (GMRT) - a national facility located 80 km from Pune-is a rotational synthesis instrument consisting of an array of 30 dish antennas with each antenna having a diameter of 45 m. In a rotational synthesis instrument, the rotation of the earth is used to our advantage to sample the wavefront received from celestial sources on various spatial scales. In this scenario, the rotation of the earth gives an effect similar to reconfiguring the antennas by moving them on the ground.

In receiver systems, the signal-to-noise ratio (SNR) increases with increase in bandwidth (β) and integration time (τ). Astronomical observations carried out at GMRT

showed that $\sqrt{\beta\tau}$ improvement was not forthcoming when observed using the existing GMRT receiver chain which could possibly be due to systematics, RFI, cross-talk in the analog signal conditioners and correlators. To study if this limitation can be overcome by digitizing the output of a 50 MHz front-end receiver right at the antenna base, a system to directly digitize and record an RF/IF signal (RRI-DS) of bandwidth ~5.5 MHz, and compute correlations off-line on a computer has been designed, developed, tested and integrated with the GMRT receiver system. Test observations of astronomical sources like Cygnus A and Cassiopeia A have been carried out using two GMRT antennas in interferometric mode. Such an observation, gave a handle on GMRT data at previously unexplored time and frequency structures. This, we believe, gives us a new insight into the data quality.

The first chapter of this thesis gives an introduction to the digital correlation receivers used in radio astronomy. The second chapter describes the design and development of the hybrid wideband spectrometer for spectral-line observations. The results obtained from Methanol maser observations carried out using the wideband spectrometer in narrowband and broadband mode are discussed. This chapter also describes a spectrometer based on direct digitization of signals in the L-band. Chapter 3 describes the design, development, and testing of a direct voltage recording system which was used to digitize and record data right at the antenna base from a two-element interferometer operating at 50 MHz (using two GMRT antennas). Chapter 4 of the thesis describes the integration of the direct voltage recording systems with the GMRT receiver system and the results obtained from test observations carried out to measure the improvement in SNR as a function of bandwidth and integration time. This chapter also explains the data processing steps that have been developed for the above purpose. The results obtained from simultaneous observations carried out using the existing GMRT hardware and GMRT software correlators are compared with those obtained from RRI-DS. Chapter 5 summarizes the work carried out for this thesis.

Acknowledgements

As the work presented in this thesis has benefited from the contributions and support of many individuals, it is a pleasure to thank them.

I thank the Director of Raman Research Institute for giving me an opportunity to both work and pursue my Master's degree programme. It is difficult to overstate my gratitude to my supervisor, Prof. N. Udaya Shankar of the Department of Astronomy and Astrophysics, Raman Research Institute. With his enthusiasm, his inspiration, and his great efforts, especially during the course work, to explain things clearly and simply, has helped me reach this juncture. Throughout my thesis-writing period, he provided constant encouragement, sound advice, and lots of good ideas.

I am greatly indebted to Dr. D. K. Ravindra for initiating me into the world of Digital Signal Processing by providing me an opportunity to work on the development of an autocorrelation spectrometer. I thank Prof. K. S. Dwarakanath for the useful discussions during the 50 MHz project, Prof. A. A. Deshpande for his timely suggestions during the development of the direct voltage recording system for 50 MHz observations at GMRT. I thank Dr. Anish Roshi for giving useful insights on aspects related to high-speed analog-to-digital converters, and Dr. B. Ramesh for insights into Methanol maser observations and need for high-resolution spectrometer.

I thank my colleagues Ananth, Prabu, Som, Srivani, and Raghu for their timely suggestions and all the useful technical discussions during the course work and project work. I specially thank Srivani for all the support extended, and helping me come out triumphant when the chips were down. I take this opportunity to thank my other colleagues at RAL: Krishna Murthy (now with the computer section), Madhavi, Kamini, Kasturi, Manjunath (presently working at Qualcomm), Nagaraj, KBR, GK, Vinod, Vinutha, Sandhya, Arasi, Mamata, Wences Laus, Rishin and others for all the help they've extended. Pep (Peeyush Prasad), thanks a bunch for all the help you've extended during the last few years, especially, in fine-tuning the software related to the 50 MHz data acquisition system using RRI-PLX card.

I profusely thank Mamta for painstakingly generating and collating all the documents exchanged between the University and RRI. I am also grateful to Krishnamaraju K. and his colleagues in the Administration section (Vidya, Marisa, Radha and Raveendran) for helping me with all the University-related paper work.

I extend my sincere gratitude to Dr. Y. M. Patil and his colleagues, especially, Chowdappa, at the Library for supporting me at all times. At the computer section, I thank Jacob Rajan and his colleagues for the help rendered in fixing computer-related issues, especially, those related to data acquisition computers. I thank Sridhar B. for sparing a laptop from the computer section for drafting this thesis.

FFTW is a free collection of fast C routines for computing the Discrete Fourier Transform in one or more dimensions. I thank Matteo Frigo and Steven G. Johnson (at MIT) for their wonderful gesture in making the FFTW package publicly-available as it has been the cornerstone for all my data analysis.

I thank Mr. Attequlla, Gangadhar, Damodar, Durai Chelvan, and their colleagues, especially, Narayan Swamy, Mohan, Gokul and Sunand for making all the necessary fabrications at the workshop.

The job of writing this thesis was made more enjoyable due to the constant encouragement and guidance extended by my good friend and colleague Arvind. He has helped me in organizing my thesis chapter-wise, carefully reviewed chapters, politely pointed out glaring mistakes, and always expanded my vocabulary. I take this opportunity to thank Arvind for all his time and efforts in analyzing the 50 MHz data.

I thank Mrs. Latha Hegde for that important telephonic conversation in which she rightly reminded me of my earlier successes, which was highly contextual.

I thank my **parents, sister**, and **wife** for their never-ending support, encouragement, and their belief in me. Finally, I would like to thank all those people who have directly or indirectly helped me in this endeavor.

Contents

Section-B

3. A Direct Voltage Recording System for 50 MHz Observations at GMRT

4. Results from Test Observations carried out at GMRT

List of Figures

List of Tables

Chapter 1

Chapter 1

Introduction

This chapter begins with a brief introduction to radio astronomy and the nature of signals in radio astronomy. This is followed by a summary of the different types of digital correlation receivers used to process signals form a single-dish radio telescope and multi-element interferometric arrays. The next section describes the two primary objectives of this thesis and its scope of study. Finally, the chapter concludes with the outlay of the thesis.

1.1 Introduction to Radio Astronomy

During the last few decades, astronomical observations at radio wavelengths, ranging from about 1 mm to 10 m, have created a new branch of astronomy called radio astronomy which deals with the study of radio emission from the sky. The older astronomy in the visible spectrum is now called optical astronomy (λ ranging from 0.4 to 0.8 micron). The positions of optical astronomy and radio astronomy in the electromagnetic spectrum coincide with the two principal transparent bands of the earth's atmosphere and ionosphere [1]. Radiations from celestial objects are now being observed over the entire electromagnetic spectrum ranging from radio waves to the extremely short-wave gamma-rays. By carrying out astronomical observations at different wavelengths, which are at times complementary in nature, astronomers can gain a better understanding of the processes at work in the Universe. A radio astronomer studies radio emissions from the sky using a radio telescope. A typical single-aperture radio telescope consists of the following components:

1. A large reflecting surface, usually a paraboloid of revolution (parabolic reflector), which acts as a collector of radio waves.
2. A mechanical mount structure, on which the reflector is fixed with a control system to facilitate pointing of the reflector to different regions of the sky.
3. A sensitive analog signal conditioner and a recording system.

The parabolic reflector is the most commonly used antenna element in which the impinging radio waves from a distant source are brought to focus at a point called the prime

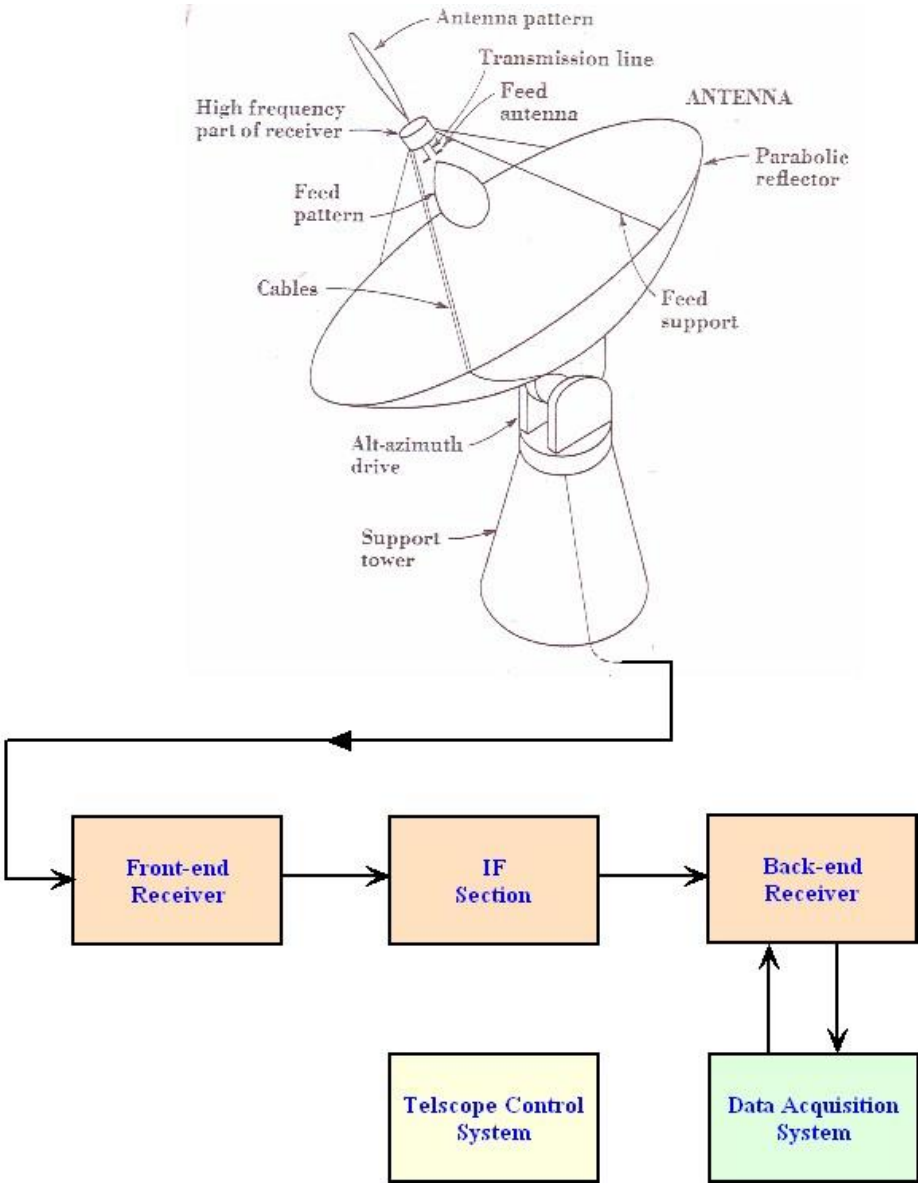

Figure 1-1: Block diagram of a single-dish radio telescope.

focus. At the prime focus, a "feed" converts these radio waves to electrical signals. The radio frequency (RF) signal collected by a radio telescope is first amplified using a low-noise amplifier in the front-end receiver, then down-converted to an intermediate frequency (IF) using a superheterodyne receiver and further analyzed using a spectrometer. It is common to call the high-frequency analog receiver as the front-end and the spectrometer as the back-end receiver. Figure 1-1 shows a block diagram of a typical single-dish radio telescope illustrating the various sections of a radio telescope.

Radio astronomers are interested in measuring the intensity of radio emission from the sky (I) as a function of the angular coordinates in the sky (θ,ϕ), frequency of emission (ν), polarization (P), and time (t), i.e., $I(\theta,\phi,\nu,P,t)$. In this thesis, we are concerned with the development of instrumentation for measurement of $I(\nu)$ and $I(\theta,\phi)$ only.

1.2 Nature of Signals in Radio Astronomy

A radio telescope couples the radio emission from the Universe to the astronomer's measuring device. Radio astronomy receivers, in general, look at very weak signals deeply embedded in noise. The signals are noise-like, i.e., the electric fields are Gaussian random variables with spectra dependent on the emission mechanism [2]. That is, if we take a series of independent voltage samples, and plot a histogram of the samples, the result will be:

$$f(x)=\frac{1}{\sigma\sqrt{2\pi}}e^{\frac{-(x-\bar{x})^2}{2\sigma^2}} \tag{1.1}$$

where, σ^2 is the average square of the voltage and $\bar{x}$ is the mean value of the voltage. In most cases the signal power is broad-band noise, the statistical properties of which do not differ from the noise originating in the receiver itself or from the background noise coupled to the receiver by the antenna. The astronomical signals from a source and the noise generated by the tool used to measure them can be described as time-stationary Gaussian noise. So, for a radio astronomer, the main problem is in distinguishing the astronomical signal from the receiver noise, as the detected signal contains both of them. In the measurement of the power spectrum of the received signal from a radio telescope, the signal-to-noise ratio (SNR) is limited by the noise in the measuring system which is compounded from sky background noise and receiver noise. As the received signals are noise-like random processes, time-averaging is required to obtain an estimate of each point in the power spectrum. In spite of the averaging, there is always an uncertainty in the measurement which cannot be less than the system noise, reduced by a factor of $\sqrt{\beta\tau}$, where, β is the bandwidth of the signal being measured and τ is the averaging/integration time to measure the power spectrum [3].

1.3 Digital Correlation Receivers used in Radio Astronomy

1.3.1 Digital Autocorrelation Spectrometer

Astronomical sources like masers have considerable spectral structure (line sources). The spectrum can have enough structure to warrant hundreds to thousands of points of resolution. In order to detect and measure these spectral-line emissions, we need a device to measure the power spectrum – a spectrometer. A spectrometer can be considered to be a device that receives an input signal s(t), which is varying in time, and estimate its power spectral density S(f). The estimate is sampled at N equidistant frequency points, or channels, f_0, f_1, …, f_{N-1}, separated in frequency by B/(N-1), where B is the bandwidth of the signal. In a spectrometer, all points of spectral resolution are measured simultaneously because, the received signals are noise-like random processes and time-averaging is needed at each filter/detector. Sampling theory shows that the time needed to gather the required number of independent samples will be inversely proportional to the bandwidth. Since commercially available spectrum analyzers - a scanning receiver with a single bandpass filter - use frequency sweepers to obtain a broadband spectrum, they are not sensitive enough for radio astronomical applications. So, special instruments have been developed for spectral analysis in radio astronomy.

One of the most commonly used spectrometers in radio astronomy is the digital autocorrelation spectrometer. Its principle of operation in based on the Wiener-Khinchin theorem which states that the power spectrum of a signal is the Fourier transform of its autocorrelation function (ACF) [4]:

$$S(f) = \int_{-\infty}^{+\infty} R_{xx}(\tau) e^{-j2\pi f\tau} d\tau \tag{1.2}$$

where, $S(f)$ is the power-spectral density, $R_{xx}(\tau)$ is the autocorrelation function given by

$$R_{xx}(\tau) = \int_{-\infty}^{\infty} x(t)x(t+\tau)dt \tag{1.3}$$

This indirect method allows accumulating the ACF before Fourier transformation produces the final power spectrum, which eases the speed requirements of the computation-intensive FFT engine. While the autocorrelations are usually measured in hardware, the Fourier transforms are carried out in a general-purpose computer.

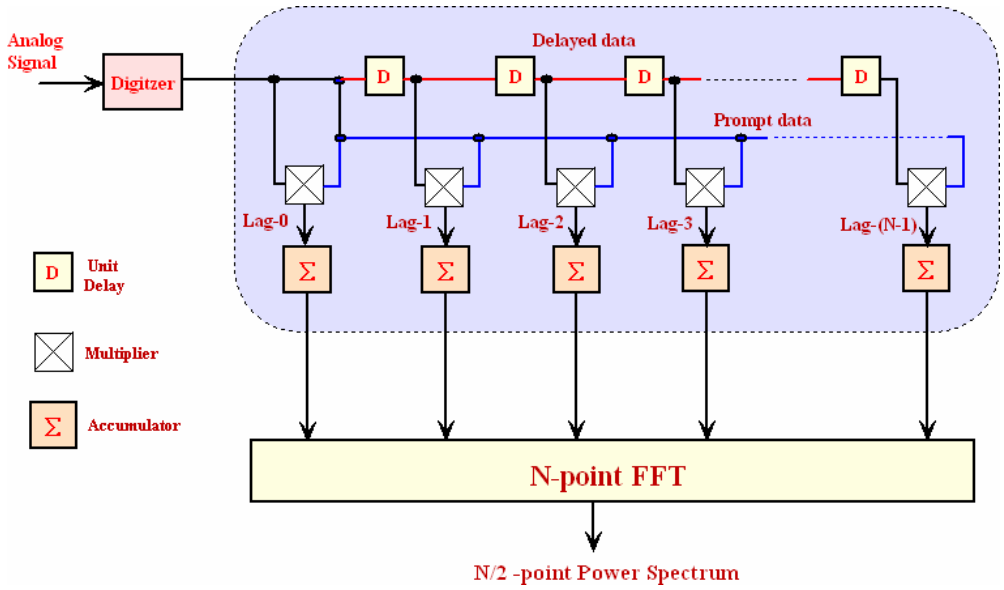

Figure 1-2: Schematic overview of an autocorrelation spectrometer.

Digital correlation receivers optimized for radio astronomy have usually been built around a custom Very Large Scale Integration (VLSI) correlator chip in which designs have favored coarse quantization in order to obtain higher speed and have more correlator channels. Figure 1-2 shows a schematic overview of an autocorrelation spectrometer. Although, coarse quantization of the input signal to a few bits results in a degraded signal-to-noise ratio, it simplifies the multipliers and accumulators that form the correlator.

The architecture in question contains N identical arithmetic modules or "lags" which operate in parallel, independently forming products from two data streams and accumulating the sum of these products. One of the data streams, the "prompt" data is common to every lag. The other data stream, the "delayed" data, is supplied from successive taps of a shift register contained on the chip [5]. Each clock pulse advances the shift register data and adds the new lagged products to the contents of each accumulator. Each module thus calculates a point on the autocorrelation function, i.e. the average product of the signal voltage at time T and the signal voltage at time (t-T). The autocorrelation function can be readily calculated in hardware once the incoming signal has been digitized. The advantage of digital correlation lies in the intrinsic digital nature of measurement: less expensive components, more stability, greater reliability and, more flexibility. The autocorrelator has two other major advantages.

The first advantage comes from the simplicity in the architecture of the autocorrelator module. The modules run independently. Apart from the shift register that distributes the delayed data, there are no data interconnections between modules. The correlator is easily expandable. To get more points on the spectrum, i.e., increase the spectral resolution, one cascades more of the same modules. Conversely, a machine with many modules can be subdivided into several smaller correlators which can independently analyze several different signals. At the system level, the simplicity of the basic module thus provides flexibility in terms of trading off bandwidth processed for spectral resolution.

The second advantage is that correlators can use very coarse quantization of the input signal. The radio astronomical signals are noise-like and follow Gaussian amplitude probability distribution. So, in a correlation spectrometer for noise-limited applications, very coarse quantization of the signal can be used with little loss in signal-to-noise ratio-the variance in an N_s sample estimate of the correlation function is increased over what it would have been for multi-bit correlation. Instead of digitizing the signal with 8 to 16 bits, as is often required in digital signal processing, it is common to digitize to only one bit; the amplitude is ignored and the signal's polarity determines whether the value of the bit is a 1 or a -1. As expected, such a distorted representation of the signal produces a distorted version of the desired correlation function, but, as long as the signal is a Gaussian random process, the distortion can be removed perfectly after the integration by a procedure called quantization correction. This relationship between the correlation function of the input signal and the correlation of the 1-bit representation was first described by J.H. Van Vleck [6] and is given by:

$$\rho_x = \sin(\frac{\pi}{2}\rho_y) \tag{1.4}$$

where, ρ_x is the true correlation obtained from the measured correlation ρ_y. The 1-bit arithmetic greatly simplifies the multipliers and accumulators that form the correlator modules [7]. Each multiplier reduces to a single exclusive-or gate and each accumulator reduces to a counter. Simple one-bit correlation, however, does have its price: more integration time, by a factor of 2.47, is required if the averaging is to be as effective as if the

Number of bits	Number of levels	Optimal threshold spacing	Efficiency at Nyquist rate
1	Two	-	64%
2	Three	1.224σ	81%
2	Four	1σ	88%
3	Eight	0.65σ	96.2%
4	Sixteen	0.374σ	98.7%

Table 1-1: Optimum threshold levels and efficiency for some quantization schemes.

signal had been multi-bit. Going from a 1-bit digitizer to a 2-bit, four-level digitizer reduces the 2.47 integration time penalty to only 1.29 but obviously complicates the multiplier and the accumulator circuitry. A 2-bit, three-level digitizer (usually output codes 00, 01 and 10 are considered while 11 is ignored) is often used; it permits multiplier/accumulator circuitry almost as simple as the 1-bit case and yields an integration time penalty of 1.51.

In all of these quantization schemes the distortion of the ACF can be corrected. Some of the integration time penalty can be recovered. When the signal is over-sampled by a factor of 2, i.e. sampling at a rate of 4 times the bandwidth, the factors of 2.47, 1.29, and 1.51 reduce to 1.82, 1.14, and 1.26, respectively. Table1-1 shows the optimum threshold levels, quantization efficiency for some of the commonly used coarse quantization schemes. The efficiency factor is defined as the ratio of signal-to-noise ratio of the digital correlator relative to the signal-to-noise ratio of an analog correlator.

1.3.2 High-speed Analog-to-Digital Converters in Receivers

A significant advance in receiver design since the advent of superheterodyne principle is the development of the software radio concept in which the ADC is positioned as close to the antenna as possible, so that the resulting samples can be processed digitally [8]. As advances in technology provide increasingly faster and less expensive digital hardware, more of the traditionally analog functions of a radio receiver are being replaced with software or digital hardware. The final goal for radio receiver design is to directly digitize the RF signal at the output of the receive antenna and therefore implement all receiver functions in either digital hardware or software. An analog receiver's RF front end uses local oscillators and mixers to down-convert the signal to an intermediate frequency (IF), typically in a few

hundred MHz range, before digitization by an ADC. The direct RF sampling front end eliminates the mixing stages.

The development of direct RF/IF sampling receiver has been spurred by recent advances in commercial ADCs that can operate continuously on input signals with bandwidths in excess of a Gigahertz. There is a keen interest in replacing analog hardware with digital signal processing in radio receivers for the following reasons: 1) In the direct RF sampling receiver, by eliminating the analog components for frequency translation, the potential sources of error introduced by the non-linearity of the mixing, can be avoided; 2) The processing of digital samples by a programmable microprocessor offers flexibility in evaluating a receiver architecture or the incorporation of the latest signal processing algorithms without the need to build costly prototypes; 3) As the ADC operates at high conversion rates, thus capturing a broad frequency spectrum, a single front end can be used to process a wide range of RF signals. Thus, a single receiver has the potential to replace multiple receivers. However, a key advantage of the IF sampling receiver design is its ability to provide better linearity in the presence of large adjacent out-of-band signals. With direct RF sampling no such stages exist and the converter must support the full dynamic range.

The two important concerns that need to be addressed when sampling at RF/IF are aperture width and aperture jitter. The aperture width is the effective time duration over which the carrier signal gets averaged to produce a given ADC output. The width of this window is inversely proportional to the maximum input bandwidth that the ADC can accommodate. So, if a higher frequency carrier is input, then the ADC's averaging process will significantly degrade the strength of the sampled signal. Aperture jitter or aperture uncertainty is the sample-to-sample variation in the encode process of an ADC which can be caused externally by jitter in the sampling clock, and internally by the sampling switch which does not open at precise times. Aperture jitter causes the ADC to sample at a different phase of the carrier wave than assumed which can lead to signal power loss and carrier phase measurement errors.

1.3.3 Fast Fourier Transform Spectrometer

Autocorrelation is not the only way to do digital spectrometry; the Fast Fourier Transform (FFT) is, in principle, more efficient for large enough N where, N is the number of FFT points. Traditionally, digital signal processing required a dedicated digital signal processor (DSP) which is a microprocessor designed to handle digital signal processing tasks. In some high-performance signal processing applications, field-programmable gate arrays (FPGAs) can take advantage of their highly parallel architectures (hardware parallelism) and offer much higher throughput than DSPs by breaking the paradigm of sequential execution and accomplishing more per clock cycle. FPGAs provide a competitive alternative for high-performance DSP applications previously dominated by general-purpose DSPs and Application Specific Integrated Circuits (ASICs). Of late, with the integration of specialized functions and expansion of performance and capabilities in terms of speed and density of gates, FPGAs have begun to take on ASICs role in system design. The FPGAs maintain the advantage of custom-based functionality like that of an ASIC while at the same time avoids high development costs. Specialty components, such as dedicated multiply and accumulate units (MACs), greatly improve FPGA utilization and efficiency for DSP applications. Without these specialized components, the seemingly simple task of multiplying two numbers together can become extremely resource-intensive. The state-of-the-art FPGAs have a few hundred of 25 x 18 bit MACs in specialized blocks called the DSP48 slice, which are specifically designed for DSP data and signal analysis operations. The rapid increase in the capabilities of FPGAs coupled with advances in the high-speed analog-to-digital converter has led to the development of Fast Fourier Transform Spectrometer (FFTS).

Fourier spectroscopy involves three operations: (i) sampling the analog signal with a high bit-resolution, (ii) computing the squared magnitude of the Fourier transform of each windowed data section, and (iii) averaging the spectra.

1.3.4 Correlators for Interferometric Applications

The angular resolution of a radio telescope is given by $\theta \approx 1.22\lambda/D$ where θ is the smallest angular separation that two point sources can have in order to be recognized as separate objects and is measured in radians, λ is the wavelength of the radiation received,

and D is the diameter of the radio telescope. So, even a 100 m radio telescope operating at 300 MHz has a resolution of ~ 42 arc min, which is much poorer than the resolution of our eye (1 arc min) at optical wavelengths. It is not economically feasible to build a steerable, filled aperture telescope of a diameter greater than a few tens of meters. So, the angular resolution of single-aperture radio telescopes is often inadequate for astronomical observation. To obtain angular resolutions comparable to that of optical astronomy (1 arc sec) and allow identification with objects detected in the optical and other parts of the electromagnetic spectrum, a technique known as aperture synthesis is used. Aperture synthesis is based on the well-known Michelson Interferometer. A radio interferometer consists of a pair of directional antennas that are tuned to receive radio emissions from a source in a desired RF band. The signals from the two receivers are then cross-correlated to measure the coherence function.

Generally, a radio astronomer measures the intensity distribution as a function of angular coordinates $I(\theta,\phi)$ by using an array of antennas and a correlation receiver which measures $\frac{n(n-1)}{2}$ correlations, where, n is the number of antennas. The fundamental idea behind this is the Fourier transform relationship that exists between the sky radio brightness distribution $I(\theta,\phi)$ and the spatial coherence function $V(u,v)$. This is known as the van Cittert-Zernike theorem:

$$V(u,v)=\int_{-\infty}^{\infty}\int_{-\infty}^{\infty} I(\theta,\phi)e^{j2\pi(u\theta+v\phi)}d\theta d\phi \tag{1.5}$$

where, (θ,ϕ) are the direction cosines, and (u,v) are the E-W and N-S components of the projected baselines, measured in wavelengths.

A correlation interferometer basically measures one Fourier component of the sky brightness distribution over that part of the sky which is within the primary beam of each antenna element [9]. Thus, by measuring the Fourier components over a wide range of antenna spacings, the sky brightness distribution may be reconstructed with much higher resolution than is possible with a large filled aperture telescope. This method of gradually building up all the required Fourier components and using them to image the source is called synthesis imaging. The Fourier components may be measured simultaneously or sequentially. The use of the rotation of the earth to provide a continuous arc of baselines is called Earth-

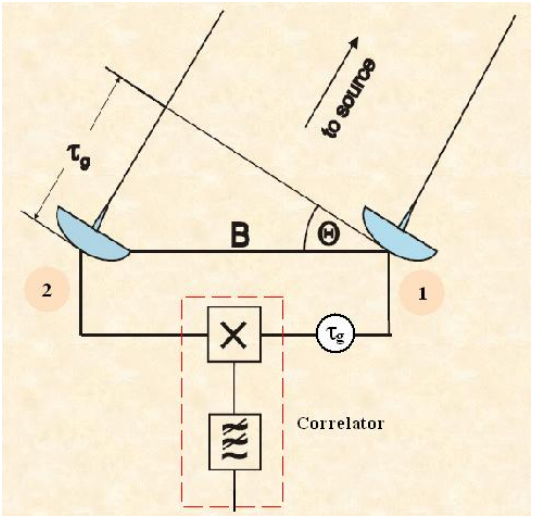

Figure 1-3: Schematic diagram of a two-element interferometer.

rotation synthesis. If the array of antennas is compact (within a few tens of kilometers), phase-synchronized local oscillators can be distributed to the antennas and the signals from the antennas can be directly connected to the correlation receiver. If the antennas are widely separated, connecting them in real-time to a correlation receiver may be difficult. The technique of Very Long Baseline Interferometry (VLBI) was developed to overcome this problem. In VLBI, highly stable reference clocks are used for synchronization and the signals from the antennas are recorded on hard disks and correlated offline [10].

A two-element radio interferometer consists of a pair of directional antennas that are tuned to receive radio emission from a source in a desired RF band. The signals from the two receivers are then cross-correlated to measure the coherence function. Figure 1-3 shows a schematic diagram of a two-element interferometer. The signal arrives at the second antenna delayed by the geometrical time delay τ_g with respect to the first antenna. This geometrical delay (path delay) is compensated before cross-correlating the signals from the two antennas. The Fourier transform of the coherence function gives the source visibility as a function of frequency for a particular orientation of the baseline between the telescopes. Observations with different baselines yield the visibility function, and this can be transformed to obtain the source brightness distribution.

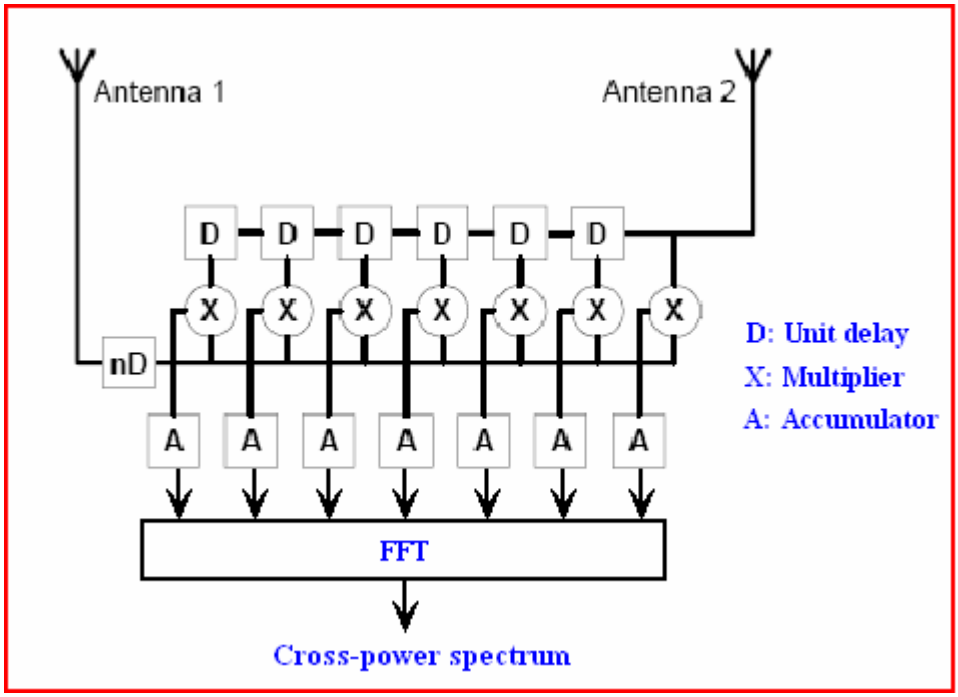

Figure 1-4: Schematic diagram of an XF correlator.

Cross-correlators are used in interferometric arrays to determine the cross-power spectrum (visibility) between telescope pairs. The two fundamental operations required to combine or correlate the signals are a Fourier transform (F) and a cross multiplication (X). The order of these operations can be interchanged to obtain the cross-power spectrum, leading to the so-called XF and FX correlator architectures which are described below. In the first method, the cross-correlation function, $R_{xy}(\tau)$, given by:

$$R_{xy}(\tau) = \frac{1}{N}\sum_{k=0}^{N-1} x(k)y(k+\tau) \tag{1.6}$$

is measured for each pair of antennas as a function of delay 'τ', and then Fourier transformed to obtain the cross-power spectrum (spectral visibility).

The digital implementation of this method is called an XF correlator (lag-domain correlator) where, 'X' stands for correlation and 'F' stands for Fourier transformation. A schematic diagram of the XF correlator is as shown in Figure1-4 [11].

In the second method, instead of measuring the cross-correlation function, the cross-power spectrum is directly measured. In such a correlator, the input bit stream from each antenna is converted to frequency-domain by a real-time FFT, and then for each antenna pair,

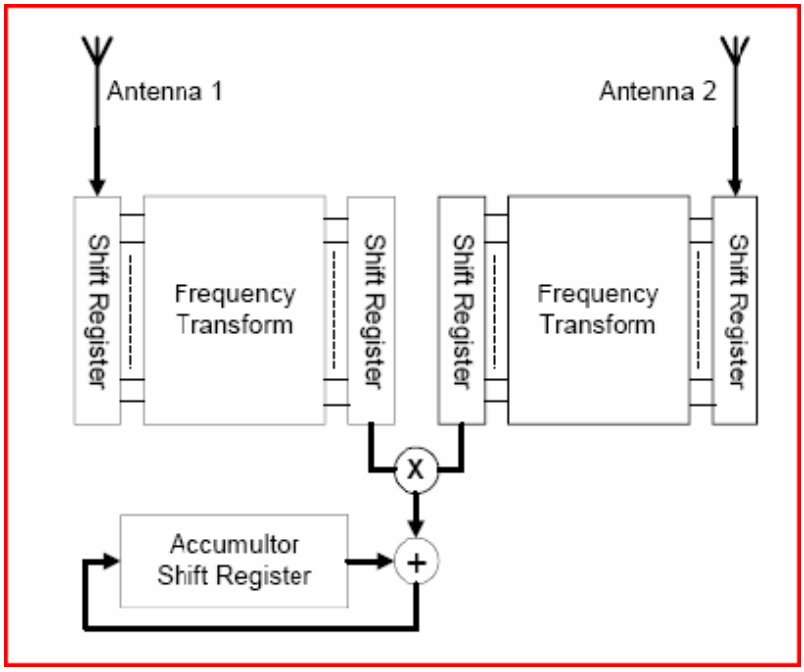

Figure 1-5: Schematic diagram of an FX correlator.

the complex amplitudes for each frequency bin are pair-wise multiplied to produce the cross-power spectrum. This type of correlator is called an FX correlator because the frequency transformation preceded cross multiplication. Figure1-5 shows a schematic diagram of the FX correlator [11].

Correlators for radio astronomy have usually been built around special purpose ASICs that derived their performance from highly optimized circuits. Contrary to the increasing costs and risks of designing ASICs, FPGAs, with their growing densities and on-board system functionality, are rapidly proving to be a cost-effective, flexible and lower risk alternative. FPGAs have evolved into an enabling technology that allows system designers to minimize the time and risk involved in developing a new product. In the last few years, FPGAs have become popular in correlator designs as FPGAs are reconfigurable or reprogrammable devices that offer more flexibility than ASICs while still being highly efficient.

For a typical multi-element radio telescope, involving a large number of antennas/elements, computational load in terms of operations per second is orders of

magnitude less for an FX correlator compared to that of an XF correlator. However, FX correlators suffer from higher interconnection costs and bit-rate increase.

1.3.5 Software FX correlator

In VLBI, as with all interferometry at radio wavelengths, hinges on the ability to obtain a digital representation of the electric field variations at a number of spatially separated locations (radio telescopes), accurately time-tagged and tied to a frequency standard. The digitized data are transported to a single location for processing (a correlator) and are coherently combined in order to derive information about the high angular resolution structure of the target sources of radio emission. After observations, the data collected from each telescope are brought to a purpose-built and dedicated digital signal processor, the correlator. The correlator aligns the recorded data streams, corrects for various geometrical and instrumental effects, and coherently combines the data from the different independent pairs of radio telescopes. An alternative to customized hardware correlator is to develop software which carries out the correlation operations on non-application specific hardware like, general purpose computers. A generic modern CPU is capable of calculating a large N-point FFT, allowing correlator implementation consisting of re-usable code which can run on more than one computational platform is referred to as a 'software correlator'. In recent years, with the increase in the capability and easy availability of commodity computing equipment like: processors, storage, networking, etc. has made the correlation of interferometric data feasible. The correlation algorithm is highly parallel and very well suited for parallel computing architectures. The highly parallel nature of the correlation problem coupled with the availability of high-level programming languages and optimized vector libraries, means that a reasonably general software correlator code can be written quickly and be used in a variety of different computing environments with minimum modification. However, the trade-off for flexibility and the convenience of high-level programming tools is a reduced efficiency for any given task compared to an application-specific or FPGA-based solution. Some of the advantages of software correlator [12] over hardware correlator are:

1. Flexibility: The data structures are allocated dynamically rather than being constrained by fixed hardware boards. The spectral resolution, time resolution, number of inputs considered can be changed with ease.

2. Compared to designing with an application-specific hardware or even FPGA-based processors (although the programming tools for FPGAs are developing rapidly), with the use of high-level programming languages, it is easier to develop the software correlator.
3. Modular design helps in expanding the network of computers to cater to more antennas or provides capability to handle higher bandwidth (scalability). As and when more powerful computational platforms are available and affordable, the existing system can be upgraded. The changes in the software (fixes) do not need rewiring.
4. Extra precision means more wiring and additional complexities in the design of the design of the correlator hardware; whereas, in a software correlator, the general-purpose computers provide us with floating-point accuracies.

1.4. Objectives and Scope of Study

The two primary objectives of this thesis are:

1. The Raman Research Institute (RRI) operates a 10.4 m radio telescope. This telescope was till recently operating at 6.667 GHz for studying Methanol maser lines emanating from celestial sources in our Galaxy. The front-end is now being upgraded to operate at around 50 GHz. One of the primary objectives of this thesis was to design and develop a spectrometer capable of processing a bandwidth of about 320 MHz (single polarization) or 160 MHz (dual polarization) for carrying out spectral-line survey using the RRI 10.4m radio telescope. A wideband spectrometer (WBS) based on a 2-bit, 3-level Application Specific Integrated Circuit (ASIC) from the National Aeronautics and Space Administration (NASA)-USA had to be designed for the following specifications: capability to process a bandwidth of 160 MHz (dual-polarization), 4096 correlation lags per polarization, provision to trade off bandwidth for improved spectral resolution catering to both broadband and narrowband observations, capability to work as a total power receiver in which an estimate of the total power in the band of interest is obtained from the zeroth lag of the autocorrelator. Then, the WBS had to be integrated with the 10.4 m radio telescope and test observations carried out at 6.667 GHz on an astronomical source (Methanol maser) to validate the instrument. Later, the autocorrelator unit of the WBS had to be integrated with an analog-to-digital converter (ADC) capable of directly digitizing astronomical signals in the L-band thereby, minimizing the number of IF units

in the spectrometer. Then, test observations on an astronomical source had to be carried out to realize the concept of a spectrometer based on direct digitization of signals up to 1.4 GHz.

2. The Giant Metrewave Radio Telescope (GMRT), which is a rotational synthesis instrument, is an array of 30 dish antennas with each antenna having a diameter of 45 m. Fourteen of the thirty dishes are located in a compact central array, a region of about 1 sq km. The remaining sixteen dishes are spread out along the 3 arms of an approximately `Y'-shaped configuration over a much larger region, with the longest interferometric baseline of about 25 km. The array operates in five frequency bands centered around 150, 230, 325, 610 and 1420 MHz. RRI had designed and developed a low-frequency V-dipole feed with a plan to equip GMRT with a low frequency receiver system, operating in the frequency range 40-80 MHz. In receiver systems, the signal-to-noise ratio increases with increase in bandwidth (β) and integration time (τ). Astronomical observations carried out at GMRT showed that $\sqrt{\beta\tau}$ improvement was not forthcoming when observed using the existing GMRT receiver chain which could possibly be due to systematics, RFI, cross-talk in the analog signal conditioners and correlators. It may be noted that analog signals from each antenna are carried on optic fiber to a centralized location for further processing. To study if this limitation can be overcome by digitizing the output of the low frequency front-end receiver right at the antenna base and transmit the digitized signals on optical fiber to a centralized place for further processing, we developed a system equivalent of a two-station VLBI by employing digital recording systems. Two digital recording systems, which could in principle be separated by several kilometers, were developed for the following specifications:

   a. Capability to digitize a signal of bandwidth ~5 MHz (anywhere within 40-80 MHz band) using a sampling clock of about 11 MHz.
   b. Synchronously release the recording systems at the two antenna bases using high-stability Rubidium oscillators referenced to a signal from Global Positioning Systems (GPS) receiver.
   c. A data acquisition system capable of recording 8-bit data at about 25 Megabytes per second, to record two orthogonal polarizations at each antenna base.

d. After recording the voltages from a radio source at the two antenna bases, cross-correlation of the data needed to be carried out in software with features to detect and replace data points affected by radio frequency interference, implement frequency-domain channelization, and compute cross-correlations on the two data sets to generate the visibilities as a function of time for the single baseline. From the test observations carried out on an astronomical source, the signal-to-noise ratio (SNR) performance as a function of both β and τ obtained from the direct recording system had to be estimated and compared with those obtained from the existing GMRT back-end receivers. Further, investigations had to be carried out to identify if any of the sources mentioned above was behind the $\sqrt{\beta\tau}$ improvement not forthcoming with the regular GMRT receivers.

1.5 Thesis Outlay

This thesis is organized into five chapters. Chapter 2 contains two sections: Section-A describes a hybrid wideband autocorrelation spectrometer (WBS) for spectral-line observations which has been built around a 1024-lag VLSI for 2-bit, 3-level operation. The results obtained from Methanol maser observations carried out using the wideband spectrometer in narrowband and broadband mode are discussed. Section-B describes a spectrometer based on direct digitization of signals in the L-band (1 to 2 GHz). Section-B also describes the considerations that go into choosing a high-speed ADC for modern digital receivers. Chapter 3 describes the design and development of a direct voltage recording system to digitize and record voltages right at the antenna base (using two GMRT antennas). The chapter 4 of the thesis describes the integration of the direct voltage recording systems with the GMRT receiver system and the results obtained from test observations carried out at 50 MHz. In the last chapter, chapter 5, a summary of the work carried out as part of this thesis is presented. Towards the end of this thesis, there are two appendices:

1. Appendix A contains the schematic diagrams of major modules/units developed as part of work related to the hybrid wideband spectrometer and the direct voltage recording system for 50 MHz observations at GMRT. Appendix A also contains data sheets of major electronic components used in these modules/units.

2. Appendix B is a compact disc (CD) containing important programs that were developed as part of this thesis, along with a read-me file explaining the salient features of each program, and the procedure to compile and execute each program.

Chapter 2

Chapter 2

Section-A

Development of a Hybrid Wideband Spectrometer

2.1 Introduction to a Hybrid Spectrometer

Digital autocorrelation receivers optimized for radio astronomy have usually been built around custom Very Large Scale Integration (VLSI) correlator chips. The highest clock speed at which these VLSI correlator chips operate is limited by technology. In order to develop autocorrelation spectrometers capable of processing higher analog bandwidths, several such VLSI correlator chips are operated in parallel. It is obvious that pre-filtering a wideband signal by N filters reduces the digital operations per second by a factor of N to bring it within the realm of VLSI correlator chips. This approach of merging a filter bank and an autocorrelator results in what is termed as "hybrid spectrometer" [13]. In a hybrid spectrometer, the signal frequency band is split into frequency sub-bands by a number of bandpass filters. The output from each filter is then digitized and analyzed by an autocorrelator. The possibility of assigning different number of correlator channels to different filters is the greatest advantage of this configuration. A block diagram of a typical hybrid spectrometer is shown in Figure 2-1.

2.2 Need for a Hybrid Wideband Spectrometer

The technical challenge in obtaining the spectra from a variety of spectral-line sources, each emitting/absorbing from a range of physical conditions, is essentially one of providing a versatile spectrometer capable of processing a wide bandwidth with varying spectral resolution. A radio astronomer will typically choose the frequency resolution an order of magnitude greater than the width of the spectral-line to enable measurement of line profile. In order to carry out a survey of the Maser sources at around 6.667 GHz, and targeted observation of other spectral-lines sources, a hybrid wideband spectrometer (WBS) capable of processing a bandwidth of 320 MHz was developed to form the back-end receiver of the 10.4m radio telescope which is operated by the Raman Research Institute. The WBS was required to have a flexible architecture with trade-off between bandwidth processed and spectral channels.

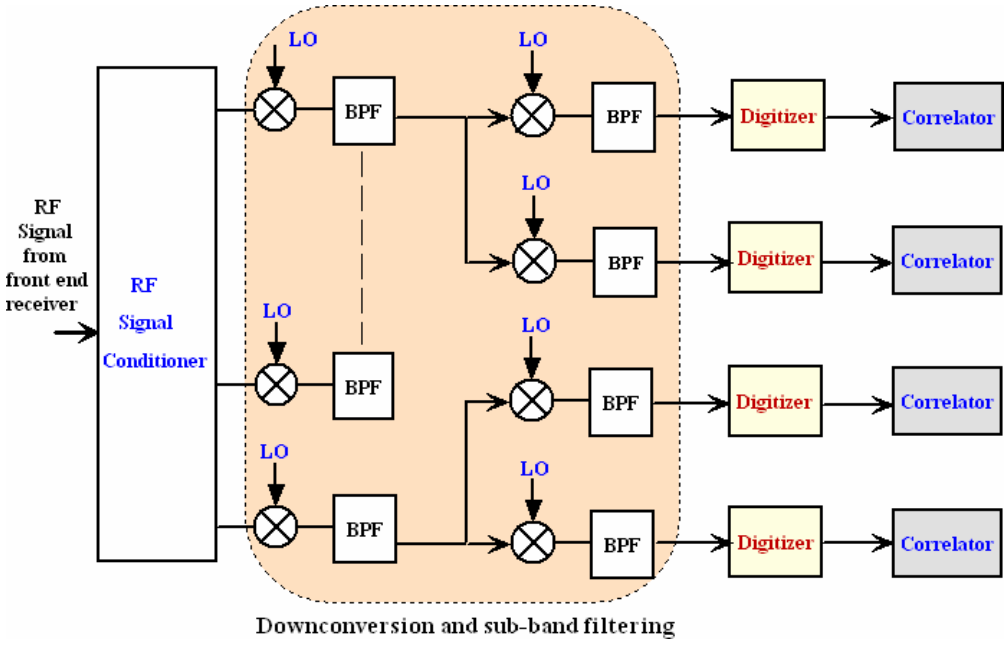

Figure 2-1: Block diagram of a typical hybrid spectrometer.

2.3 Description of WBS

A hybrid wideband spectrometer (WBS), capable of processing a bandwidth of 160MHz, dual polarization, or 320 MHz (single polarization) has been designed and developed. The block diagram of the wideband spectrometer is as shown in Figure 2-2. The IF unit of the spectrometer accepts an RF signal ranging from 1040MHz to 1720MHz and produces four signal bands centered around 80 MHz, each of bandwidth equal to 40 MHz. This is accomplished in two stages of downconversion: the first-stage IF unit selects a signal of bandwidth equal to 160 MHz from the RF input signal and down converts it to an IF signal centered around 320 MHz, using a programmable local oscillator; the second- stage IF unit, containing four staggered local oscillators, produces four bands of bandwidth equal to 40 MHz, centered around 80 MHz, thus covering the entire 160 MHz band (per polarization). For the downconversion stages, programmable local oscillators modules in the frequency ranges: 1290 to 2000 MHz, 300 to 500 MHz and 170 to 230 MHz are available. These modules are from Synergy Microwave limited and are programmed through the PC parallel

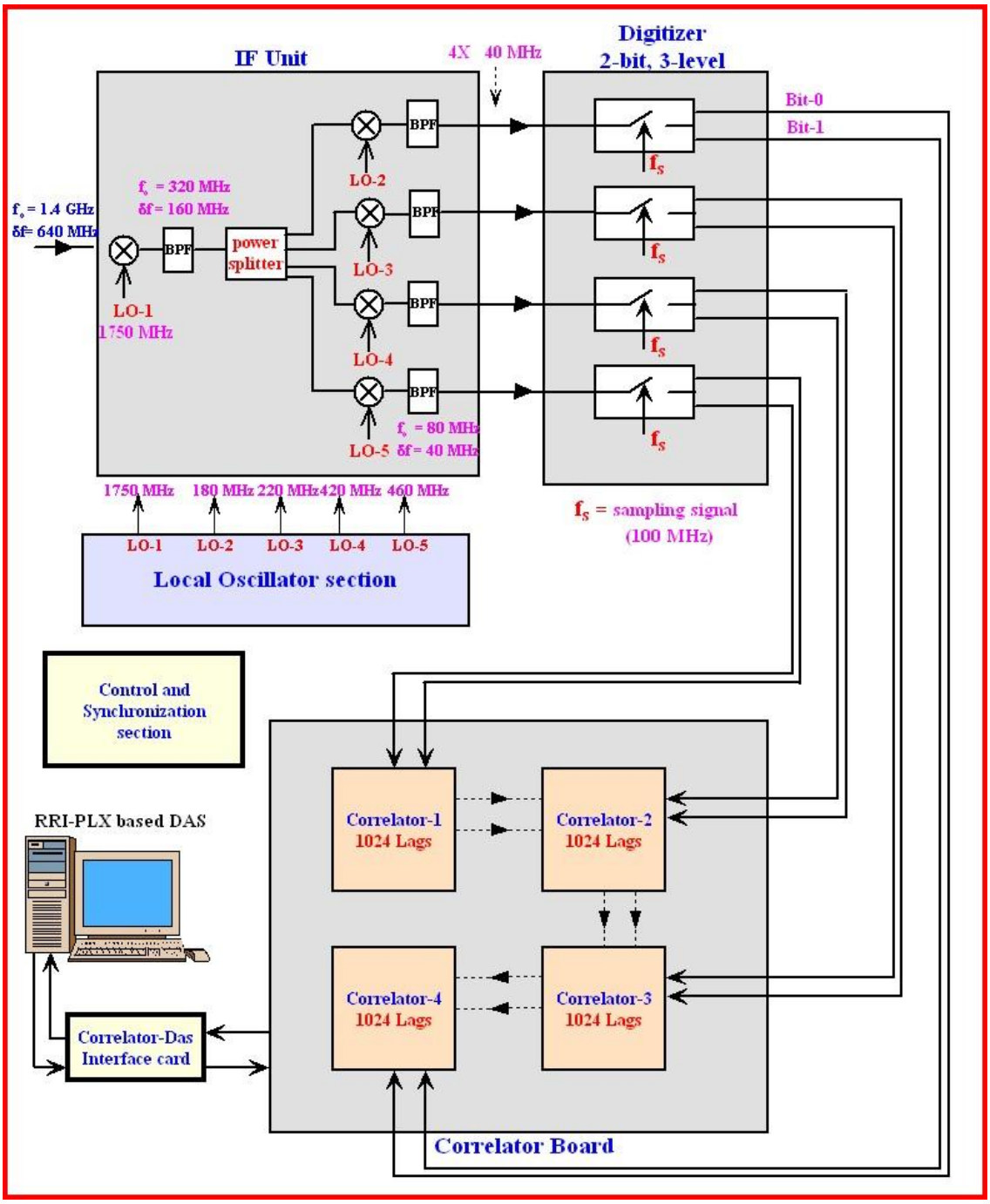

Figure 2-2: Block diagram of the hybrid wideband spectrometer.

port. The 40 MHz output bands of the IF unit are coupled to the digitizer section, which produces a 2-bit, 3-level representation of the input analog signal at the rate of 100 Mega samples per second. The coarse quantized outputs from the digitizer unit are then interfaced to the correlator unit. The correlator unit is built around four, 2-bit, 3-level NASA correlator chips that can be cascaded, with each chip providing 1024 lags/channels. It can provide a

maximum of 1024*4=4096 autocorrelation lags across a single IF band, or, 1024 lags across each of the four IF bands. An identical setup exists for the other polarization. So, the raw spectral resolution can vary from about 12 kHz to 49 kHz. The correlator can be configured to operate in two different modes in which the bandwidth processed per polarization can be traded off for higher spectral resolution.

2.4 Digitizer unit for WBS

As described earlier, the IF unit selects a signal of bandwidth equal to 160MHz, and produces four bands of bandwidth equal to 40 MHz, centered at 80MHz. These four bands are fed to the digitizer section, which consists of four, 2-bit, 3-level digitizer modules. The 3-level quantization scheme is considered to be a reasonable compromise between degradation of the signal-to-noise ratio and circuit complexity [5]. The digitizer unit of the wideband spectrometer is a 2-bit, 3-level digitizer circuit built around AD96687BP, which is a dual, high-speed comparator from Analog Devices. Consequently, high speed design techniques have been employed to achieve the best performance. Some of the important design considerations are: the use of a low impedance ground plane, effective power supply decoupling, proper ECL terminations (open-emitter outputs of the AD96687 are terminated through 330 Ω resistors to –5.2V), and microstrip routing for a controlled impedance of 50 Ohms. The comparator provides a latch input, which, in response to a logic signal, freezes the output at a known state at any given instant of time. The comparator has a propagation delay of 2.5 ns, and a propagation delay dispersion of 50 pico seconds, both of which are important characteristics of a high-speed comparator. Propagation delay is the time required for the output to reach the 50% point of transition, after the input has crossed the threshold voltage. It denotes the highest frequency of the input signal that can be compared using the comparator. Propagation delay dispersion is a measure of the difference in propagation delay under differing overdrive conditions. The AD96687's propagation delay of 2.5 ns allows us to comfortably use the device as a comparator because the highest frequency component in the input to the digitizer is only 100 MHz.

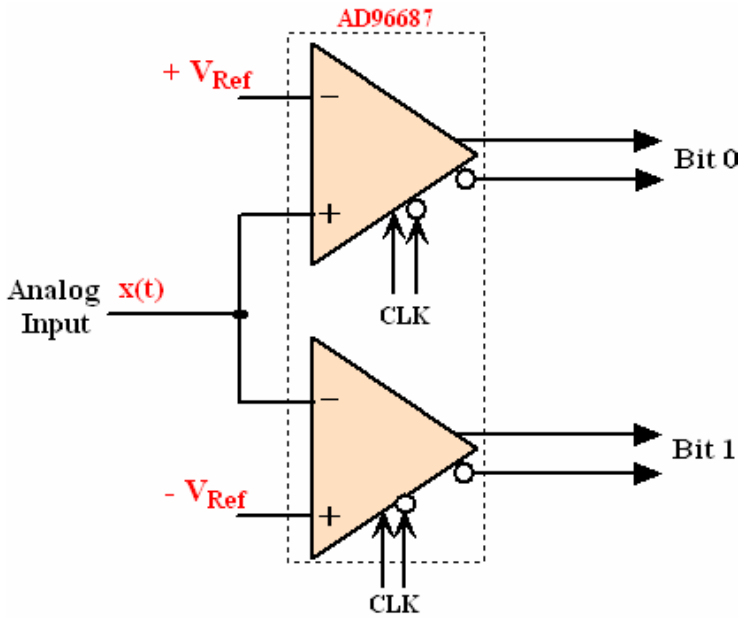

Figure 2-3: Schematic overview of the 2-bit, 3-level digitizer circuit used in hybrid wideband spectrometer.

The digitizer board of the WBS has been designed as a 4-layer board in which one layer is exclusively meant for ground reference. The ground plane provides a low inductance ground, eliminating any potential differences at different ground points throughout the circuit board caused by ground bounce. A proper ground plane also minimizes the effects of stray capacitance on the circuit board. In high-speed applications, power supply decoupling capacitors placed close to the power supply pins of a device act as a charge reservoir for the device during high frequency switching. A decoupling capacitor of larger value (say 10 μF) helps in reducing potential ripples in the bias to the comparator.

Figure 2-3 shows the schematic overview of the 2-bit digitizer used in the WBS. The inputs to the digitizer circuit consist of the analog input signal and the two voltage references. The positive reference voltage was derived from a potential divider network and the negative reference voltage was obtained from a high-precision operational amplifier OPA627. The 2-bit, 3-level, digitizer outputs are driven differentially for further processing by the correlator unit. When the instantaneous amplitude of the input voltage x(t) is greater than $+V_{Ref}$, then the value of Bit-0 and Bit-1 are logic-1 and logic-0, respectively. When the instantaneous amplitude of x(t) is between the two thresholds, then both bits are at logic-0, and in the event that the instantaneous amplitude is lower than $-V_{Ref}$, then, the value of Bit-0 and Bit-1 are

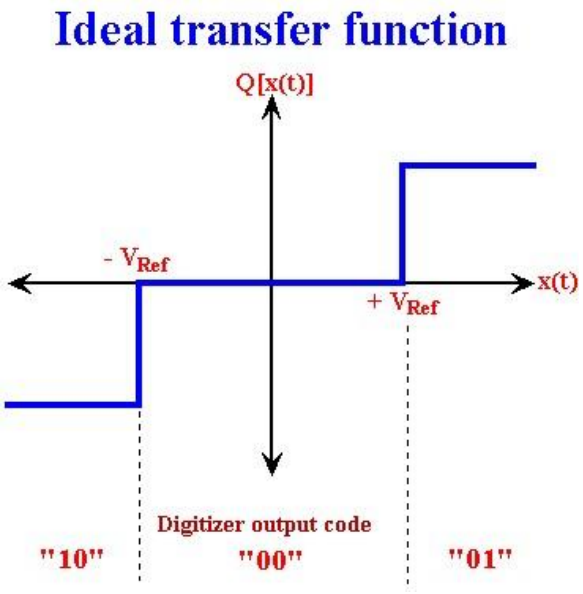

Figure 2-4: Transfer function of an ideal 2-bit, 3-level digitizer.

logic-0 and logic-1, respectively. Figure 2-4 shows the transfer function of an ideal 2-bit, 3-level digitizer circuit [14]. The abscissa is the unquantized voltage x(t) and the ordinate is the quantized output Q[x(t)]. From Table 1-1, the optimum spacing (for achieving the maximum efficiency) between the two reference-voltages for a 2-bit, 3-level digitizer is 1.224σ, which corresponds to individual threshold voltages of 0.612σ [15]. If the reference voltages are fixed at ± 200mV, then the optimum total input power level of the analog signal should be maintained at:

$$V_{Ref} = 0.612\sigma$$

$$\therefore \sigma = \frac{0.200}{0.612} = 0.3267$$

$$P_{in} = 10 \log \left(\frac{\sigma^2}{50} \right) \left[\frac{1}{1mW} \right] \text{ dBm}$$

$$P_{in} = +3.29 \text{ dBm}.$$

The final IF filter has a 3-dB bandwidth of 37.8 MHz, and a 20-dB bandwidth of the ≈ 40 MHz. Given that the input signal to the digitizer ranges from 60 MHz to 100 MHz, the required sampling frequency is calculated using equations (2.1) and (2.2), given below:

$$(2 * f_h)/n \leq f_s \leq (2 * f_l)/n-1 \qquad (2.1)$$

where f_h and f_l are the highest and lowest frequency component present in the pass band, f_s is the sampling frequency, n is an integer obtained from[22]

$$2 \le n \le {f_h}/{BW},\ BW = (f_h - f_l),\ \text{and}\ \ (f_h - f_l) \le f_l \qquad (2.2)$$

So, given that $f_l = 60MHz$ and $f_h = 100MHz$, we find that:

$$2 \le n \le {100}/{40}$$

For $n = 2$, the range of valid sampling frequencies (in Megahertz) is:

$${(2*100)}/{2} \le f_s \le {(2*60)}/{1}$$

Although the valid sampling frequencies can range from 100 MHz to120 MHz, a sampling frequency of 100 MHz was chosen for the WBS because the maximum clock frequency of NASA correlator chip is around 100 MHz. The sampling clock was derived from a synthesized signal generator whose reference input was connected to the 10 MHz observatory reference.

2.5 Correlator Unit for the WBS

Considering that we needed to process a bandwidth of about 160 MHz per polarization, a correlator (VLSI) capable of clocking at 320 MHz with a large number of channels/lags was required. The fastest correlator (VLSI) that was available when the WBS was being designed was the 2-bit, 3-level correlator chip from NASA which could be clocked up to a maximum frequency of about 100 MHz, providing 1024 channels per chip [16]. So, the autocorrelator unit of the wideband spectrometer has been built around four, 2-bit, 3-level NASA correlator chips, providing a total of 4096 channels when cascaded. Figure 2-5 shows a schematic diagram of the correlator board that has been designed for the WBS. The correlator board is an 8-layer board in which signal integrity issues concerned with the design of a high-speed digital board have been addressed. They are, controlled 50Ω impedance routing of high-speed signals with proper ECL terminations (330Ω pulled down to -5.2V) to reduce ringing in the signals, necessary spacings along with grounded guard traces have been provided between high-speed signals so that cross-talk is reduced, adequate decoupling capacitors at the power pins of every IC, and proper ground reference planes. The

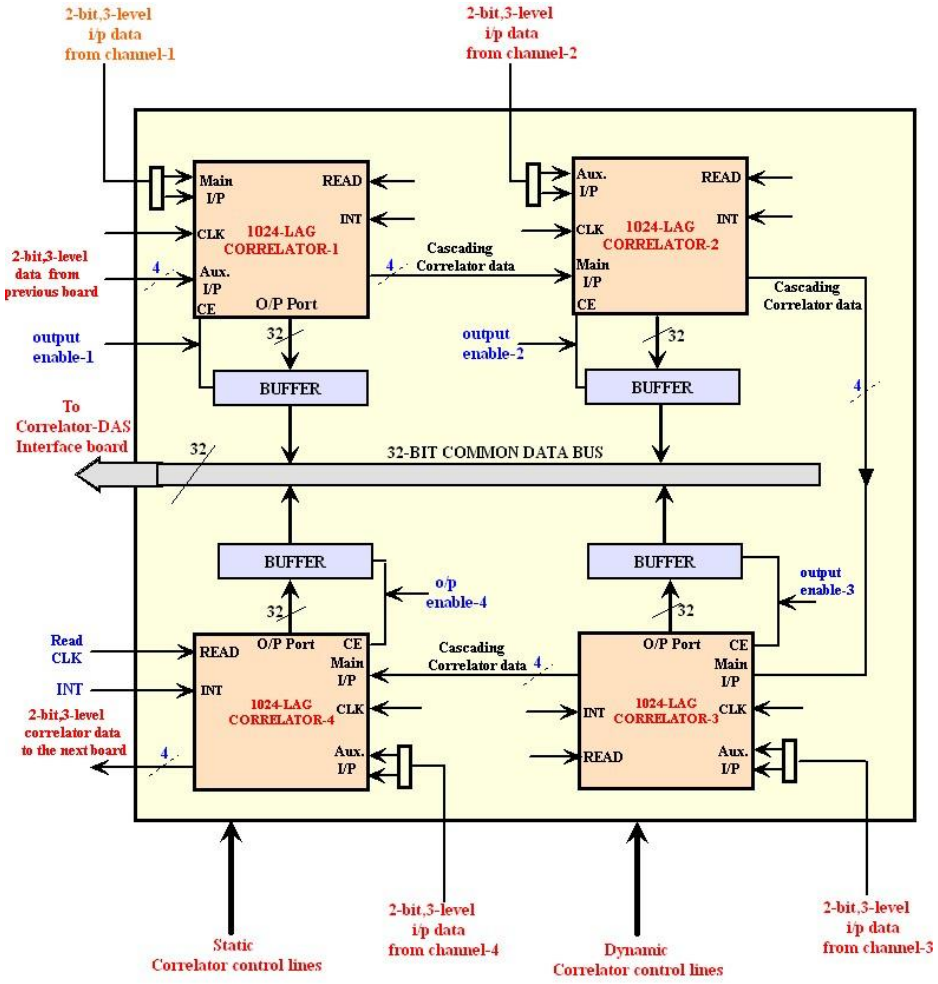

Figure 2-5: Schematic diagram of the correlator board used in WBS.

printed circuit board (PCB) for the correlator unit was designed at RRI using the PCB design tool called Visula.

Each correlator chip has two input ports- a main input port and an auxiliary input port. The ports can accept two data streams-Stream-A (A_0, A_1) and Stream-B (B_0, B_1) -at a rate of about 100 MS/s, either from the previous correlator chip or directly from the digitizer unit [16]. Samples from Stream-A are successively delayed in a 1024-stage internal shift register and multiplied with the prompt data from Stream-B. Both streams use two bits in which only three, out of the four, possible data words are valid. Arithmetic is performed in 1024 multiplier-accumulator unit, operating in parallel. At the end of an integration period, which is controlled by the INT signal, the data in the accumulator is parallel-loaded into 1024 output registers, after which, a new integration can begin. The integration periods can be as

short as 10 clock cycles. However, any integrated data that is not read out before the INT signal goes low again, will be overwritten. The contents of the output registers can be shifted out at rates up to 20 MHz, via a 32-bit tri-stating output port, 30 clock cycles after the integration signal is de-asserted. The data read out is under the control of the chip enable (CE) and the read (READ) signal. When CE is asserted, data will appear on the 32-bit output bus on the rising edge of READ strobe. 1024 successive strobes of READ are required to output data from the chip.

The number of data samples processed by the correlator is provided by an internal counter, which can be accessed in the same manner as the normal lag output register. This counter is attached to the end of the output shift register and can be read as 1025^{th} lag. The value of this register is useful in unbiasing the correlator count of each lag and also in the calculation of correlation coefficient.

Salient features of the correlator chip

The salient features of the NASA correlator chip are:

1. 1024 lags/channel.
2. 32-bit accumulator stages.
3. Data and control signals can be cascaded.
4. Selectable auxiliary ports on both data inputs.
5. Integration can continue while data is read out.
6. ~100 Mega Samples/second.
7. 32-bit tri-state asynchronous output port.

Bit-1	Bit-0	Value
0	0	0
0	1	1
1	0	-1
1	1	Illegal

(a)

Stream-B data \ Stream-A data	+1	0	-1
+1	+1 (2)	0 (1)	-1 (0)
0	0 (1)	0 (1)	0 (1)
-1	-1 (0)	0 (1)	+1 (2)

Multiplication table

(b)

Table 2-1: (a) NASA correlator input data format. (b) Product table of the correlator.

Table 2-1(a) summarizes the correlator input data format. The products of the 2-bit, 3-level data have three possible values: +1, 0 and –1. To simplify the architecture of the multiply-accumulator unit, the products are biased up to 2, 1 and 0, respectively, to allow the accumulation of only positive values. Table 2-1(b) shows the product table of the NASA correlator (products within brackets are the biased values). The multiplier consists of a Modulo-2 counter, with the counter overflow driving the input of a 32-bit asynchronous ripple counter, working as the accumulator. The maximum overflow rate is equal to the clock rate and occurs when the biased product is always 2. Assuming a clock rate of 100 MHz, the on-chip integration period can vary from a maximum of ~43 s to a minimum of 300 ns.

The correlator can be configured to operate in different modes of operation, in which, the bandwidth processed per polarization can be traded off for higher spectral resolution. In Mode-1 of operation, the correlator unit can be configured to process four, independent 40 MHz bandwidth signals, providing a raw spectral resolution of ≈ 49 kHz. In Mode-2, the correlator unit can be configured to put all four correlator chips in cascade, to process a signal of bandwidth equal to 40 MHz, per polarization. In this mode of operation, a raw

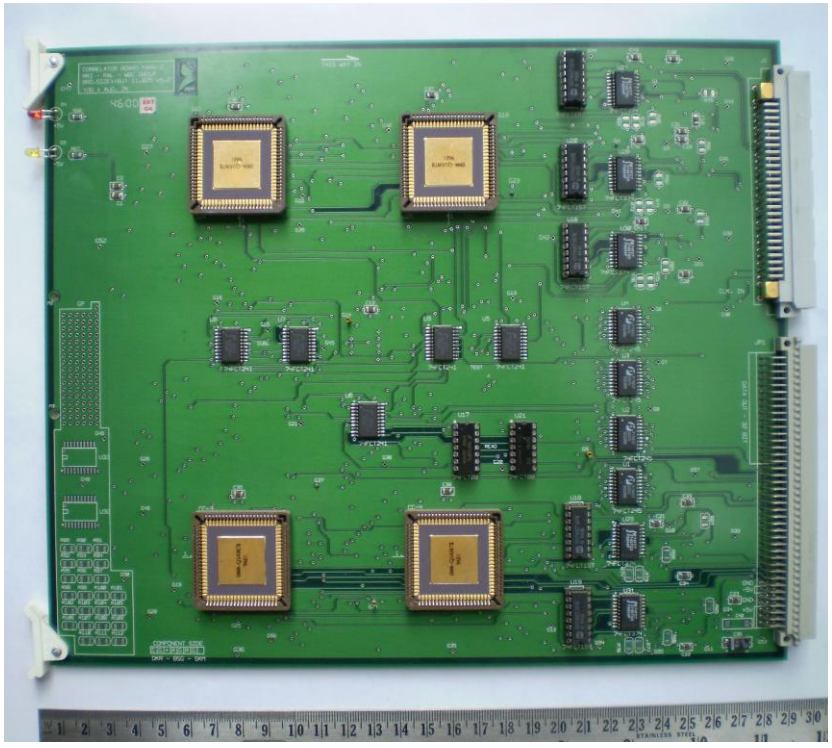

Figure 2-6: Photograph of the correlator board developed for the WBS.

spectral resolution of ≈ 12 kHz can be obtained.

A set of control signals, static control signals and dynamic control signals, are required to operate the correlator unit. The static control signals, generated by a microcontroller-based card, are used to configure the correlator unit in one of the two modes of operation. The dynamic control signals, generated by the correlator-DAS interface board, are mainly used for integration control, chip selection and data read out. Figure 2-6 shows a photograph of the correlator board developed for the hybrid WBS. The physical dimension of the correlator board conforms to 6U standard (11.025" X 9.2") and contains 64-pin and 96-pin Euro connectors for digital input and output.

2.6 Utility boards

As stated in the previous section, the control signals required for operating the correlator unit in synchronization with the data acquisition system, and configuring the spectrometer into one of the modes of operation, are generated by two utility boards: the Correlator-DAS interface board to generate the dynamic control signals and the Microcontroller-based digital input-output card to generate the static control signals. The Correlator-DAS interface board was developed for this specific application, while, the microcontroller-based I/O card, which was already available in the laboratory was adapted for this requirement.

2.6.1 Correlator-DAS Controller Board

The Correlator-DAS controller board is a MAX-7000 (EPM7128LS84) EPLD-based controller card designed to interface the 32-bit correlator output data with a 16-bit, PCI-based data acquisition system. Inside the EPLD, a state-machine-based logic is used to generate all the dynamic control signals in the proper sequence required to operate the correlator unit. The function of the dynamic control lines generated by the interface board is provided below:

1. **INT**: Indicates the beginning and end of a basic integration period (512ms, default). Integration is asserted by holding the INT pin in logic high state.
2. **CE [1....8]:** When this signal is asserted (High) for a specific correlator chip, data from the previous integration period can be read in conjunction with READ signal.

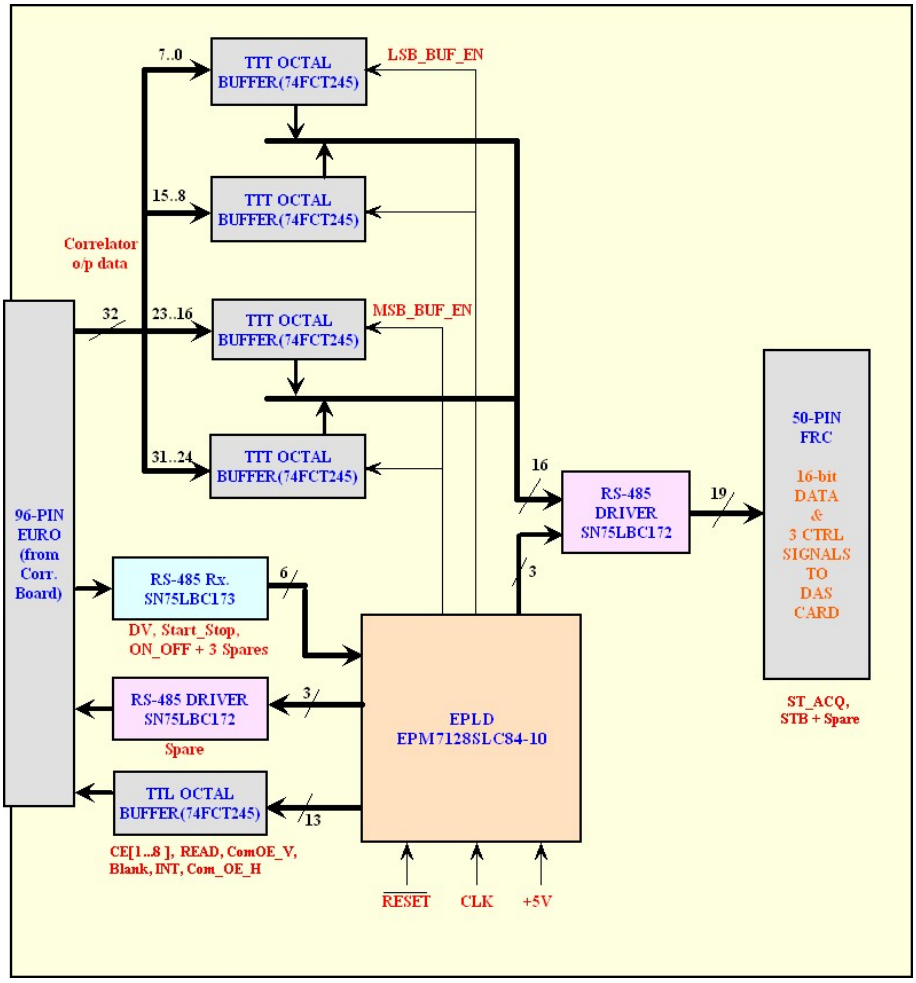

Figure 2-7: Functional overview of the Correlator-DAS interface card.

3. **READ:** This signal is common to all the correlator chips. When CE is asserted, data will appear on the 32-bit output bus on the rising edge of READ strobe. 1024 successive strobes of READ are required to output data from a chip.
4. **COM_/OE_V, COM_/OE_H:** These control lines, when asserted (active Low), enable correlator data to be read out from either V-Ch correlator board or H-Ch correlator board after an integration period. After data read out, these lines are de-asserted so that the 32-bit output lines from both correlator boards are tri-stated.
5. **BLANK:** When this signal is held high during an integration period, the overflow counters are isolated from the accumulator unit in multiply-and-accumulate unit of the correlator.

The job of the controller board is to interface the data acquisition card (DAS card) to the correlator unit. The PCI-based DAS card (RRI-PLX), which is built around a PLX-9054

chipset, contains two Spartan 2e 300k gate FPGAs for real-time signal processing and interfaces for signaling standards like RS-422and LVDS. The DAS card is mounted on one of the PCI expansion slots in the back-end control and acquisition PC. Section 3.5.4 of chapter 3 provides a detailed description of the RRI-PLX DAS card.

On the rising edge of every READ strobe, a 32-bit wide data word read out from a correlator output register appears on the input port of four octal buffers. Since, the data acquisition system is capable of transferring only 16 bits of data at a time, the controller board asserts the LSB_BUF_EN signal and the MSB_BUF_EN signal, alternately, at twice the rate of READ strobe so that the 32-bit data can be transferred to the data acquisition system as two sets of 16-bit data. Figure 2-7 shows a functional overview of the Correlator-DAS interface board.

2.6.2 Microcontroller Card

The microcontroller-based I/O card is used for the generation of the static control lines of the correlator. The static controller lines are used to configure the correlator unit into one of the two modes of operation. This card is built around AT89C2051, an 8-bit microcontroller from Atmel and consists of two 8255 for data input-output and a MAX-232 chip to interface to the PC serial port. A C program has been developed to interact with this board through the PC serial port and to set the bits required to configure the correlator into one of the two modes of operation.

2.7 Data Processing for the WBS

This section describes the major steps involved in processing the correlator data acquired by the back-end computer which contains the RRI-PLX DAS card, and finally, a flowchart indicating all the major steps involved in configuring the WBS, and operating the wideband spectrometer is presented. When the default READ strobe of time-period 9.6 μs and integration period of 512 ms is chosen, the total time required to acquire data from four correlator chips of both polarizations from the moment INT signal goes low is (9.6 μs * 1025 output registers per chip * 8 correlator chips) = 78.725 ms. The size of the data acquired at the end of each integration period can be (4Bytes per register * 1025 register per chip * 8 correlator chips) = 32 kilo Bytes. The steps involved in processing of the correlator data are:

1. **EVEN_FUNTION**: The autocorrelation function is made an even function, since, by definition, the autocorrelation function is an even function. The function is made symmetric about the first lag (zero delay: lag for which there is no delay). If the spectrometer is configured to operate in Mode-1, each of the eight, raw autocorrelation functions are converted into 2048-point even function each. If configured to operate in Mode-2, an 8192-point even function is generated for each polarization.
2. **UNBIAS**: As described in the section on the autocorrelator unit of the WBS, there is a bias in the implementation of 2-bit, 3-level correlator chip by +1. This bias is removed from the autocorrelation function according to the relation:

   $$unbias[i] = ((2 * raw\_corr[i]) - clk\_count) / clk\_count$$

   where, clk_count is the value obtained from the 1025^{th} register of the correlator chip which records the total number of correlator clock ticks during the integration period.
3. **CORRECTION**: Since the data input to the correlator is quantized to 2-bits and 3-levels only, in order to obtain the true autocorrelation function, a correction has to be applied raw correlator data. The procedure to obtain the true correlation function from the WBS data is described in section 2.7.1.
4. **SMOOTHING**: After obtaining the true autocorrelation function, the data is smoothed with a user selectable window function. The three selectable weighting functions are: Hanning window, Hamming window and triangular window [17].
5. **POWER SPECTRUM**: The windowed data is Fourier transformed to obtain the power spectrum. Fourier transformation of the windowed, corrected autocorrelation function is carried out using the FFTW [18]. FFTW is a C subroutine library for computing the discrete Fourier transform (DFT) in one or more dimensions, of arbitrary input size, and for both real and complex data.

Figure 2-8 shows the flowchart summarizing the data processing involved in the wideband spectrometer.

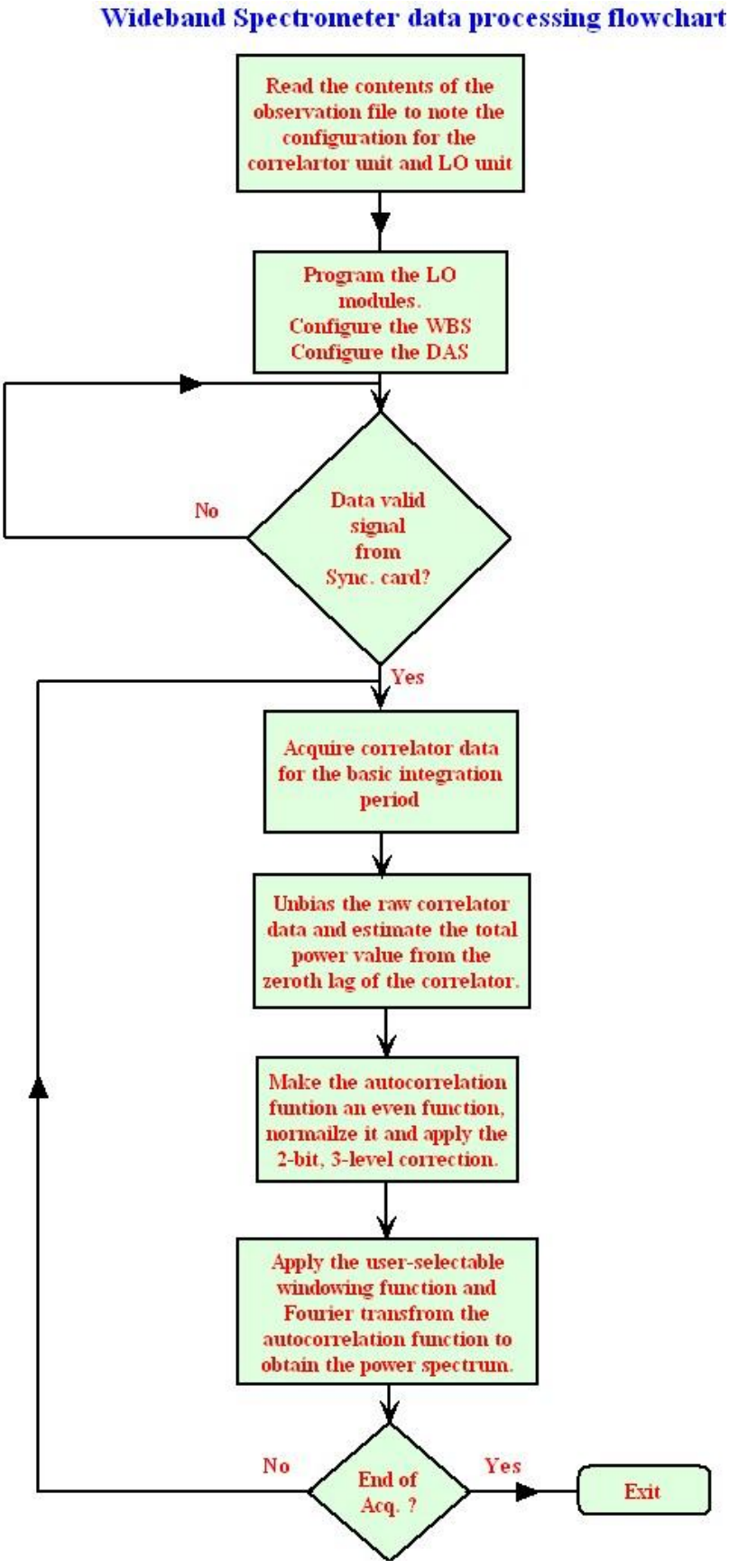

Figure 2-8: Flowchart for data processing in WBS.

2.7.1 Procedure to Obtain the True Correlation

Unlike the autocorrelation function obtained from an analog correlator which uses infinitely fine quantization, the autocorrelation function obtained from a correlator operating on coarsely quantized signal of interest is not the true correlation. The input signal has been purposefully coarse quantized in order to reduce the complexity of the correlator hardware. Since the amount of distortion is known, the true autocorrelation function can be retrieved. This methodology to obtain the true value of the autocorrelation function from a 2-bit, 3-level correlator is as per the procedure outlined by Srinivas R. Kulkarni and Carl Heiles in their paper titled "How to obtain the true correlation from a 3-level digital correlator" [19]. The procedure in [19] is summarized below:

Let $r(z)$ be the autocorrelation function of $V(t)$, as measured by a 2-bit, 3-level autocorrelator. Then, $r(z) \propto \langle Q(V(t)Q(V(t+z)) \rangle$, where, the $\langle\ \rangle$ indicates time average and $Q(V(t))$ the quantization transfer function. Let $\rho(z)$ be the corresponding quantity measured by a perfect analog correlator. Then, $\rho(z) \propto \langle V(t)V(t+z) \rangle$. Let us assume that ρ is normalized, i.e., $\rho(0) = 1$ and $r(z)$ is the ratio of the counts in the lag with delay z to the total number of samples involved in the time average. The other lags of ρ are computed as follows:

1. Compute the decision level c using the relation $\rho(0) = 1 - erf(\frac{c}{\sqrt{2}})$, i.e., $c = \sqrt{2}(erfinv[1 - r(0)])$, where, erf is the error function and $erfinv$ is the inverse error function.
2. The quantization correction is applied based on approximation $|\rho| <$ 0.86.

$$\rho(z) = Ar + Br^3;$$

where $A = (\frac{\pi}{2})\exp(c^2)$ and $B = -A^3[\frac{(c^2-1)^2}{6}]$

Figure 2-9 shows a plot of the autocorrelation function before and after quantization correction, for a noise power input to the wideband spectrometer. The autocorrelation function shown in Figure 2-9 is obtained from one of the 40 MHz bands with 1024 lags across the band. The autocorrelation function is shown for lags ranging from 1 to 2048, with

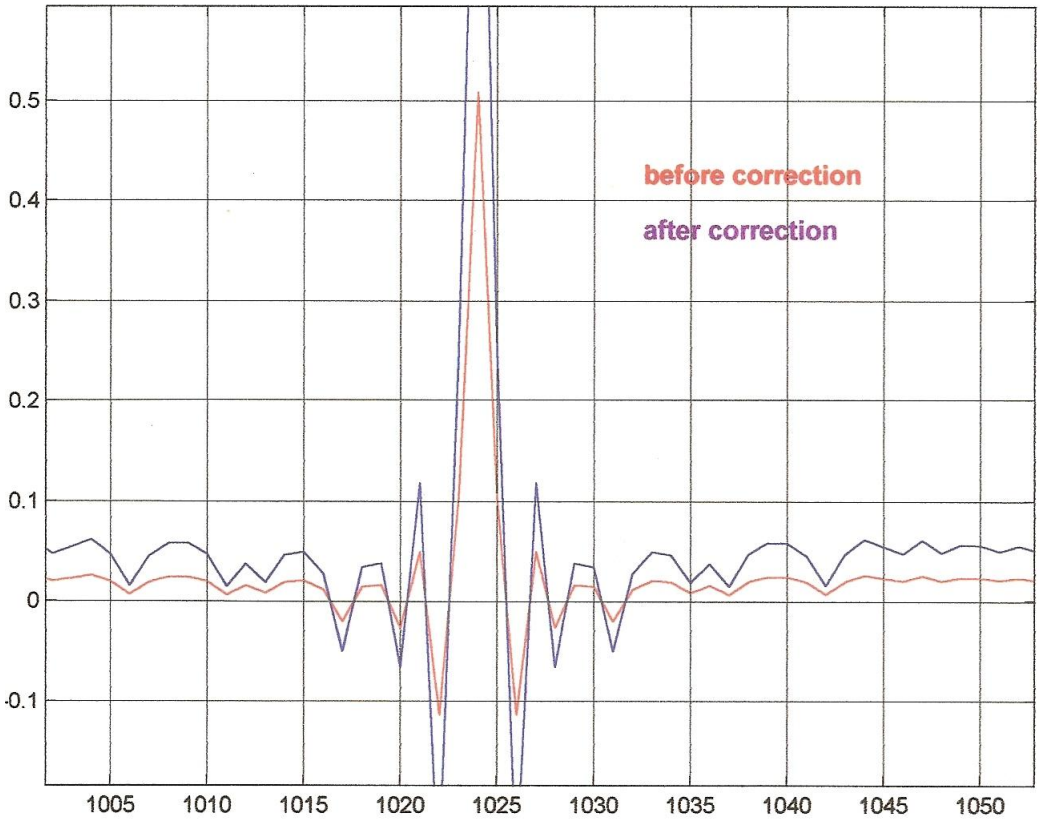

Figure 2-9: Plot of autocorrelation function before and after quantization correction.

the correlation function being symmetric about the 1024 lag. The 1024th lag corresponds to the zeroth lag of the correlator.

2.8 Tests carried out on the wideband spectrometer

The various modules of the wideband spectrometer described in the previous sections were integrated compactly within a 19” rack system. Figure 2-10 shows a photograph of the wideband spectrometer taken at the time of integrating the WBS along with other sub-systems at the 10.4 radio telescope. The 19” rack system is shown on the left-hand side of Figure 2-10. It consists of two 6U card frames: Correlator and Digitizer section (top), and Local Oscillator section. In between the two 6U card frames, an aluminum chassis containing the IF unit of the WBS is mounted. At the bottom of the 19” rack system, two power supply units which power the correlator section and the IF section are mounted one above the other.

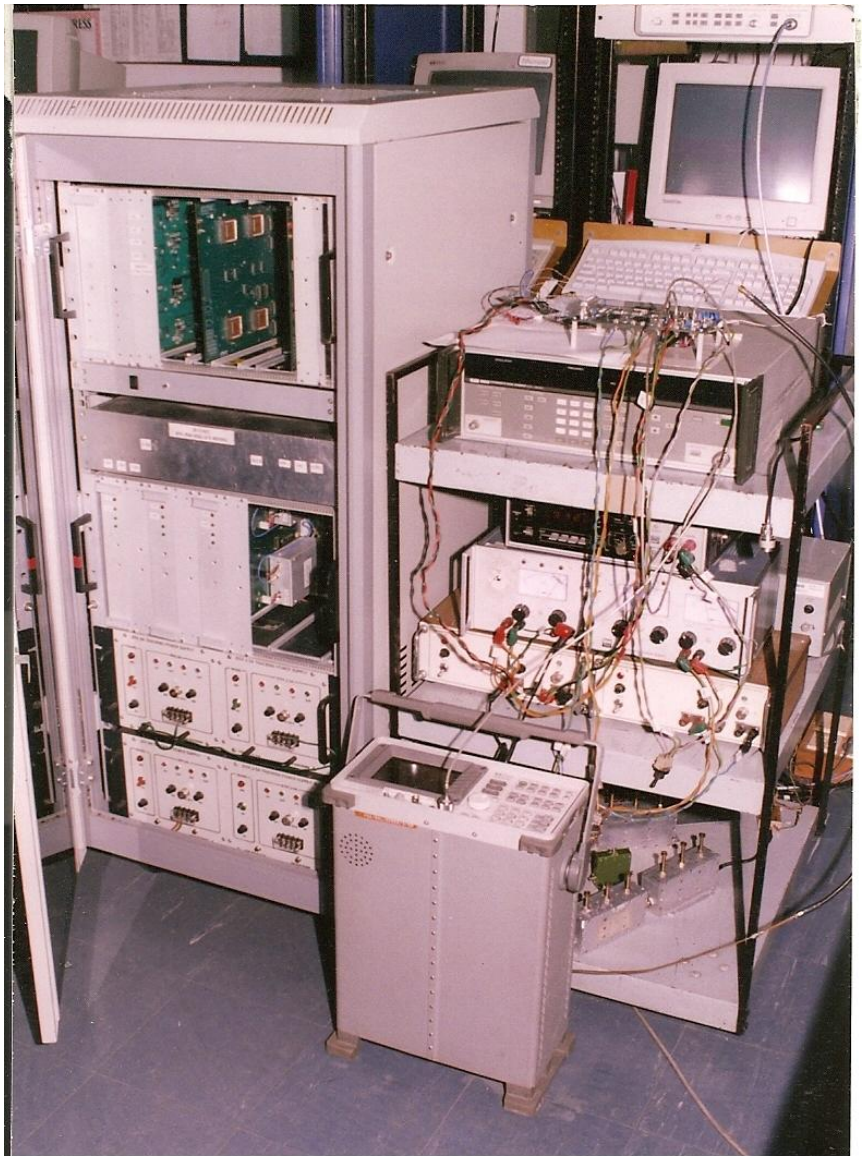

Figure 2-10: A photograph of the wideband spectrometer housed in a 19” rack system.

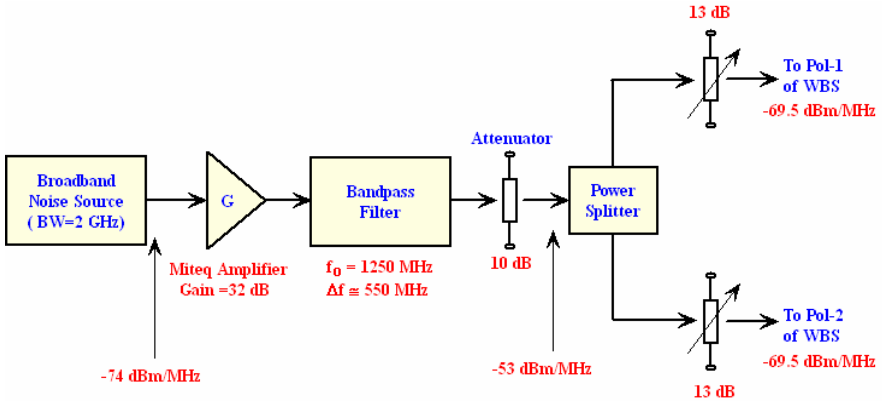

Figure 2-11: Block diagram of the noise source set up to test WBS.

Figure 2-11 shows the noise source setup that was used to test the WBS. Noise power output at ~ -70 dBm in a MHz is fed to the two polarizations of the IF unit of the WBS. The first-stage local oscillator was set to 1720 MHz and the four second-stage local oscillators were set to: 180 MHz, 220 MHz, 420 MHz and 460 MHz. So, the IF unit processed a signal of bandwidth equal to 160 MHz, centered around 1400 MHz and produced four bands of bandwidth equal to 40 MHz which are centered around 80 MHz. Figure 2-12 shows a plot of the four bands (of one polarization) obtained at the output of the spectrometer, each of bandwidth 40 MHz, centered at 1460, 1420, 1380 and 1340 MHz.

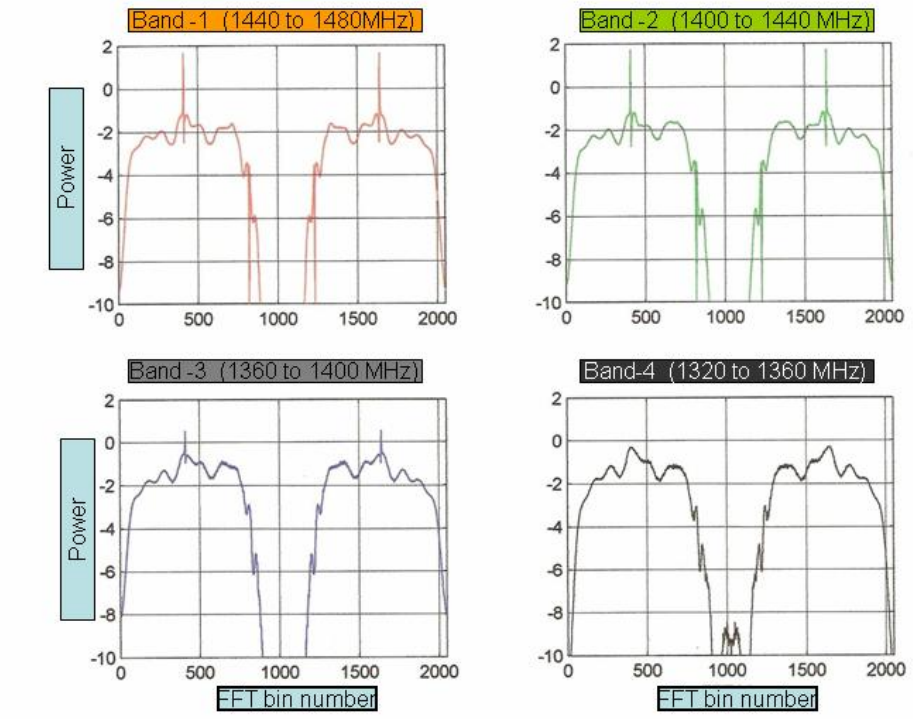

Figure 2-12: A plot of four, 40 MHz bands obtained from WBS.

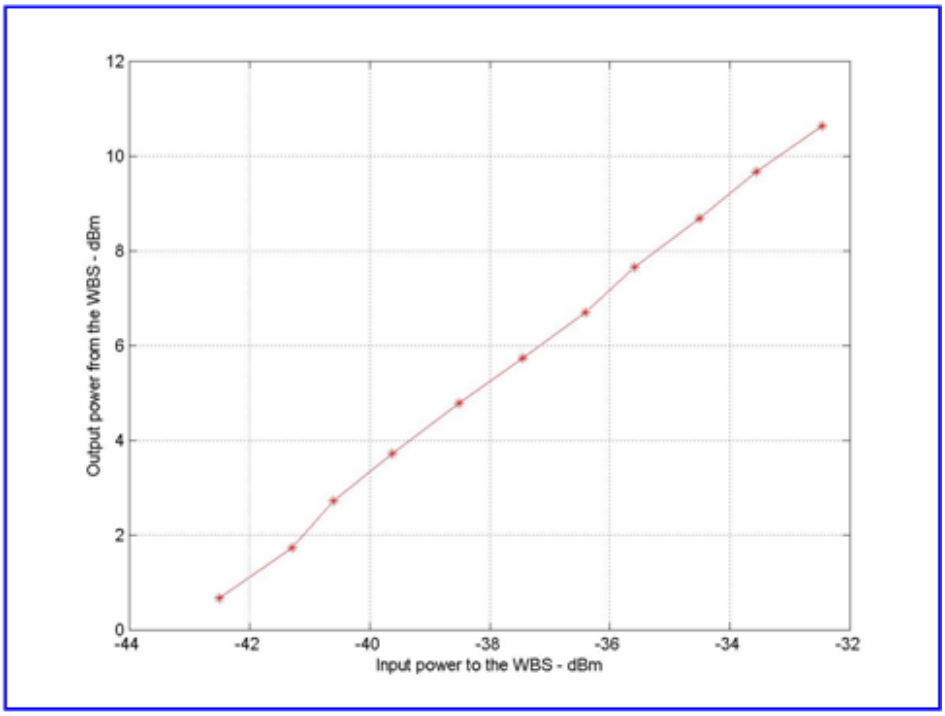

Figure 2-13: Linearity plot of the wideband spectrometer.

Figure 2-13 shows a plot illustrating the linearity of the spectrometer obtained by varying the input power level to the IF unit of the spectrometer. The output power from the WBS was obtained from the zeroth lag of the correlator (lag for which there is no delay) which by definition provides an estimation of the average power in the band of interest.

2.9 Integration of the WBS with the 10.4m radio telescope.

The Raman Research Institute operates a 10.4m radio telescope which is located on its campus. The reflecting surface is a parabolic reflector of diameter 10.4 metres. This telescope was till recently operating at 6.7 GHz for studying Methanol maser lines emanating from celestial sources in our Galaxy. Figure 2-14 shows a photograph of the 10.4m radio telescope.

The WBS was integrated with the 6.7 GHz receiver prime focus receiver of the telescope. Figure 2-15 shows a block diagram of the 6.7 GHz receiver system. The IF unit of the analog receiver carries out the downconversion of the RF at 6.7 GHz to an IF signal

Figure 2-14: Photograph of RRI 10.4 m radio telescope.

whose 3 dB bandwidth is 5 MHz, centered around 32.5 MHz. So, the downconversion section of the IF unit of the WBS was bypassed for narrow-band mode of observation. A sampling clock of 11.85 MHz is used to sample the bandpass signal, providing a 2-bit, 3-level representation of the analog signal. The correlator unit of the spectrometer computes the autocorrelation function of the digitized data which is then Fourier transformed in the back-end control and data acquisition PC as per the procedure outlined in section 2.7 of this chapter, to obtain the power spectrum.

The other major sub-system of the 10.4 m radio telescope is control PC (CPC) which interacts with the control system to facilitate pointing of the reflector to different regions of the sky. Additionally, the CPC generates three control signals: ON_OFF, Data Valid, and Start-of-Acquisition.

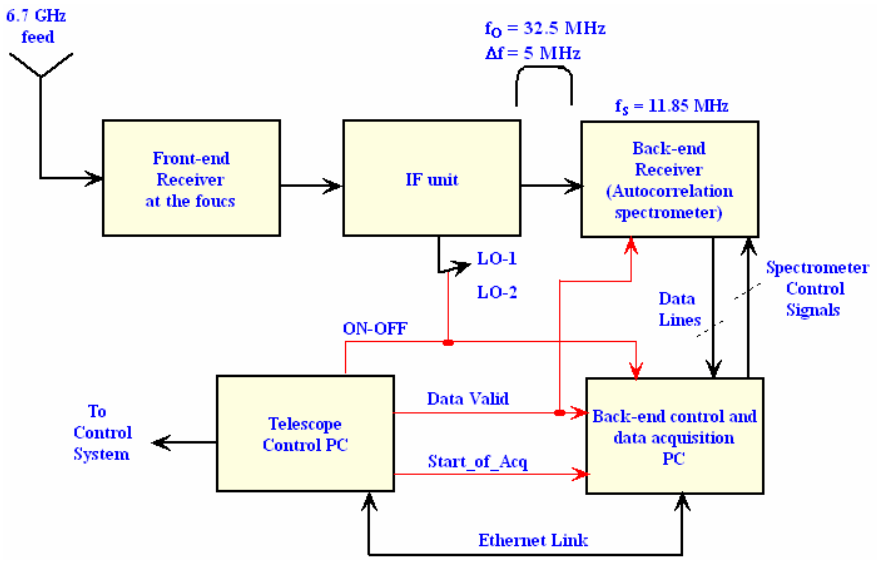

Figure 2-15: Block diagram of the 6.7 GHz receiver system at the 10.4 m radio telescope.

Essentially, most measurements in radio astronomy are done by subtracting between two situations: on source and off source. Taking data when the telescope is pointing towards a source and then switch the telescope to point towards a nearby empty sky region is one example. The purpose is to reduce the instrumental effects that otherwise overwhelm very weak signals that are being measured. One of the most difficult propositions in spectral measurements in radio astronomy is obtaining good flat baselines-parts of the spectrum with no signals. To reduce the severity of instrumental effects which give rise to a bumpy baseline, radio astronomy measurements are made using one of the three switching schemes: position-switching in which the telescope is physically steered from on-source to away from the source; beam-switching in which the antenna beam is switched from on-source to off-source, and frequency switching scheme in which the position of the source within a spectrum is moved by switching the local oscillator of the first-stage IF unit between two nearby frequencies. The 10.4m telescope implements a frequency switching scheme in which the frequency of the first-stage downconversion is switched between LO-1(5218.4462 MHz) and LO-2 (5217.4464 MHz) which is ~1MHz. The switching between two local oscillator frequencies is controlled by the ON_OFF signal coming from the CPC.

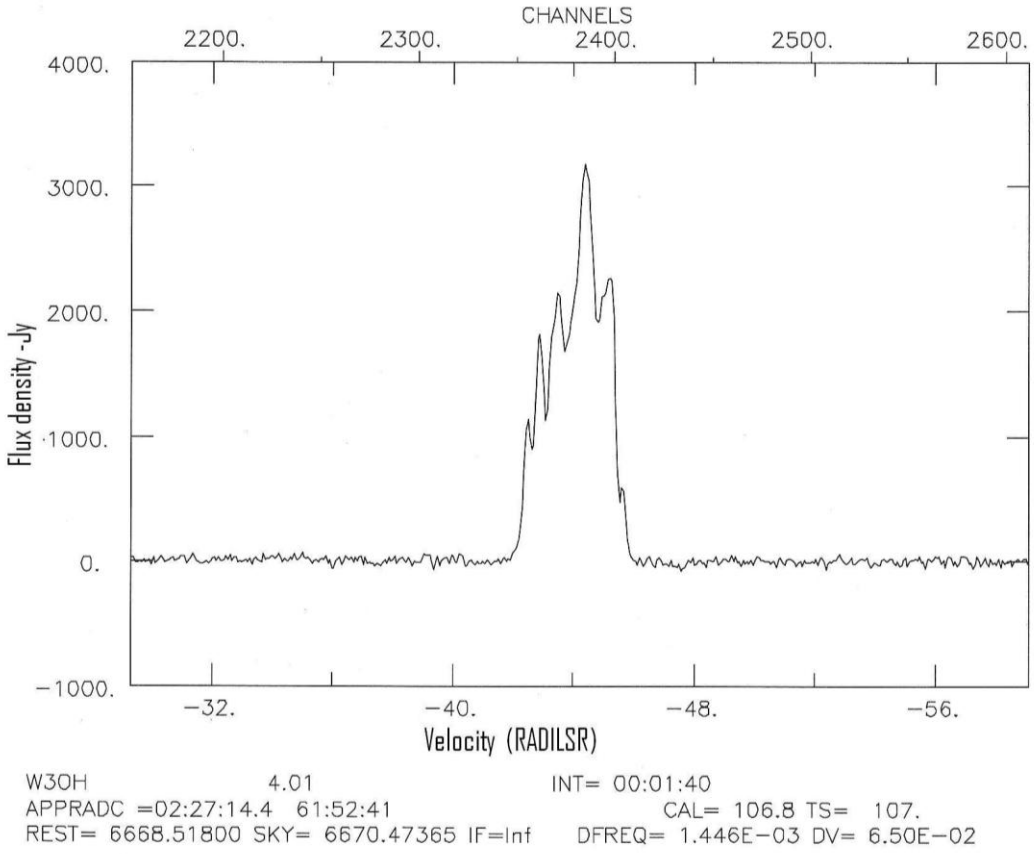

Figure 2-16: Spectrum of a maser source obtained from the wideband spectrometer.

The Data Valid (DV) signal is generated by the CPC when the telescope is tracking an astronomical source. Since this signal is connected to the INT line of the correlator unit of the spectrometer, when asserted, it allows the correlator to begin a new integration cycle (based on Start-of-Acquisition signal) consisting of a 512 ms basic integration period. The newly built spectrometer was successfully integrated with all the sub-sections of the 10.4 m radio telescope.

2.10 Results obtained from test observations using the WBS

After integrating the wideband spectrometer with the 10.4m telescope, it was configured to process signals from the 6.7 GHz front-end receiver. For maser observations, the spectrometer was required to process a narrow bandwidth of 5 MHz only with a spectral resolution of about 1.5 kHz. As mentioned earlier, the sampling clock used to digitize the 5 MHz band is maintained at 11.85 MHz. When all four correlator chips of the spectrometer

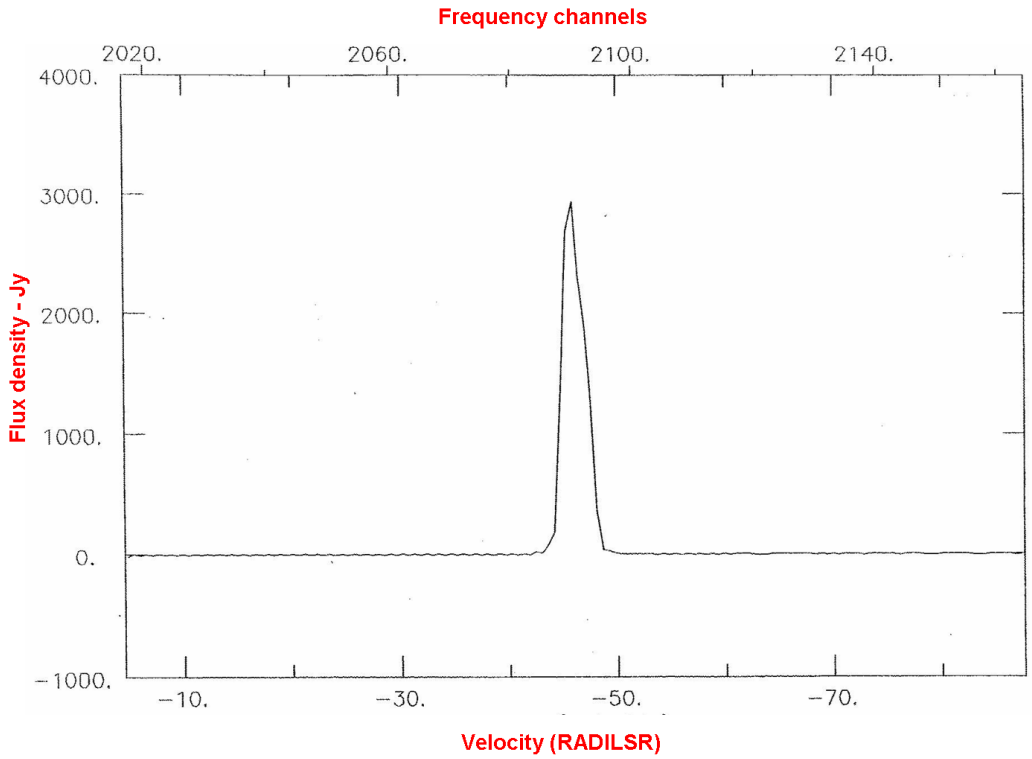

Figure 2-17: Spectrum of a maser source obtained from wideband spectrometer, operating at 100 MHz clock.

are cascaded, the spectral resolution available is 1.446 kHz. Figure 2-16 shows the spectrum of a Methanol maser source in the ultra-compact HII region (W3OH) obtained from the spectrometer which was configured for high spectral resolution, narrow band observations.

Later, the configuration of the spectrometer was changed in such a way that it could process at least one of the four 40 MHz. The 40 MHz signal centered at 80 MHz was sampled using a 100 MHz clock and was passed through the same data processing procedure described in section 2.7 of this chapter. The spectral resolution, albeit coarser for Methanol maser observations, obtained was $50*10^6 \big/ 4096 = 12.2kHz$.

Figure 2-17 shows a spectrum of the same maser source that was observed with the spectrometer configured to process a bandwidth of 40 MHz with a spectral resolution of 12.2 kHz. It is clearly seen that because of coarser spectral resolution, the spectrum in Figure 2-17 does not show the fine finger-like features of the maser lines which are clearly seen in Figure

2-16. This exercise was to demonstrate the functioning of the spectrometer in cascaded mode of operation (at 100 MHz clock).

2.10.1 **An unbiased survey of the galactic plane for 6.7 GHz methanol masers configuring the WBS for narrow bandwidth observation.**

An unbiased survey of the Galactic plane, searching for 6668.518 MHz maser emission of methanol using the 10.4m telescope has been undertaken by Prof N. Udaya Shankar, K. R. Vinod and Dr B. Ramesh. The observations were made in the frequency switching mode with the 4096-channel spectrometer configured to process a narrow bandwidth of 5.92 MHz. This survey proposed to cover a region of the Galactic plane from 320° to 80° in the Galactic longitude and -0.5° to +0.5° in the Galactic latitude (parts of the fourth and first quadrants). The half power beam width of the 10.4m telescope at 6.7 GHz is 18 arcmin. The telescope was moved in steps of 15 arcmin in longitude and also in latitude, and each location was observed for 2 hours. This gives a velocity resolution of 0.065 Km/s. The system noise temperature is around 110 K and the antenna gain is around 60 Jy/K. A, two hour integration gives a noise floor of 2.65 Jy and hence a 3σ detection level of ~9 Jy. They have already surveyed the required 120° longitude strip at Galactic latitudes –0.125° and +0.125°. Out of the 960 pointings, 150 detections have been made. Some of these are already known in the literature and many (minimum of 20) are probably new detections.

Section - B

A spectrometer based on direct L-band digitization

2.11 Introduction to a direct RF/IF digitization

An analog-to-digital converter is a critical component in a radio receiver design [20]. It is used to convert a continuous-time input voltage into discrete output levels which are represented by binary coded words. Advances in the development of ADCs, and the availability of increasingly faster and less expensive digital hardware are resulting in more of the traditional analog functions of a radio receiver being replaced with digital hardware. The trend in receiver design is evolving towards this goal by incorporating digitization closer and closer to the receive antenna at increasingly higher frequencies and wider bandwidths. While an intermediate frequency (IF) sampling receiver is one that utilizes an ADC to sample the analog signal before it is converted to baseband, a direct RF sampling receiver, as a logical extension of IF sampling, digitizes the RF signal without first mixing the signal down to a lower intermediate frequency. In direct RF sampling applications, there is little analog signal processing between the antenna and the converter. However, there are many concerns that need to be addressed when sampling at high carrier frequencies. The two important concepts in direct RF sampling are aperture width and aperture jitter.

The aperture width is the effective time duration over which the carrier signal gets averaged to produce a given ADC output. The width of this window is inversely proportional to the maximum input bandwidth that the ADC can accommodate. So, if a higher frequency carrier is input, then the ADC's averaging process will significantly degrade the strength of the sampled signal.

Aperture jitter or aperture uncertainty is the sample-to-sample variation in the encode process of an ADC which can be caused externally by jitter in the sampling clock, and internally by the sampling switch which does not open at precise times. Aperture jitter causes the ADC to sample at a different phase of the carrier wave than assumed which can lead to signal power loss and carrier phase measurement errors.

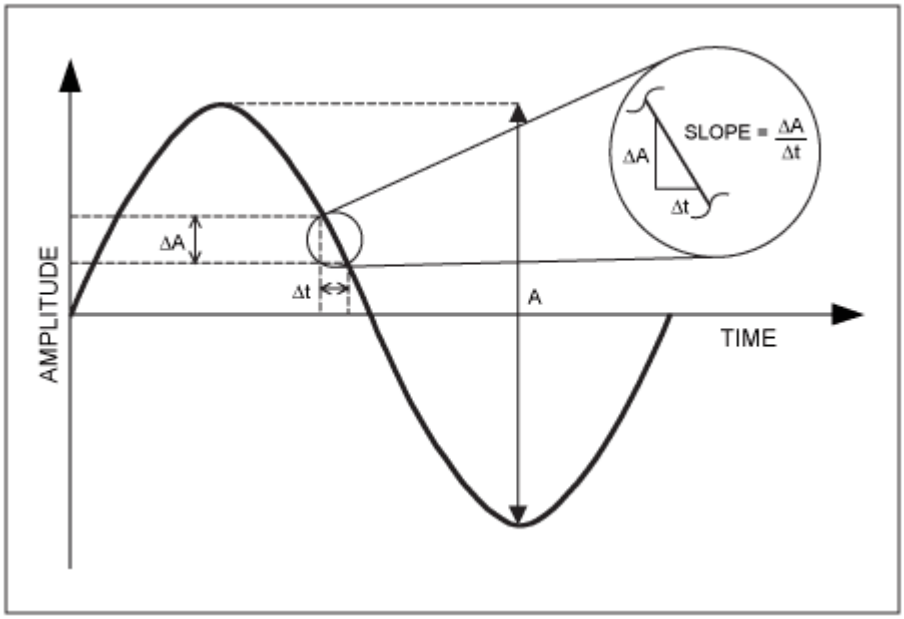

Figure 2-18: Uncertainty in sampling time due to aperture jitter.

As depicted in Figure 2-18, uncertainty in sampling time Δt is equated to uncertainty in amplitude ΔA. This results in false sampling of the analog input amplitude, thus degrading the SNR of the ADC. The theoretical SNR for an ADC as limited by aperture uncertainty is determined by the following equation [21]:

$$SNR = -20\log[2\pi f_{in} t_{jitter}]$$

where, f_{in} is the input analog frequency and t_{jitter} is the RMS jitter in the sampling clock. This equation provides much insight into the noise performance that can be expected from a data converter. The rule of thumb is that the RMS jitter be low enough so that the SNR due to clock jitter does not affect the SNR due to quantization noise of the data converter.

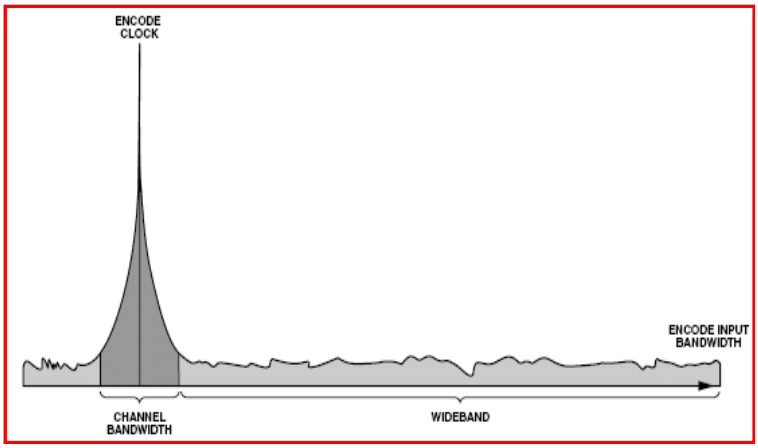

Figure 2-19: A typical spectrum of an encode signal.

When sampling at high carrier frequencies, clock purity is of extreme importance. The aperture uncertainty shows up as wideband noise in the sampled spectrum. Figure 2-19 shows the typical spectrum of an encode signal from dc to the encode bandwidth of the ADC [21]. So, the clock input port of an ADC should be regarded as the local oscillator port of the ADC, not a digital control signal. As is the case with a mixer, the input signal is multiplied with by a local oscillator, which in this case is the sampling clock. Since multiplication in time-domain is equal to convolution in the frequency-domain, the clock signal is convolved with the desired analog input signal causing the spectral shape of the clock signal to be expressed on the analog signal. As the ADC is a sampling system, all the wideband noise on the clock port of the ADC will be aliased into the band of interest thereby, degrading the SNR.

2.12 Bandpass Sampling for Direct Digitization

The sampling process is of critical importance in radio receivers using digitization at RF or IF. The content of the resulting sampled signal is highly dependent on the relationship between the sampling rate employed and the minimum and maximum frequency components of the analog input signal. While sampling of low-pass signals at rates equal to $2f_{max}$ where, f_{max} is the highest frequency component present in the signal, often referred to Nyquist sampling is not the only sampling scheme used in practice, another technique known as bandpass sampling is used to sample a continuous bandpass signal that is centered about some frequency other than zero Hz. Sampling at rates lower than $2f_{max}$ can still allow for reconstruction of the information content of the analog signal as long the conditions (for acceptable uniform sampling rates) described by equations (2-1) and (2.2) are met.

While bandpass sampling has the advantage of downconversion without the use of mixers-due to the intentional aliasing of the signal band resulting in an inherent translation to baseband position-the noise from all the aliased bands is combined into the baseband [22]. Even with an ideal anti-aliasing filter, the SNR is not preserved for bandpass sampling owing to the thermal noise contributions from the aliased spectra between dc and at least the original bandpass spectral location. This is in contrast to analog mixing process in which the signal-to-noise ration is ideally preserved. When a continuous input signal's bandwidth and center frequency permit us to do so, bandpass sampling may not only reduces the speed

requirement of ADCs below that necessary with traditional low-pass sampling, it also reduces the amount of digital memory necessary to capture a given time interval of a continuous signal.

2.13 Choosing an ADC for a Direct Digitization Spectrometer

In this section, some of the important specifications that need to be considered while choosing an ADC for broadband applications have been described [23]. The integration of ADC functionality into consumer equipment has been influencing the converter market with ADCs in many ways being treated like application specific integrated circuits. Apart from cost of the converter, there are a few key specifications of interest like: number of ADC bits (resolution), the analog input bandwidth, signal-to-noise ratio (SNR), spurious-free dynamic range (SFDR), signal-to-noise ratio and distortion (SINAD), power consumption and sample rate that can be used to select the right ADC for a given application [24]. These specifications are in addition to the general specifications like: digital output signaling standards, ease of configuration, looking for plots showing the device performance as a function of analog input frequency, frequency of sampling clock, temperature and supply voltages, checking for specifications under the same condition in which the device is likely to be used, etc. Also, the radio frequency interference (RFI) scenario in and around the operating frequency band needs to be taken into account in order to asses the linearity that can be provided by the ADC and estimate the actual number of ADC bits available for representing the signal of interest.

2.13.1 ADC Bit Resolution and Input Power

A converter has a physical number of bits that usually corresponds to pins on the device. These are sometimes referred to as “marketing bits” or “resolution”. However, performance may or may not correspond to these physical bits. Typically, performance bits are fewer than the number of marketing bits. These bits are often called Effective Number of Bits (ENOB). To evaluate the number of bits necessary in an ADC system, the dynamic range of the input signal to the ADC has to be analyzed by carrying out a survey of the spectrum at the site where the radio telescope is likely to come up. Ideally, a radio telescope should receive only the very weak sky noise and a 2-bit or a 3-bit representation of the sky signal could be sufficient to describe it. But, due to the presence of stronger man-made RF

signals (called RFI if they fall in a protected frequency band) increase in the received power has to be taken into consideration to avoid saturation of the converter.

2.13.2 Input Bandwidth

In order to accurately sample high frequency signals, high analog bandwidths are required. Typically, in ADCs, the sampling mechanism is a capacitor and a switch. Converter bandwidth is largely determined by the value of the switch resistance (R) and the sample capacitor (C). So, to maximize input bandwidth, both R and C should be minimized. But, wider input bandwidth allows more noise to pass the ADC input stages and be digitized, resulting in lower SNR than would be for a lower bandwidth ADC. Therefore, for a given design, SNR is inversely proportional to bandwidth. This is one of the key reasons why high bandwidth converters have fewer SNR bits than the total resolution of the ADC. Conversely, wider input bandwidth allows for better slew-rate performance and more accurate tracking of the fast slewing analog signals associated with both transient events and high-frequency sine waves. It also allows wideband analog signals to be accurately sampled by the accompanying faster sampling rate.

While, for optimal spurious performance, a wide input bandwidth is desirable, the increased bandwidth with smaller C allows more noise to enter the front-end of the ADC and be spread across the Nyquist spectrum resulting in the degradation of SNR. Thus, SNR and SFDR must be traded for one another. Usually, the input bandwidth specification is representative of the flatness of the ADC response versus input frequency and is not an indication that the device will hold the performance up to those input frequencies. Hence, it is important to note the manufacturer's specifications for SNR, SFDR and ENOB for different input RF frequencies and sampling clocks, as these dynamic specifications of the ADC decreases at higher frequencies because the effects of jitter get worse. The other issue that crops up with higher analog bandwidth is that of interfacing the analog input to the ADC. For higher intermediate frequencies (IFs) and direct RF sampling applications, proper impedance matching to the source becomes more critical. At high frequencies, optimal ADC performance is achieved when a proper match exists.

2.13.3 Power Dissipation

Although usually not considered directly as a performance metric, power consumption does factor into most ADC figure-of-merit calculations, indicating that the lower the power, the better the figure-of-merit. While ADC power consumption is of serious concern in hand-held devices, it does affect the overall power budget of a receiver system. The thermal management of the ADC needs to be taken care of by providing a suitable heat-sink, maintaining the specified air-flow (if forced cooling is required), and constantly monitoring the converter's temperature so that a suitable action can be taken if the device's temperature exceed specified limits.

2.13.4 Sampling Rate

Typically, a converter's best performance is limited to the first two Nyquist zones, confining the input frequency of the ADC to being less than the maximum frequency of the sampling clock specified by the manufacturer. As the maximum frequency of the sampling clock for high-speed analog-to-digital converter increases, so does the width of the Nyquist zones. Additionally, for converters with a higher maximum sampling rate, the analog anti-aliasing filters have more room for transition from pass-band to suppression than for a lower sampling-rate device, thereby, easing the requirements of the filter. Higher sampling rates improve noise performance of the ADCs. While the overall integrated noise does not improve, the distribution of the noise over wider bandwidth does offer improvements in noise spectral density (NSD). This process is often referred to as processing gain and is nothing more than distributing the same noise power over a wider band of frequencies.

2.14 Requirements and Specifications of the Spectrometer

Considering all the points discussed in the previous section and our requirement of an ADC capable of sampling RF signals in the L-band, we procured and evaluation board EB7610 from Signal Processing Technologies, USA for our spectrometer. It must be emphasized that, during the time the design of a direct digitization spectrometer was conceptualized, procuring such an ADC from outside was an arduous task. The board contains SPT7610 analog-to-digital converter which is a parallel flash converter, capable of digitizing full-scale voltage of 0 to -1V input into six-bit digital words at an update rate of 1 Giga samples per second with a power dissipation of about 3W. The small-signal analog

bandwidth of the ADC is typically 1.4 GHz. The bit resolution of the ADC was not a major concern because RFI is not a serious issue when processing RF signals around 6-7 GHz. Also, we only required 2 bits since the downstream processing unit was the same 2-bit, 3-level NASA correlator unit. The ADC thermal issue was addressed by a heat-sink with a small fan mounted on the chip. The important specifications of the spectrometer when configured to a narrowband observation mode are:

1. Maximum instantaneous observation bandwidth = **50 MHz,** as the maximum clock frequency of the correlator is 100 MHz.
2. Digitizer resolution = **2-bit, 3-level derived from a 6-bit ADC.**
3. Maximum number of correlator lags per polarization = **4096 (in cascaded mode).**
4. Typical on-board accumulation = **512 ms**.
5. Raw spectral resolution **= 12 kHz.**

2.15 Description of a Direct L-band Digitization Spectrometer

This section describes a digital autocorrelation spectrometer based on direct digitization of RF signals in the L-band. The spectrometer is built around EB7610 ADC evaluation board and a 4096-channel autocorrelator unit described in section 2.5. The block diagram of the direct digitization spectrometer is as shown in Figure 2-20. The high-speed ADC digitizes an analog signal of bandwidth 12 MHz (3-dB), centered at 1450 MHz, using an effective sampling clock of 62.5 MHz. Since the plan was to observe Methanol maser

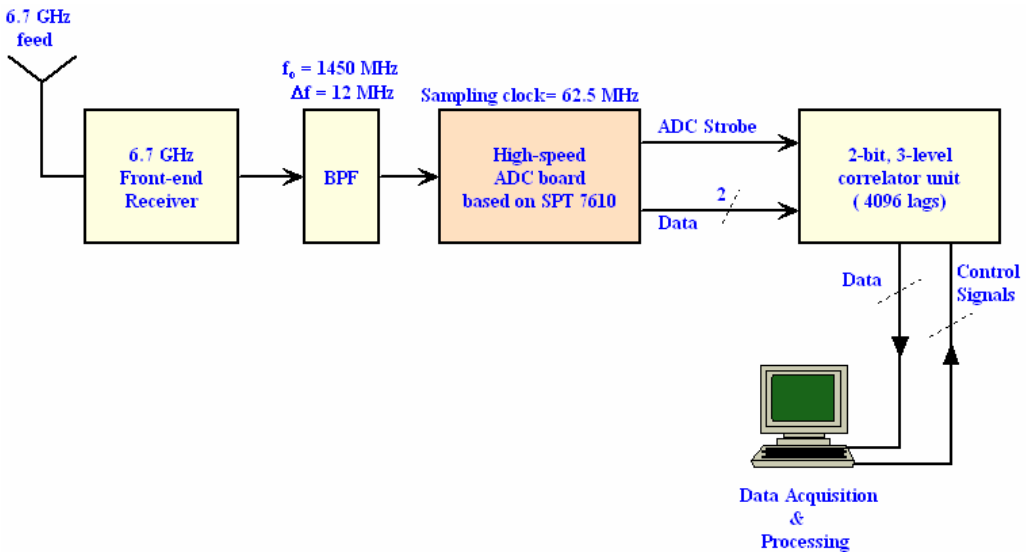

Figure 2-20: Block diagram of the direct digitization spectrometer.

sources, a bandpass filter of bandwidth equal to 12 MHz was chosen as it was readily available in the laboratory. The sampling clock is derived from a synthesized signal generator referenced to the observatory reference. Two, optimally selected bits from the ADC, are coupled to the ADC-Correlator interface board to present the chosen bits in a form suitable to the 2-bit, 3-level correlator unit. A spectrometer produces power-spectra with a raw spectral resolution of about 7.629 kHz.

2.16 Test Results from Direct L-band Digitization Spectrometer

The ADC evaluation board was integrated with the correlator unit and the correlator unit was configured to process a narrow bandwidth signal (12 MHz) for Methanol maser observations at 6.7 GHz. Figure 2-21 shows a spectrum of the same maser source that was observed using the hybrid wideband spectrometer. This allowed us to compare the results obtained from direct RF digitization at L-band and the hybrid spectrometer involving additional stages of downconversion. It may be recalled that the spectral resolution of the hybrid spectrometer configured for narrow band mode was 1.44 kHz while the resolution in the 40 MHz band in cascaded mode was 12 kHz. The spectral resolution obtained with the direct digitization based spectrometer was 7.6 kHz, which is somewhere in between the spectral resolutions of the configurations mentioned above. The 7.6 kHz spectral resolution is

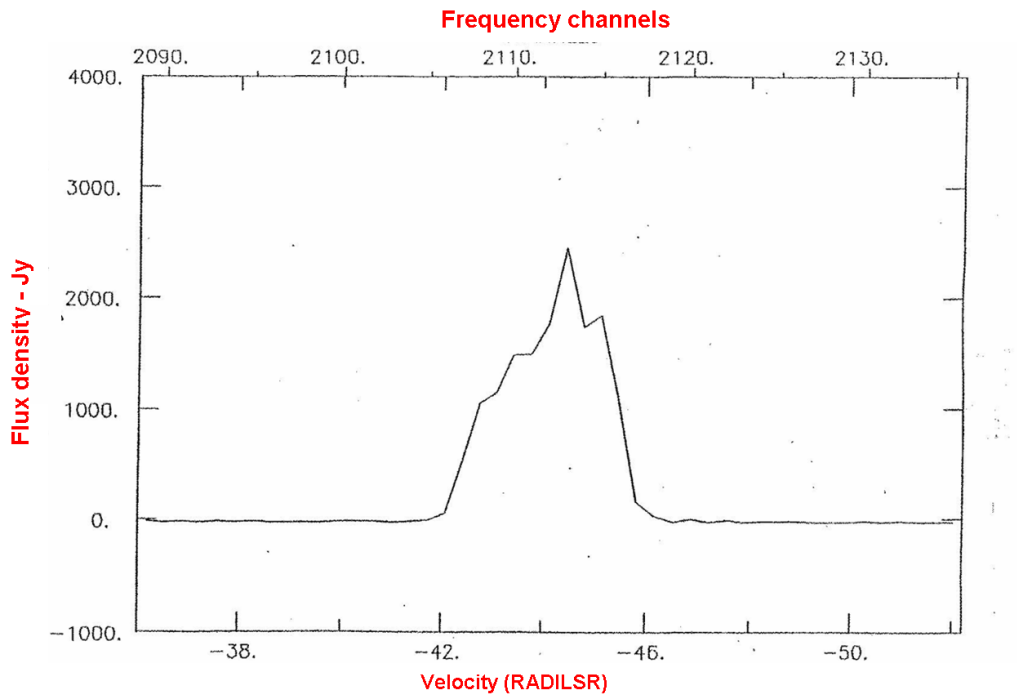

Figure 2-21 Spectrum of a maser line observed using the direct digitization spectrometer.

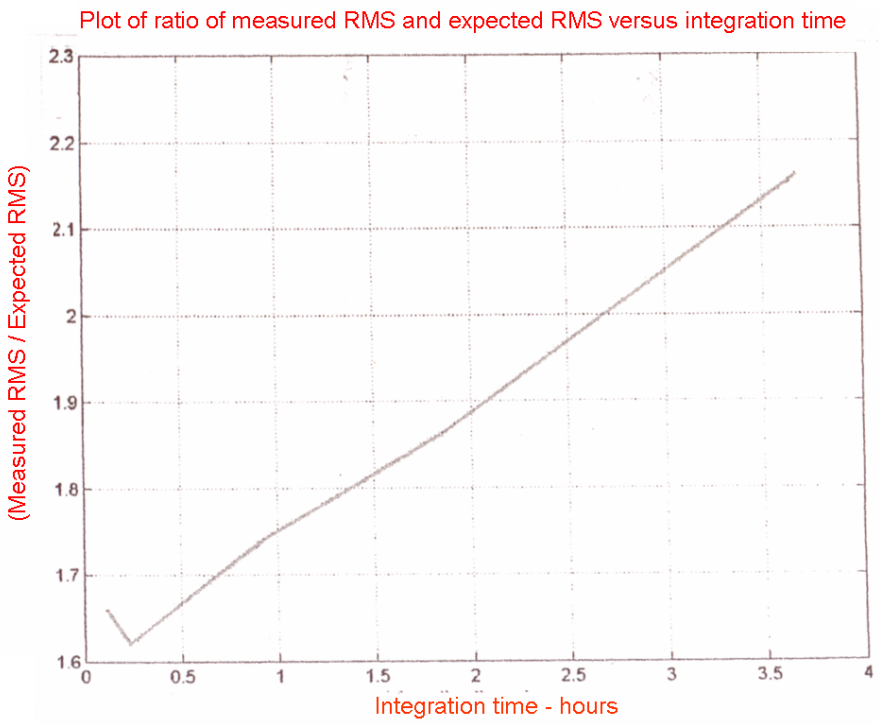

Figure 2-22: A plot of ratio of measured rms to expected rms.

entirely due to the 62.5 MHz sampling clock, which in turn is decided by the centre frequency and bandwidth of the anti-aliasing filter prior to the ADC. So, even though the finger-like features of the maser line are not as clearly visible as in Figure 2-16, however, it does show some features of the spectral-line source. The rms noise in the spectrometer is given by: $1/\sqrt{\beta\tau}$

where, β is the spectral resolution (7.629 kHz) and τ is the integration time. For a basic integration time of 512 ms, the rms noise in the measurement is 0.016. For a system temperature of 130 K, and a conversion factor of 55 Jy per Kelvin, rms in the measurement of flux density is 110 Jy.

Figure 2.22 shows a stability plot of the direct digitization spectrometer in which a ratio of measured rms noise from the spectrometer to the theoretical expected rms noise is plotted as a function of integration time. At the end of 3.5 hours of integration the minimum detectable flux density improves by a factor of about 150, from 110 Jy (for 512 ms integration time) to about a Jy.

Chapter 3

Chapter 3

A Direct Voltage Recording System for 50 MHz Observations at GMRT

3.1 Introduction to the Giant Metrewave Radio Telescope

This section provides a brief introduction to the Giant Metrewave Radio Telescope (GMRT) and its receiver chain. The GMRT, which is located near Pune in India, is the world's largest array of radio telescopes at metre wavelengths [25]. It consists of an array of 30 antennas, each antenna is 45 m in diameter, and has been designed to operate at a range of frequencies from 150 MHz to 1450 MHz. The GMRT has a hybrid configuration in which 14 of the 30 antennas are randomly distributed in a central square (~1 km across), while the remaining 16 antennas are distributed in a roughly Y-shaped configuration, with the length of each arm of the Y being ~14 km. The maximum baseline length between the extreme arm antennas is ~ 25 km. The GMRT operates five different receivers in five frequency bands centered around 150, 230, 325, 610 and 1420 MHz. The feeds are mounted on four faces of a feed turret placed at the focus of the antenna with the provision to rotate the turret so that the required feed points to the vertex of the antenna. The feeds for 230 MHz and 610 MHz co-exist on one of the four faces of the turret.

3.1.1 GMRT Analog Receiver Chain

The signals from all five feeds, after the first-stage RF amplification, are fed to a common second-stage amplifier called the “Common Box” [2]. The “Common Box” has an input select switch allowing the user to choose which RF amplifier's signal is to be selected, and then converted to IF. The first local oscillator (I LO, situated at the base of the antenna, inside a shielded room) converts the RF band to an IF band centered at 70 MHz. After passing the signal through a bandpass filter of selectable bandwidth (5.5 MHz, 16 MHz, 32 MHz), the IF at 70 MHz is then translated (using II LO) to a second IF at 130 MHz and 175 MHz for polarization-1 and polarization-2, respectively. The maximum bandwidth available at this stage is 32 MHz for each channel. This frequency translation is done so that signals for

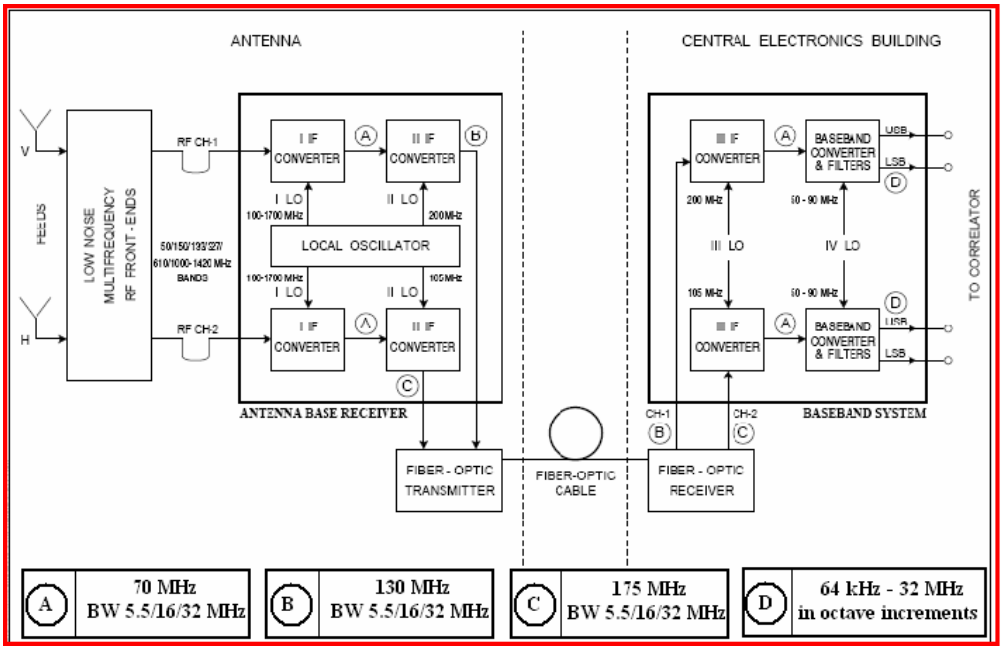

Figure 3-1: Schematic diagram of the GMRT receiver chain [2].

both polarizations can be frequency division multiplexed onto the same fiber for transmission to the central electronics building (CEB). At the CEB, these signals are received by the Fiber-Optic Receiver and the 130 and 175 MHz signals are then separated out and sent for baseband conversion. The baseband converter section converts the 130 and 175 MHz IF signals first to 70 MHz IF (using III LO), these are then converted to upper sideband (USB) and lower sidebands (LSB), each, at most 16 MHz wide at 0 MHz using a tunable IV LO. There are also two Automatic Level Controllers (ALCs) in the receiver chain. The first ALC is just before the Fiber Optic transmitter and the second is at the output of the baseband unit. Control and telemetry signals are also transported to and from the antenna on the fiber-optic communication system. Each antenna has two separate fibers for the uplink and downlink. Figure 3-1 shows a schematic diagram of the GMRT receiver chain.

3.1.2 GMRT Hardware Correlator (GMRT-HC)

The principal back-end used for interferometric observations is a 32 MHz bandwidth FX correlator, providing a maximum of 256 spectral channels for each of the two polarizations for each baseline. The 6-bit data from the ADC is rounded off to 4 bits and fed to the FFT sub-section after delay compensation. In the FFT sub-section, a data weighting function can be applied to the 4-bit time series and then Fourier transformed. The hardware FFT engine is implemented using an ASIC.

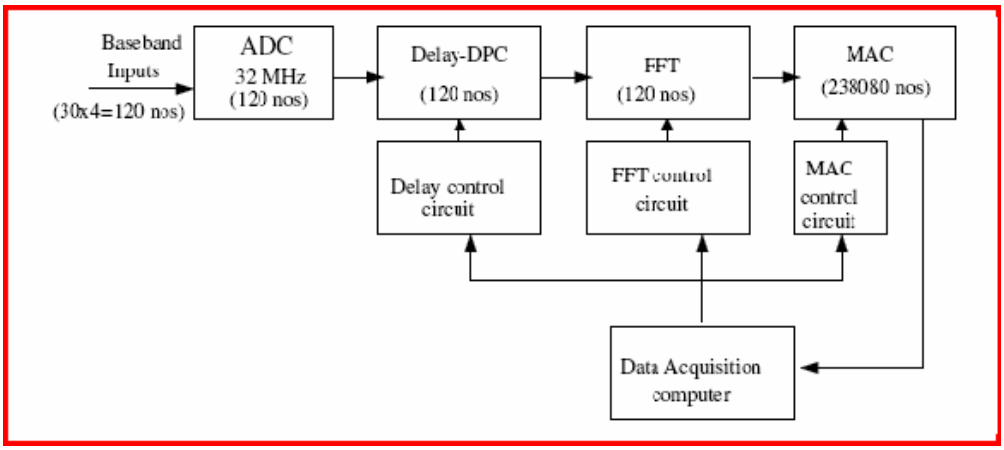

Figure 3-2: A simplified block diagram of the GMRT correlator [2].

The maximum length of the FFT is 512 points which provides 256 spectral channels at the output. The multiply-and-accumulate (MAC) unit, which is also an ASIC, takes the FFT outputs and computes the self- and cross-correlations and accumulates these products for an integration period ranging from 4 ms to 128 ms (short-term accumulator, STA). Although the integration time can be as short as 128 ms, long term accumulation makes the shortest integration time to be around a second. The FX correlator itself consists of two 16 MHz wide blocks, which are run in parallel to provide a total instantaneous observing bandwidth of 32 MHz. For spectral line observations, where fine resolution may be necessary, the total bandwidth can be selected to be less than 32 MHz. The available bandwidths range from 32 MHz to 64 kHz in steps of 2. The maximum number of spectral channels however remains fixed at 256, regardless of the total observing bandwidth. Figure 3-2 shows a simplified block diagram of the GMRT correlator.

3.1.3 GMRT Software Correlator (GMRT-SC)

In addition to a digital hardware correlator, GMRT also has a software back-end in which the baseband signals of bandwidth 16 MHz from each antenna are digitized using 8-bit ADCs, raw voltages transformed by a 1024-point FFT engine, and the self- and cross-correlations computed across a cluster of computers (48 nodes). The software correlator provides a visibility spectrum which is approximately one second averaged and has 512 spectral channels across a 16 MHz band, thereby, providing an improvement in spectral resolution by a factor of two over the GMRT hardware correlator.

3.2 Need for a Direct Voltage Recording System

The Raman Research Institute (RRI) has designed and developed a low-frequency V-dipole feed with a plan to equip GMRT with low frequency receiver system, operating in the frequency range 40-80 MHz. Four of the thirty GMRT antennas were equipped with the V-dipole feed. They are: C04, C11 (in the central square) and E02 and W02 in the eastern and western arm, respectively. The evaluation of the feeds installed on these four GMRT antennas was carried out using low frequency front-end receiver (developed by RRI) to observe in a narrow band of frequencies in the frequency range 40-80 MHz. In practical systems, besides the noise from the receiver itself, there will other sources of system noise: the spillover noise of the antenna which consists of ground radiation that enters the system through the side lobes, and noise produced by unavoidable attenuation in transmission media (like waveguides, coaxial cables) connecting the feed to the receiver input all contribute to the total receiver output. Therefore, it is necessary to integrate the receiver output over a certain time interval in order to get a reasonable signal-to-noise ratio. Ideally, if there is only white noise (uncorrelated noise) in the system, the signal-to-noise ratio will increase as the square root of the integration time. This means that, given a receiver with a certain system noise temperature T_{sys} and noise bandwidth β, one can reduce the uncertainty in the estimation of system noise temperature, Δt, by simply increasing the integration time:

$$\Delta t = T_{sys} \Big/ \sqrt{\beta \tau} \tag{3.1}$$

If the total receiver bandwidth of a receiver is $\Delta \nu$, then two samples taken at time less than $\Delta t = 1 \Big/ \Delta \nu$ apart are not independent. A total integration period of τ contains $N = \tau \Big/ \Delta t = \tau . \Delta \nu$ independent samples. For Gaussian statistics, it is known that the total error for N samples is $1 \Big/ \sqrt{N}$ of that of a single sample. However, in practice, one will have to deal with two other kinds of noise: the flicker noise ($1 \Big/ f$) and a low-frequency drift noise (correlated noise). There is an optimum integration time called as “Allan” time which marks the crossover from white noise to 1/f-noise and drift and is the maximum integration time for the receiver. Integrating longer than the Allan time will result in the worsening of the signal-to-noise ratio.

Test observations carried out at GMRT showed that $\sqrt{\beta\tau}$ improvement was not forthcoming when observed using the existing GMRT receiver chain, described in section 3.1. This could possibly be due to systematics, RFI, cross-talk in the analog signal conditioners and correlators. To study if this limitation can be overcome by digitizing the output of the low frequency front-end receiver right at the antenna base, we developed a direct voltage recording system (RRI-DS) to record the raw voltages at two antenna bases and cross-correlate them off-line in a computer. Simultaneous test observations on astronomical sources were carried out at 55 MHz using GMRT hardware correlator, GMRT software correlator and the direct voltage recording system. At an antenna base, the direct voltage recording system tapped the signal to be digitized and recorded (from the GMRT receiver chain) in such a way that it did not hinder simultaneous observations along with the existing GMRT correlators which are present at the central electronics building. This allowed us to compare the SNR improvements obtained from the three correlators.

3.3 Requirements of the Direct Voltage Recording System

Two direct voltage recording systems had to be set up at two GMRT antennas where the V dipole feeds were mounted. For each antenna base, an ADC capable of digitizing an analog signal of bandwidth ~5.5 MHz at a sampling rate of about 11 MHz had to be developed. A recording system at each antenna, capable of sustaining a data rate of about 22 Mbytes per second (MBps) (11 MBps * two polarizations) for at least 5 hours, had to be developed. Since the antennas are physically spaced apart, a synchronizing mechanism had to be worked in which the recording systems at both antennas were released within an accuracy of about ten nanoseconds taking into account that the sampling period is around 90 ns. After carrying out the observations, the data from two antennas had to be brought to a common place and correlated. For this purpose, a C-program had to be developed to read the raw voltages from the two antennas and generate a 4096-point cross-power spectrum (visibility) with variable integration period. Once the bulk of the computation was completed, the visibility data had to be further analyzed using Matlab programs.

3.4 Specifications of the Direct Voltage Recording System

The following are the specifications of the 50 MHz direct voltage recording system (at each antenna base):

1. Frequency range for astronomical observations: 40 to 80 MHz.
2. Bandwidth to be processed: ~5.5 MHz.
3. Number of bits of precision required to represent the analog signal: 8 bits.
4. Sampling rate: ≥ 11 MHz.
5. Synchronization accuracy at two stations: better than 10 ns.
6. Sustained rate of the data acquisition system: ≥ 22 MBps
7. Hard disk capacity: ≥ 250 GB.
8. Duration of observation: 5 hours continuous.
9. Number of points in the cross-power spectrum: 4096.
10. Cross-power spectrum integration time: 3 ms to 1 s.
11. At each antenna bases, the 11 MHz sampling clock to the ADC has to be derived from an analog continuous wave (CW) signal from a signal generator whose phase is controlled by a Rubidium oscillator (Rubidium frequency standard).

3.5 Description of the Direct Voltage Recording System

This section contains a detailed description of the 50 MHz receiver system, with emphasis on the direct voltage recording system. The main modules of the direct voltage recording system are: the clock generation and synchronization circuit, the analog-to-digital converter, and the data acquisition system. Figure 3-3 shows a block diagram of the direct voltage recording system. The blocks shown in yellow color were developed by RRI as part of the 50 MHz receiver system for GMRT, while the blocks depicted in blue color are from the existing GMRT receiver chain which was described in section 3.2.1 of this chapter. The low-frequency V-dipole feed coexists with the 325 MHz feed on one of the four faces of the turret housing the feeds. The 50 MHz front-end receiver, which contains a low-noise amplifier with a noise-figure of ~2.7 dB, provides a total gain of about 40 dB for each polarization. It also contains a notch filter to heavily attenuate signals in the 90 to 110 MHz band corresponding to FM radio transmission. The final output of the front-end receiver is a signal of bandwidth equal to 50 MHz, and centered around 55 MHz. In the "Common Box" RF signal from the 50 MHz front-end receiver is selected.

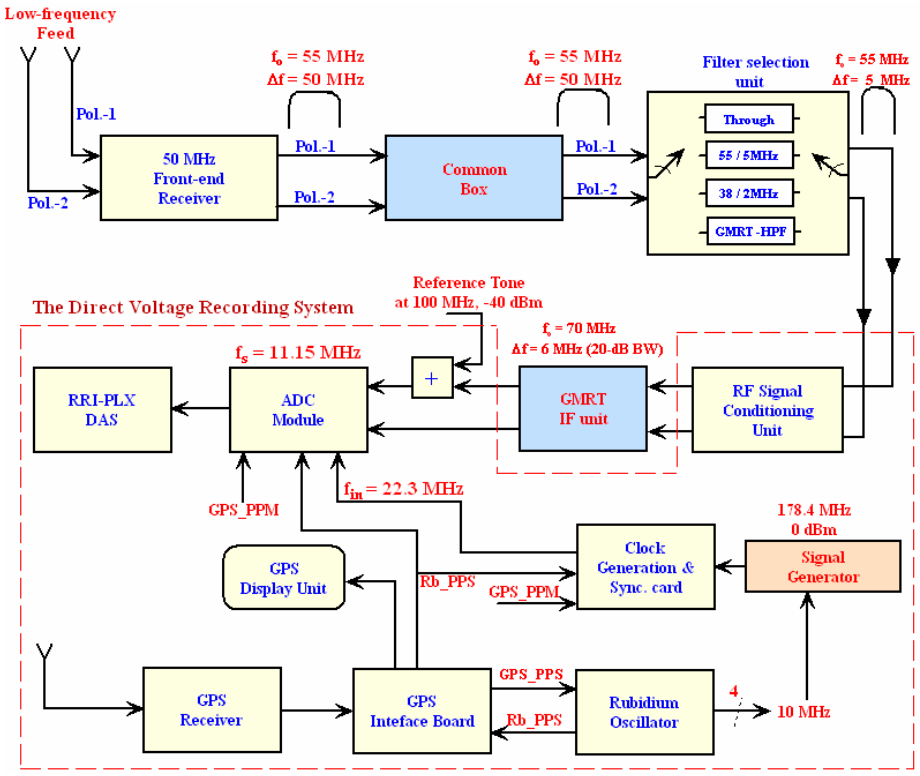

Figure 3-3: Block diagram of the direct recording system.

In the filter selection unit, the user can select one of four different paths to process:

1. A signal of bandwidth equal to 2 MHz, and centered around 38 MHz.
2. A signal of bandwidth equal to 5 MHz, and centered around 55 MHz.
3. The entire bandwidth provided by the front-end receiver, i.e., 50 MHz centered around 55 MHz (through path).
4. The normal GMRT signals.

The RF signal conditioning unit contains a combination of amplifiers and filters to further condition the analog signal before it is fed to the GMRT IF unit in which the band centered around 55 MHz is up-converted to an IF signal of bandwidth ~6 MHz, centered around 70 MHz. The IF centered around 70 MHz is fed to an 8-bit ADC for digitization. A 100 MHz reference tone, which is a phase coherent signal available at all GMRT antennas, is combined with the analog signal corresponding to V-polarization and digitized. On cross-correlating the V-polarization data from the two antennas, the value of the correlation coefficient for the reference tone should very close to unity. This is indicative of the basic

functionality of recording systems at two antennas. The next few sections describe the major building blocks of the direct voltage recording system.

3.5.1 Clock Generation and Synchronization Circuit

In a typical connected interferometer, phase synchronized local oscillators are available at every antenna base for the purpose of down converting an RF signal to an intermediate frequency (IF). As mentioned in section 3.1 of this chapter, the GMRT receiver chain has two IF units in the antenna base receiver (ABR) unit. So, we originally planned to generate the sampling clock to the analog-to-digital converter unit of the direct voltage recording system from a spare local oscillator associated with the GMRT first-stage IF unit. Later, when the GMRT first-stage IF unit also became a part of the direct voltage recording system, we decided to use a signal generator instead. The 11.15 MHz sampling clock to the ADC is derived from a clock generation and synchronization (CGS) card which contains a sine-to-square converter, and a clock divider circuit. The sine-to-square converter converts a sinusoidal signal at 178.4 MHz (obtained from a signal generator) to a square wave which is then fed to a clock divider for frequency division. The clock divider circuit consists of a high-speed, divide-by-two prescaler followed by a 4-bit counter. The 22.3 MHz output from the 3rd bit (of the 5-bit counter) is fed to a Complex Programmable Logic Device (CPLD) in the ADC module, from which, the 11.15 MHz sampling clock is derived. The signal generator at each antenna base is locked to the 10 MHz reference signal available from a

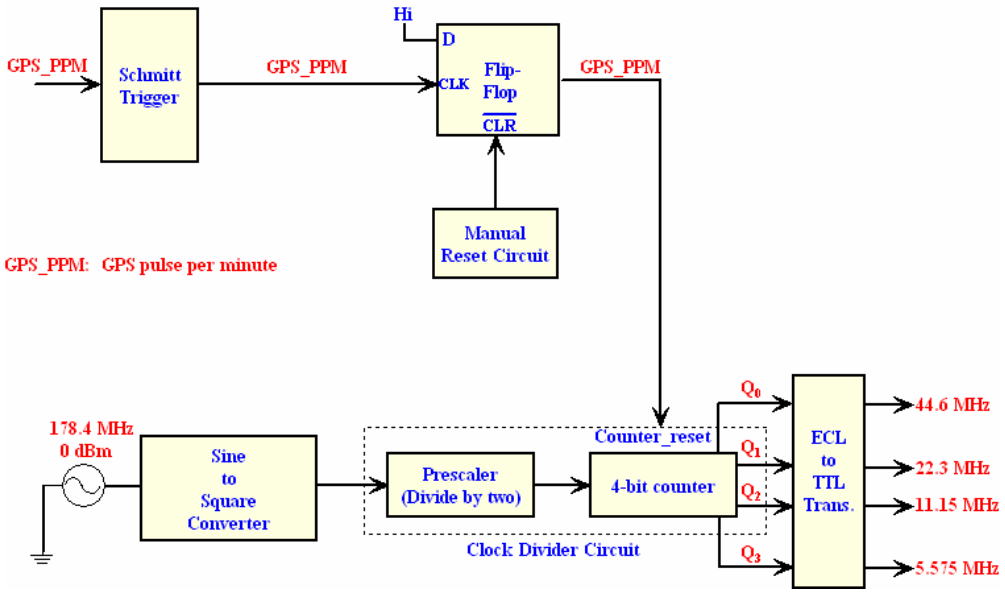

Figure 3-4: Block diagram of the clock generation and synchronization circuit.

Rubidium oscillator. The sampling clocks to the ADC present at the two antenna bases are released synchronously on the rising edge of the GPS (Global Positioning System) receiver's pulse per minute (PPM) called GPS_PPS. Figure 3-4 shows the block diagram of the clock generation and synchronization circuit.

Considering that the sampling period of the clock to the ADC is around 90 ns, one of the major requirements was to synchronously release the recording systems at the two antenna bases with an accuracy of about 10 ns. That is, the difference between the rising edges of the sampling clocks at the two antenna bases can not be greater than 10 ns. However, the difference in the arrival time or the rising edge of the pulse-per-second (PPS) edges from two independent GPS receivers, i.e., the GPS_PPS, can vary by as much as ±50ns. So, instead of directly using the GPS_PPS signal for synchronization, it was used to discipline a Rubidium oscillator at each antenna base. The Rubidium oscillator used is PRS10 from Stanford Research System Inc. When an external 1 PPS signal (the GPS_PPS in this case) is applied to PRS10, it will verify the integrity of that input and will then align its 1 PPS output with the external input. The output pulse per second from the Rubidium oscillator is called as Rubidium pulse-per-second (Rb_PPS). The processor inside PRS10 will continue to track the 1 Rb_PPS output to the 1 GPS_PPS input by controlling the frequency of the rubidium transition. The Rb_PPS signal available at each antenna base is used to synchronize the two recording systems as the difference in their arrival time is of the order of a few ns, after the Rubidium oscillators are allowed to stabilize completely. The GPS_PPM is derived by counting 59 GPS one second pulses inside a CPLD in the GPS interface board and then waiting for the rising edge of the next Rubidium pulse per second. As soon as the rising edge of the Rb_PPS is detected, a bit is toggled to denote the completion of a minute. The GPS unit used in the direct voltage recording system is based on iTRAX02 GPS receiver manufactured by Fastrax.

3.5.2 The Analog-to-Digital Converter Unit

Prior to the development of the direct voltage recording system, a survey was carried out at the GMRT site to understand the RFI environment in the frequency range 30 MHz to 85 MHz. From the survey, it was understood that an 8-bit ADC would be sufficient to meet the dynamic range requirements for carrying out low-frequency observations at around 50 MHz. Considering this, a commercial analog-to-digital converter module built around

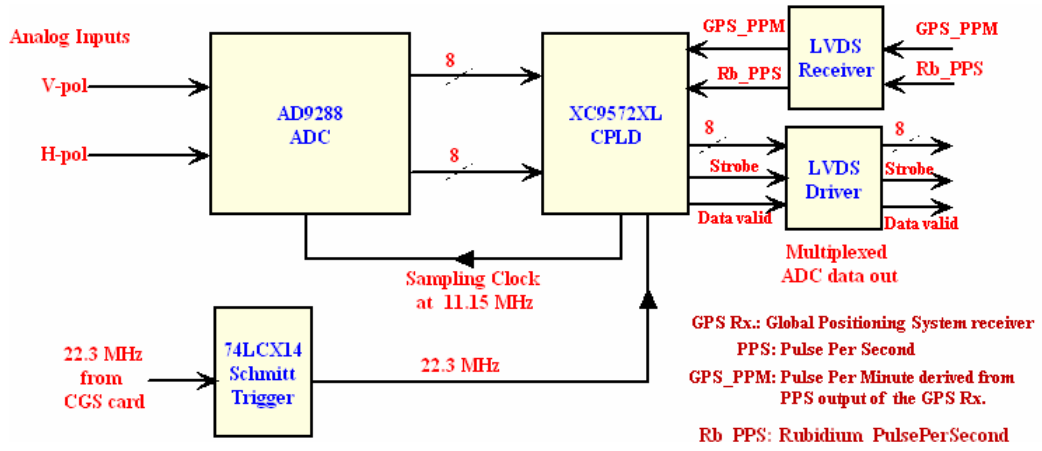

Figure 3-5: Block schematic of the ADC module.

AD9288, which is an 8-bit dual channel ADC from Analog Devices Inc., was procured for the direct voltage recording system. To digitize the 70 MHz IF signal, the 11.15 MHz sampling clock to each channel of the ADC is obtained by dividing the 22.3 MHz signal coming from the CGS board by a factor of two.

The salient features of the ADC are listed below:

1. Dual 8-bit, 100 MSPS ADC.
2. Low Power: 90 mW at 100 MSPS per Channel.
3. 475 MHz Analog Bandwidth Each Channel.
4. SNR = 47 dB @ 41 MHz.
5. 1 V p-p Analog Input Range Each Channel.
6. Single 3.0 V Supply Operation (2.7 V to 3.6 V).
7. Two's Complement or Offset Binary Output Mode

In addition to the ADC, the module also contains a Complex Programmable Logic Device (CPLD) XC9572XL from Xilinx. A firmware specific to the direct voltage recording system has been developed in VHDL to implement a marker scheme in the ADC data which can be used to detect any missing blocks of data in acquired file (refer to section 3.5.3 for more details on implementation of the marking scheme), and also multiplex the ADC data from two channels on to a single bus which is only 8 bits wide. If the ADC module is manually reset, the sampling clock to the ADC is released only on the next rising edge of the GPS_PPM pulse coming from the CGS card. Figure 3-5 shows a block schematic of the ADC module.

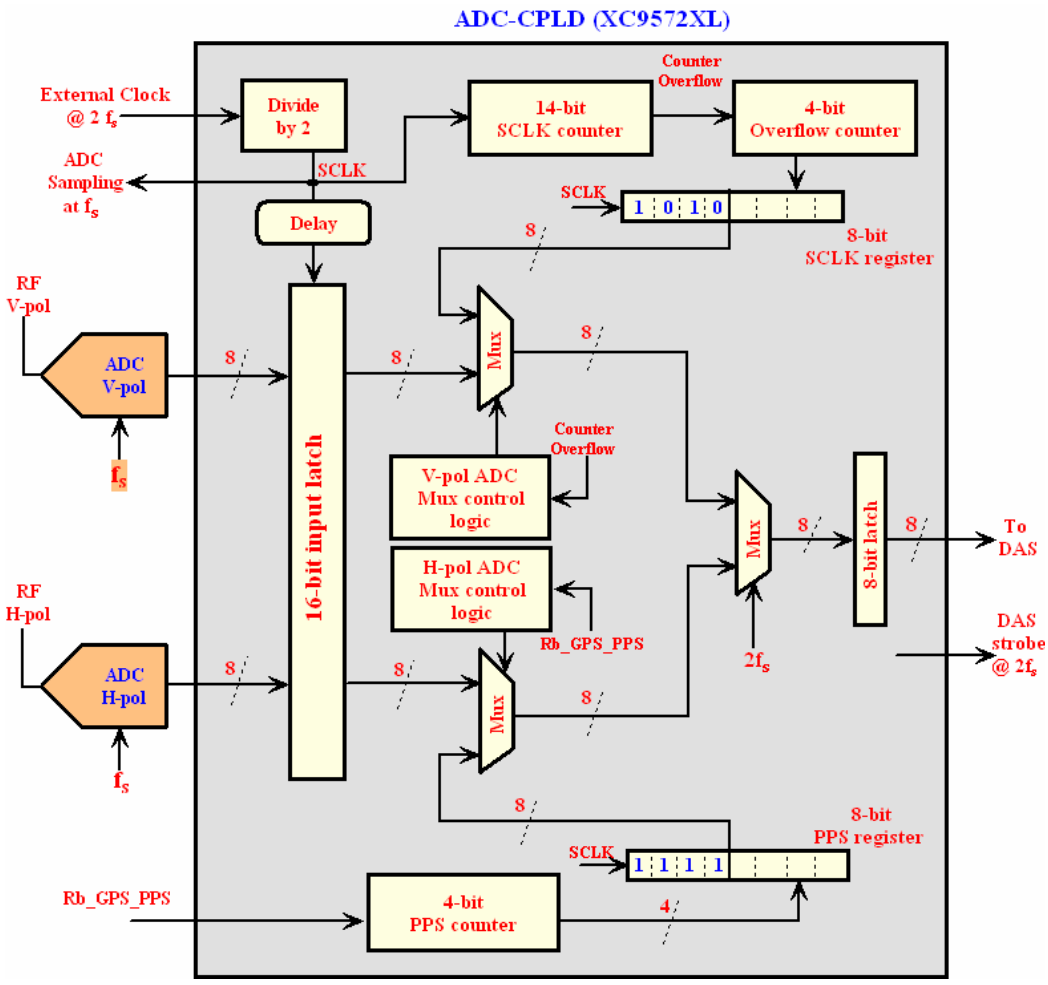

Figure 3-6: A block diagram of the firmware for marker implementation.

3.5.3 A Marker Scheme to Detect Missing Blocks of Data

The firmware inside the CPLD of the ADC module contains a marker scheme which has been implemented specifically for the direct voltage recording system to identify any missing blocks of data in the acquired data file. It counts the number of occurrences of the Rb_PPS ticks in a modulo-16 counter (4-bit PPS counter) and the number of rising-edges of the sampling clock for the entire duration of observation in a 14-bit counter (SCLK counter). Figure 3-6 shows the block diagram of the firmware developed in VHDL for marker implementation.

A 4-bit counter (PPS counter) counts the number of occurrences of Rb_PPS signal and the counter value is updated in an 8-bit register (PPS-register), who's four MSBs are frozen to "1111". Every time there is a rising edge on the Rb_PPS signal, the contents of the

8-bit PPS-register are inserted in to the ADC output data stream, in place of the H-polarization data. So, the value of the marker which is inserted on the rising edge of every Rb_PPS can range from "11110000" to "11111111," which is 240 to 245 in unsigned decimal and -16 to -1 in signed decimal. As the sampling rate is 11.15 MHz per polarization, the number of ADC data samples between two Rb_PPS markers is $11.15*10^6$ samples. In order to ensure that the inserted marker value is not confused as ADC data, on every occurrence of Rb_PPS rising edge, the H-polarization ADC data is not blocked for just one sampling clock, instead, the contents of the PPS-register are sent out to the acquisition stream for four consecutive sampling clocks.

A 14-bit SCLK counter counts the number of occurrences of the rising edge of the 11.15 MHz ADC sampling clock (sampling period = $1/11.15*10^6 = 89.686ns$). This counter overflows after counting $2^{14} = 16384$ rising edges of the sampling clock. The occurrence of each overflow pulse is counted in another 4-bit counter which is called the "overflow counter." Every time an overflow occurs, the "overflow counter" ticks and its value is updated in an 8-bit register (SCLK-register), whose four MSBs are frozen to "1010". The contents of the SCLK-register are inserted in to the ADC output data stream, in place of the V-polarization data. So, the value of the marker which is inserted can range from "10100000" to "10101111," which is 160 to175 in unsigned decimal and -96 to -81 in signed decimal. Since the 14-bit SCLK counter counts 16384 instances of rising edges of the sampling clock, the number of ADC data samples between two overflow pulses is 16384. On every occurrence of the overflow pulse, the V-polarization ADC data is not blocked for just one sampling clock, instead, the contents of the SCLK-register are sent out to the acquisition stream for four consecutive sampling clocks. Since the SCLK marker occurs every $16384*89.686ns = 1.4694ms$, there should be 680 SCLK markers between two Rb_PPS markers. From these two markers values, we can identify missing blocks of data in the acquired file, if any. Once the missing blocks of data in an output file of one antenna are identified, the corresponding blocks of data in the output file of the other antenna have to be skipped in order to continue the cross-correlating only time-aligned data sets from the two antennas

3.5.4 The Data Acquisition System

The digital representation of the ~5.5 MHz band centered around 70 MHz streaming out of the ADC at 22.3 MBps (two polarizations) is acquired on to a computer using a PCI-based data acquisition system (DAS) developed at the Raman Research Institute. The maximum sustained data rate of the DAS is about 25 MBps. The acquisition card is built around PLX-9054, a PCI chipset, which provides it with an interface to the PCI bus. Figure 3-7 shows the block diagram of the RRI-PLX card.

The RRI-PLX card has functionality for real-time data processing with two FPGAs (up to 300k gates of Spartan2e family), two CPLDs- one for configuring the FPGAs and the other for data routing, up to 256 kilobytes of SRAM, a programmable clock synthesizer (0.391 to 100 MHz), and receivers and drivers for RS-422 and serial/parallel Low Voltage Differential Signaling (LVDS) standards. The FPGAs can be programmed either though JTAG port or from a PC when the card is inserted in a PCI expansion slot. The 8-bit ADC data and the data strobe which are in the LVDS format are connected to the parallel LVDS receiver section of the RRI-PLX card for acquisition in to the computer.

The acquired data is then transferred to a set of two hard disks (each of capacity-250 GBytes) in RAID-0 configuration. The acronym “RAID”, which stands for Redundant Array of Independent (or Inexpensive) Disks, is a technology that employs the simultaneous use of two or more hard disk drives to achieve greater levels of performance, reliability, and/or

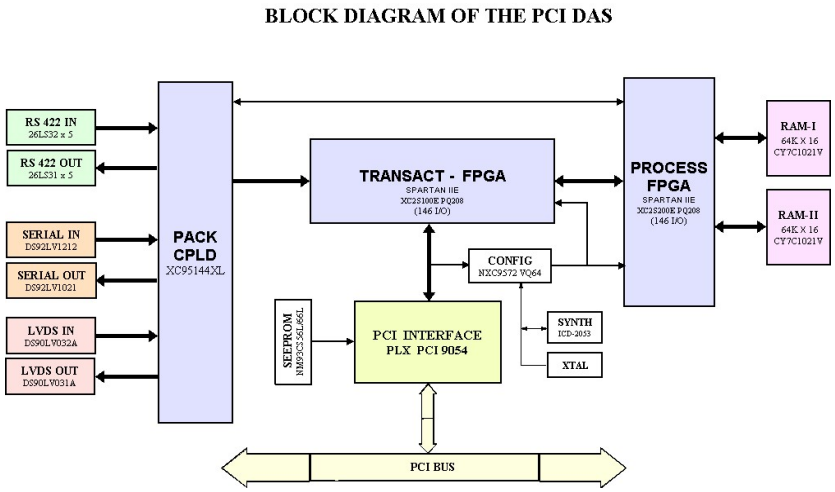

3-7: A block diagram of the RRI-PLX DAS card.

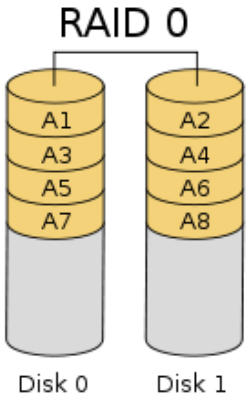

Figure 3-8: RAID-0 configuration.

larger data volume sizes. There are various combinations of these approaches giving different trade-offs of protection against data loss, capacity, and speed. RAID-0 -also called striping- is a method of storing data on multiple hard disks by interleaving the data and spreading it across the devices usually achieving faster read and write speeds. However, it is important to note that RAID-0 actually provides no data redundancy as data on all disks will be lost if any one disk fails. The read and write performance will increase, because reads and writes are done in parallel on the devices. This is usually the main reason for running RAID-0. As shown in Figure 3-8, an idealized implementation of RAID 0 would split I/O operations into equal-sized blocks and spread them evenly across two disks. A RAID-0 can be created with disks of differing sizes, but the storage space added to the array by each disk is limited to the size of the smallest disk. As the direct voltage recording system contains two hard disks of capacity 250 GB in RAID-0 configuration, the total storage space available is 2*250 GB = 500 GB. At a data rate of 22.3 Mbytes per second from the ADC, 5 hours of observation corresponds to a data size of $22.3 MBps * 60 s * 60 \min * 5 hrs = 400 GB$. Since the total storage capacity of the direct voltage recording system is 500 GB, data recording can comfortably be carried out for a period of five hours.

An existing C-program for data acquisition from the RRI-PLX card was such that it would produce one huge file- could be of the order of 10 Gigabytes for 10 minutes of observation with the direct voltage recording system- at the end of an observation session. From the point of view of pre-processing the acquired data, wherein, we are looking for missing blocks of data or corrupt data, instead of writing out a single file of a huge file size, it would be better if multiple files are written out during the course of observation. The file

size of individual files written out can be chosen in such a way that it is neither too small-in which case there is an unnecessary overhead due to the increased number of file openings and file closings- nor too big wherein it becomes difficult for the reasons cited above. So, the acquisition program was tweaked to produce multiple files, each of file size equal to 1 GB, which corresponds to ~1 minute of observation.

3.6 Laboratory Tests Results

The various modules of the direct voltage recording system which were described in detail in the previous section were integrated and configured to be tested in interferometric mode in the laboratory at the Raman Research Institute. Each recording unit had its own power supply units, ADC module, signal generator for generating the sampling clock, GPS receiver along with Rubidium oscillator, CGS card, RF signal conditioning unit, and data acquisition system in an attempt to simulate the actual field conditions during the testing process. Figure 3-9 shows a photograph of the integrated recording systems set up in the laboratory at RRI for testing it in interferometric mode.

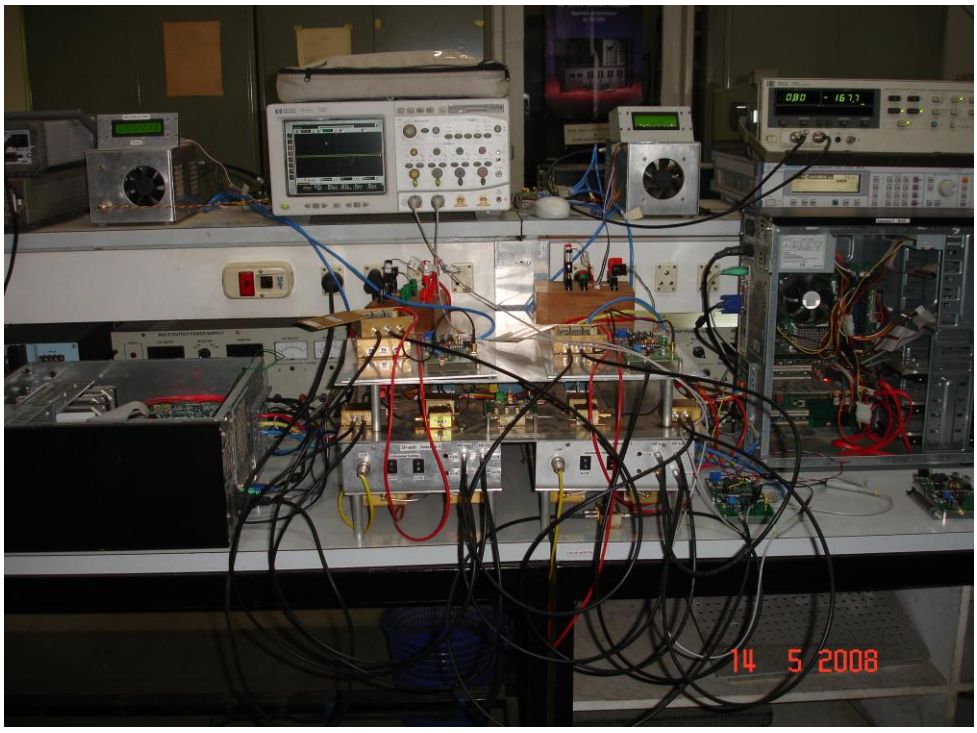

Figure 3-9: Photograph of the test set up showing the two direct voltage recording systems.

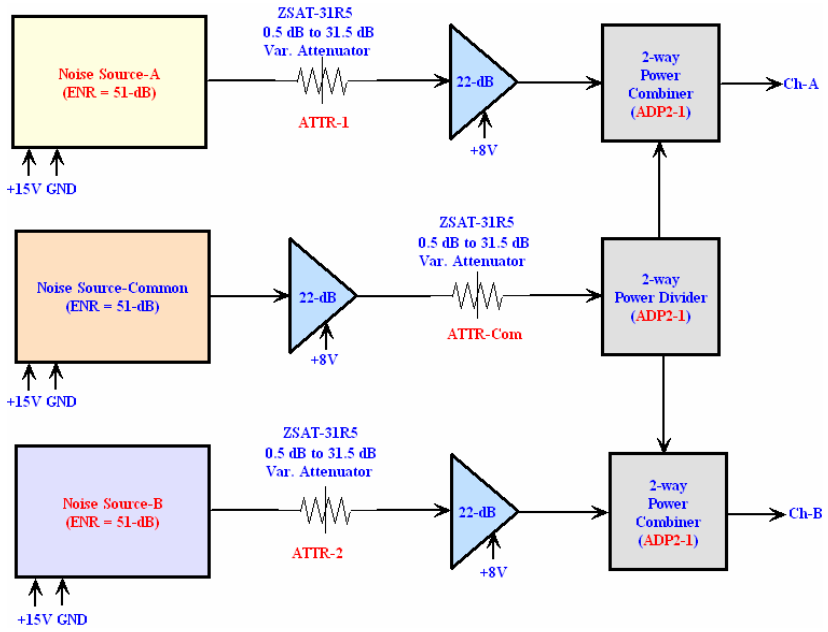

Figure 3-10: Correlated/Uncorrelated noise source.

A noise source with the provision to control the amount of correlated and uncorrelated noise was developed specifically to test the two recording systems. Figure 3-10 shows a block diagram of the correlated/uncorrelated noise source. By adjusting the value of the attenuators: ATTR-1, ATTR-2, and ATTR-Com, the correlated noise component at the outputs Ch-A and Ch-B can be controlled. For example, by setting ATTR-1 and ATTR-2 to their maximum value and reducing the value of ATTR-Com attenuator, a highly correlated noise output can be obtained at Ch-A and Ch-B. Similarly, by heavily attenuating only the noise coming from the common noise source, the noise obtained at Ch-A and Ch-B can be uncorrelated. The Ch-A output is fed to a two-way power divider whose outputs are fed to the two channels of the RF signal conditioning unit. The signal conditioned analog signals of bandwidth ~5.5 MHz and centered around 55 MHz are fed to the two channels of the ADC module. The ADC gives an 8-bit representation of the analog signal at a sampling rate of ~11 MSps. A similar arrangement exists for the second recording system as well. The steps that are followed in a typical acquisition procedure are:

1. All the modules of the two recording systems are powered on, RF output of the two signal generators connected to the CGS card are enabled, the acquisition computers are kept ready for acquisition. Since the ADC-CPLD blocks the DAS-strobe output from the ADC, there is no data for the RRI-PLX card to acquire.

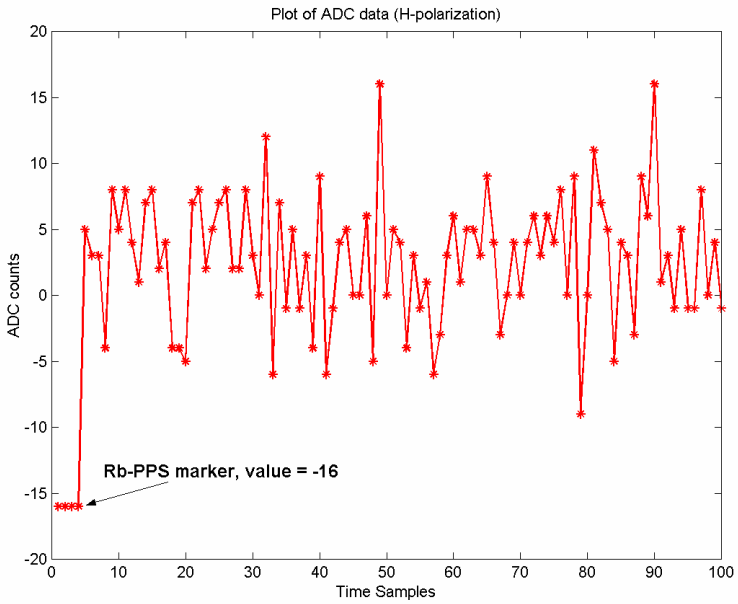

Figure 3-11: ADC data containing four Rb_PPS markers.

2. The ADC modules are reset by pressing the manual reset button in the respective ADC module which causes the action inside ADC-CPLD to be frozen till the occurrence of the rising edge of the next GPS_PPM.
3. On the occurrence of the next GPS_PPM - the difference in the time of arrival of the rising edges at the two ADC modules is always within ± 5 ns of each other- the firmware inside the ADC-CPLD releases the sampling clock to the ADC. A C-program communicating to the GPS receiver -thorough the serial- port of the acquisition computers of the two recording systems- logs the GPS time at the beginning of an acquisition cycle. This mechanism logs the absolute time of an observation session which would be required during data analysis.
4. The data obtained by data acquisition systems (at 22 MBps) is processed to obtain a ~1s averaged self-power spectra, cross-power spectra, and a plot of correlation coefficient as function of frequency, by averaging 1024, 8192-point Fourier transform. Each recording system can record data from two polarizations of an antenna: V-pol and H-pol resulting in an overall data rate of (11MBps for a polarization * 2 =22MBps). The section 4.2 of Chapter 4 contains a detailed description of the methodology for 50 MHz data analysis

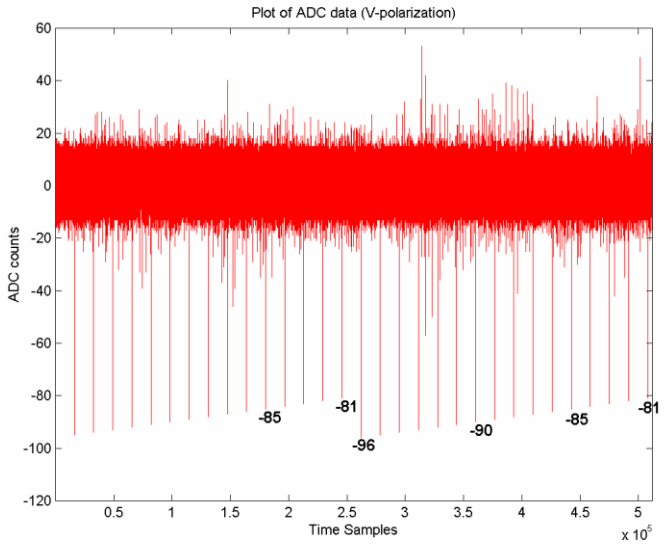

Figure 3-12: ADC data containing SCLK overflow markers.

Figure 3-11 shows the plot of raw ADC data (H-polarization) of one of the recording systems in which the first four data points at the beginning corresponds to Rb_PPS marker whose values is equal to -16 (11110000). Figure 3-12 shows the plot of raw ADC data (V-polarization) of one of the recording systems in which the SCLK overflow marker whose values ranging from -96 (10100000) to -81 (10101111), occurring every 16384 samples are clearly seen. Figure 3-13 shows the self-power spectrum obtained from two polarizations of both the data recording systems. The information contained in the self-power spectrum will be used in the computation of correlation coefficient.

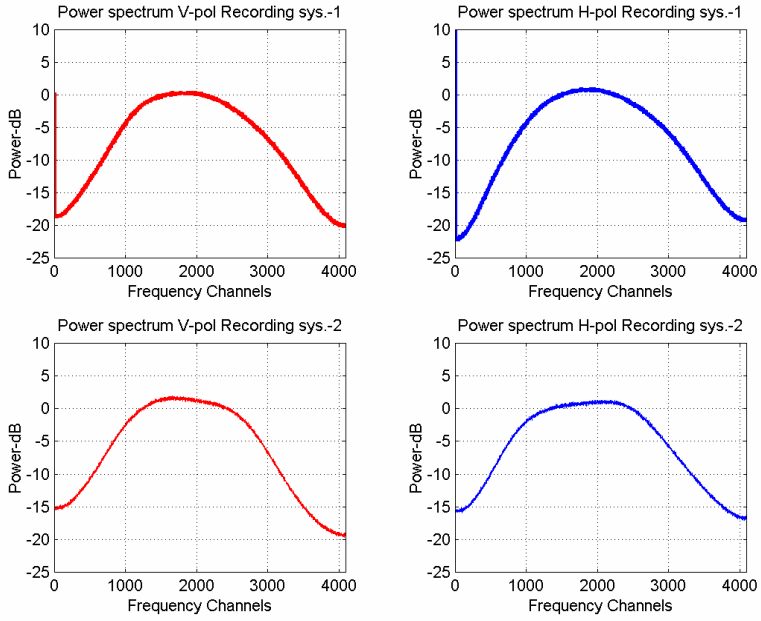

Figure 3-13: Self-power spectrum from the two voltage recording systems.

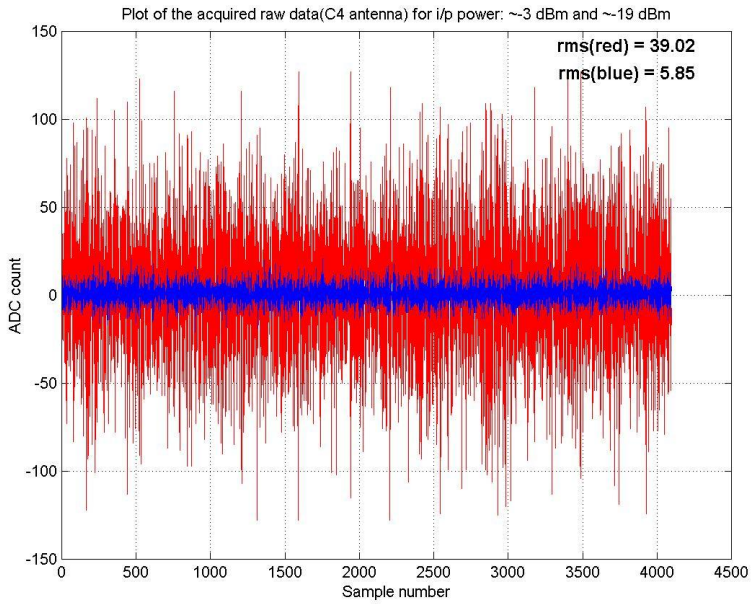

Figure 3-14: A plot of raw ADC data from linearity test.

In order to measure the linearity of the recording system, the total power input to the ADCs of both recording systems is varied by adjusting the attenuators in the noise source. It may be recalled that the maximum permissible input voltage to the ADC is $1V_{p\text{-}p}$ which corresponds to +4 dBm power of a sinusoidal signal. The ADC output codes can range from +127 to -128. However, we have restricted the total noise power input to the ADC -3 dBm because, at -3 dBm, the measured RMS is about 40 (from the red colored plot on the left-

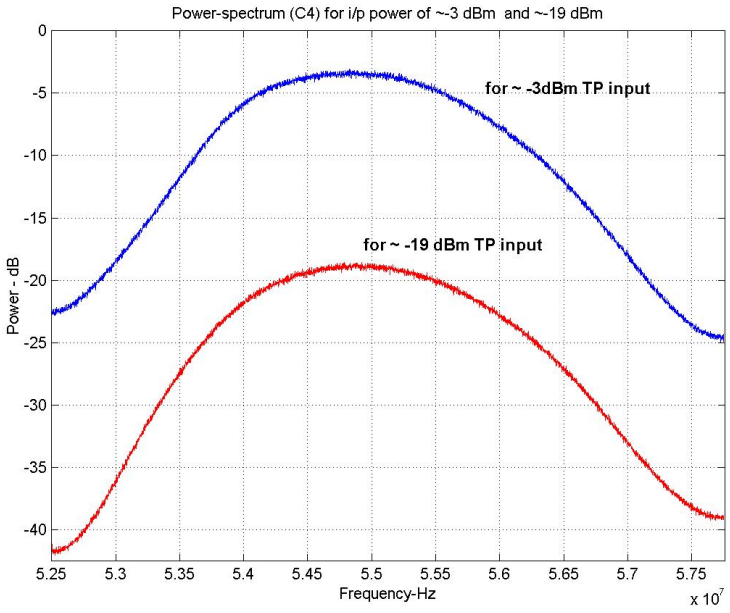

Figure 3-15: Linearity plot of the direct voltage recording system.

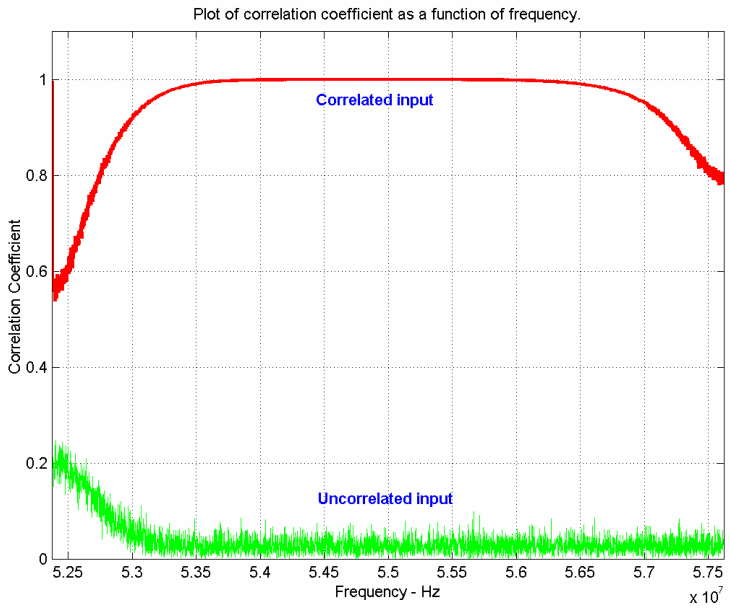

Figure 3-16: A plot of correlation coefficient obtained for correlated and uncorrelated noise inputs.

hand side). Already, at this total power itself, one sample in about thousand samples can exceed 3*40 which is 120. The plot in Figure 3-14 shows the time-domain data acquired by the recording system in which the measured RMS value in terms of ADC counts ranges from 5.85 to 39.02, which is a factor of ~6.6 (16.3 dB), corresponding to the total power input to the ADC ranging from -19 dBm to -3 dBm (16 dB). Figure 3-15 as expected, shows the difference in power levels to be about 16 dB. It must be emphasized that the linearity test has indeed tested the linearity of the entire chain of analog modules and the ADC module of the direct voltage recording system, up to a total power of -3 dBm. Tests conducted on the second recording system also showed similar results.

As mentioned earlier, the correlated/uncorrelated noise source was required to control the amount of correlated noise fed to the two recording system. Figure 3-16 shows a plot of correlation coefficient as a function of frequency for two input conditions. In the first case (red-colored plot in Figure 3-16), the attenuators in the noise source are so adjusted that noise from the common noise source is the more dominant of the three noise sources. As expected, the correlation coefficient is very close to one (0.996) because a highly correlated noise input is fed to the two recording systems. In the second case (green colored plot in Figure 3-16), the correlation coefficient measured is ~0.03. It is so because noise output from two independent noise sources: noise source-A, and noise source-B are dominant with the noise output from the common noise source being heavily attenuated.

Chapter 4

Chapter 4

Results from Test Observations carried out at GMRT

4.1 Integration with GMRT Receiver Chain

After thoroughly testing the two direct voltage recording systems in interferometric mode at the laboratory in RRI, they were shipped to the GMRT site for installation. Antenna E-02 in the eastern arm and C-04 in the central square were identified as the two antennas in which the direct voltage recording systems would be installed for carrying out test observations at 50 MHz. Figure 4-1 shows the block diagram of the initial set up in which a

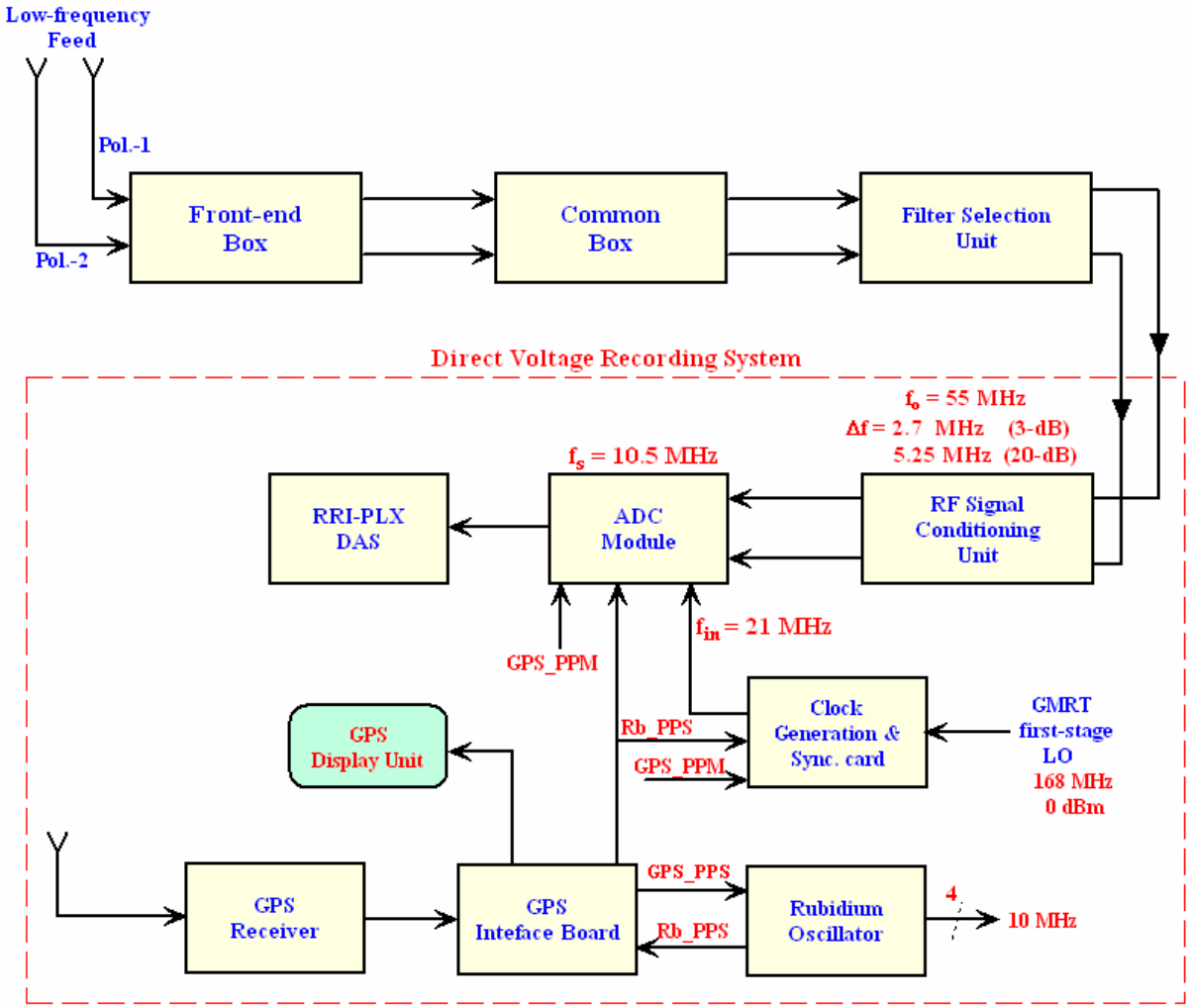

Figure 4-1: A block diagram of the initial set up of the direct voltage recording system.

signal of bandwidth equal to 5.25 MHz, centered at 55 MHz was digitized by the ADC module using a sampling clock of 10.5 MHz. In this set up, the sampling clock of 10.5 MHz was derived from the local oscillator of the GMRT first-stage IF unit which was tuned to 168 MHz (168/8=21 MHz).

However, the RF band centered at 55 MHz was not stable for reasons like out-of-band interference, power-line harmonics on the dc power supply to various modules of the direct voltage recording system. Figure 4-2 shows the power-spectrum (self-power) obtained from both polarizations of antenna C-04 and E-02. It is clear that bandshapes of both polarizations from E-02 (antenna-2) are distorted while C-04 (referred to as antenna-1) shows a neat bandshape. This problem of unstable RF band was more severe at E-02 than C-04 because, E-02 happens to be antenna in GMRT's eastern arm, away from the central square. The use of additional power-line filters on the 230 V AC to the power supply units and decoupling capacitors at every DC output vastly improved the quality of the DC power supply to the modules listed above. Additional measures were taken to improve the ground connections of the various modules of the direct recording systems. The individual modules of the recording system were connected to the ground reference is the so-called "star" ground

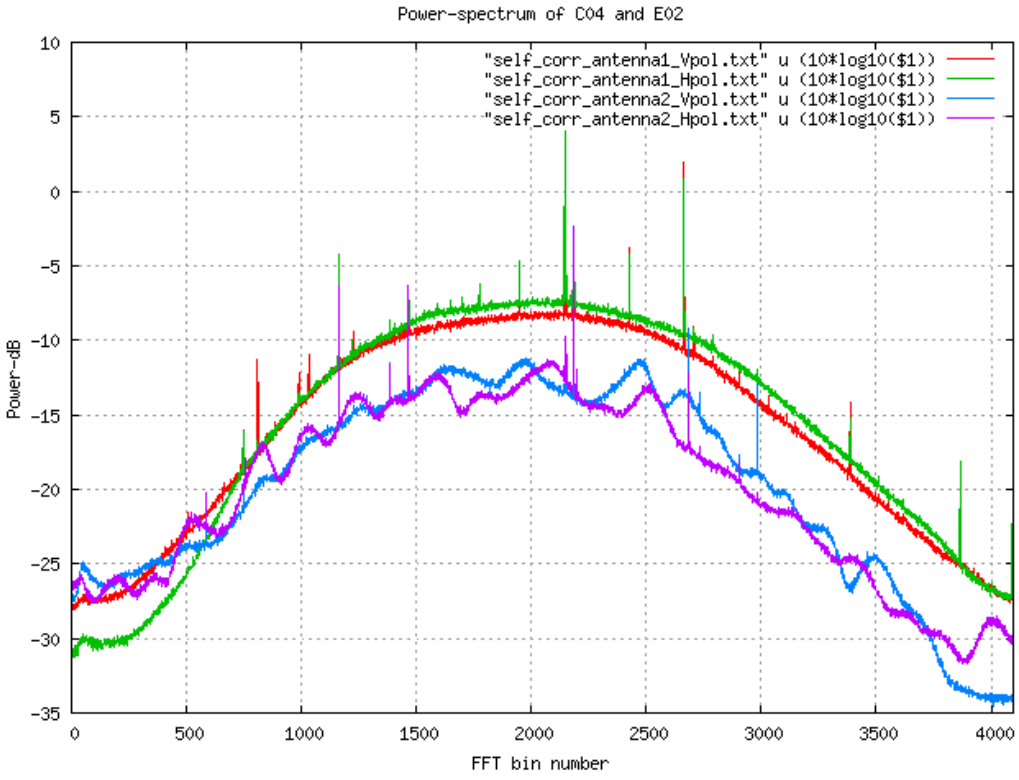

Figure 4-2: Bandshapes obtained from C-04 and E-02 using the initial set up.

connection, in which each module has a single direct connection to the reference point, forming a star-shaped distribution network. In this way, any current flowing from a single module to ground affects only that device. The reference point in this case was the ground of the shielded room inside the antenna cone. The direct voltage recording system is housed inside this shielded room.

After all these measures, a test scan was taken across Cygnus-A (a very bright source in the sky) using antennas C-04 and E-02, which are shown in Figure 4-3. While C-04 shows a neat deflection due the source, E-02, even after taking all the additional measures, continued to be severely affected by RFI and power-line harmonics. Figure 4-3 clearly shows that antenna E-02 is severely affected by RFI, and does not provide any discernable deflection when it scans across the source.

So, it was decided to shift the recording system from antenna E-02 to antenna C-11, another antenna in the central square. The fourth antenna which was equipped with the low-frequency V-dipole feed, W-02, was not available for use around the time we visited GMRT for test observations. Over and above these changes, in order to obtain better out-of-band RFI rejection, it was decided to pass the 55 MHz RF through the GMRT first-stage IF unit. The IF unit up-converts the ~5.25 MHz band centered around 55 MHz to IF of 70 MHz. The up-conversion process combined with the sharp roll-off of the 70MHz/ 6 MHz SAW filter used in the GMRT IF unit provided better out-of-band RFI rejection. This IF signal of bandwidth ~6 MHz is digitized using a sampling clock of 11.15 MHz. Figure 4-4 shows a detailed block

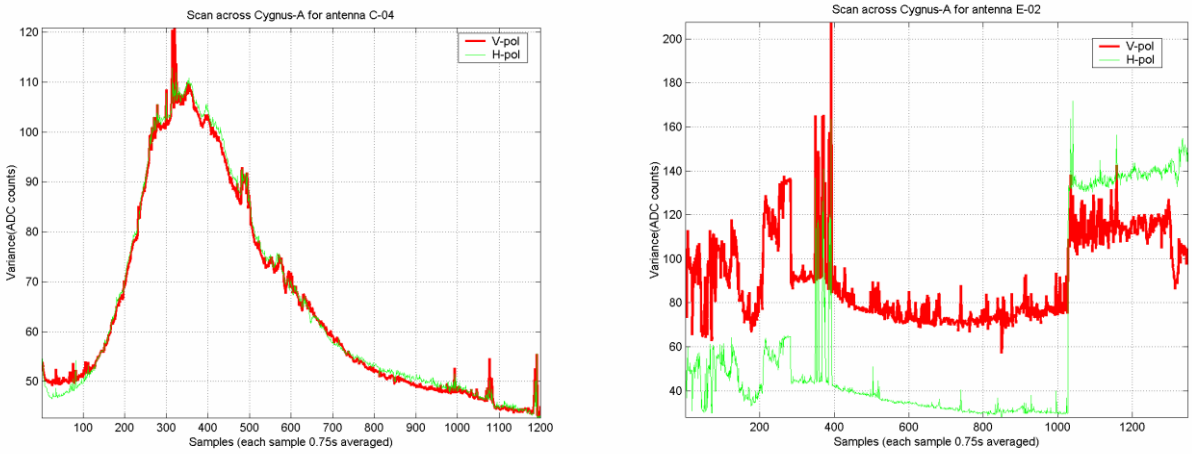

Figure 4-3: Scan across Cygnus A using C-04 and E-02.

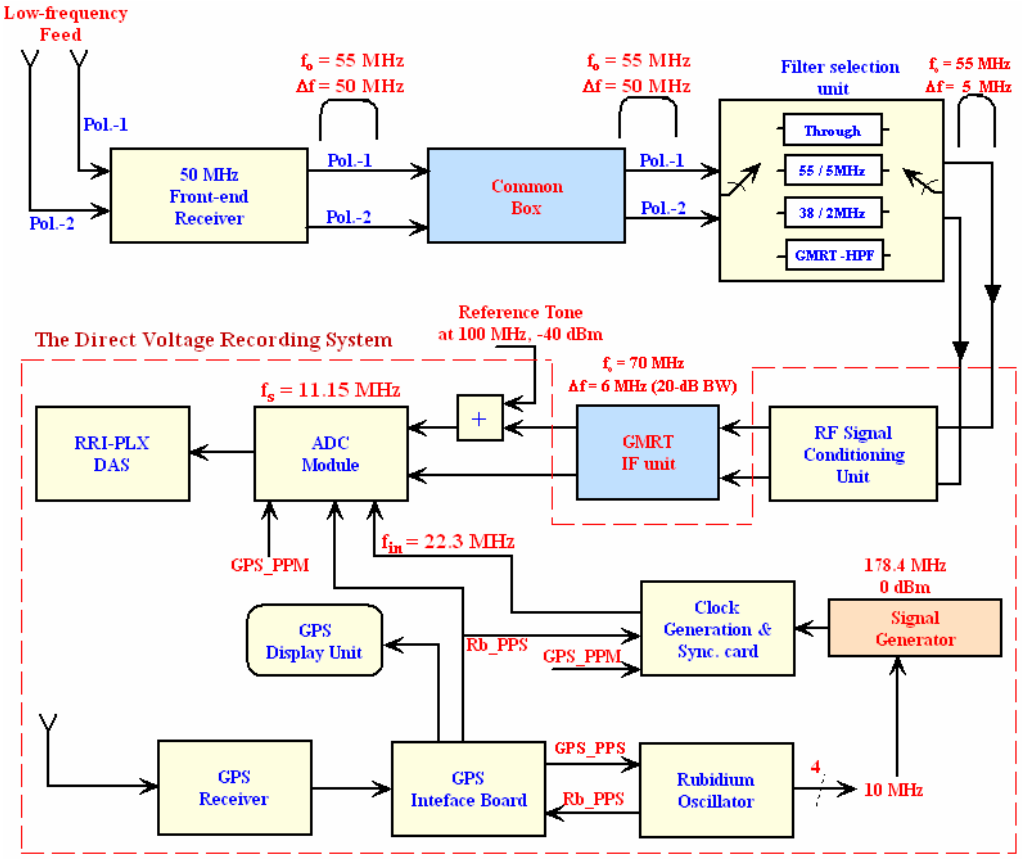

Figure 4-4: Block diagram of the direct recording system (new configuration).

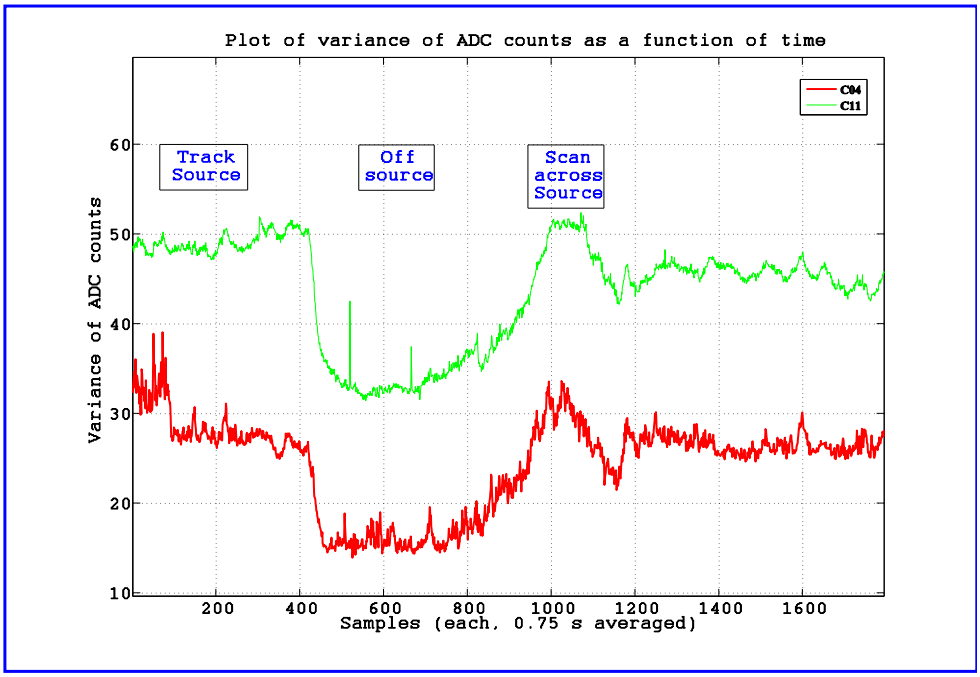

Figure 4-5: Scan across Cygnus A with the new set up.

diagram of the direct voltage recording system (new configuration). Figure 4-5 shows the

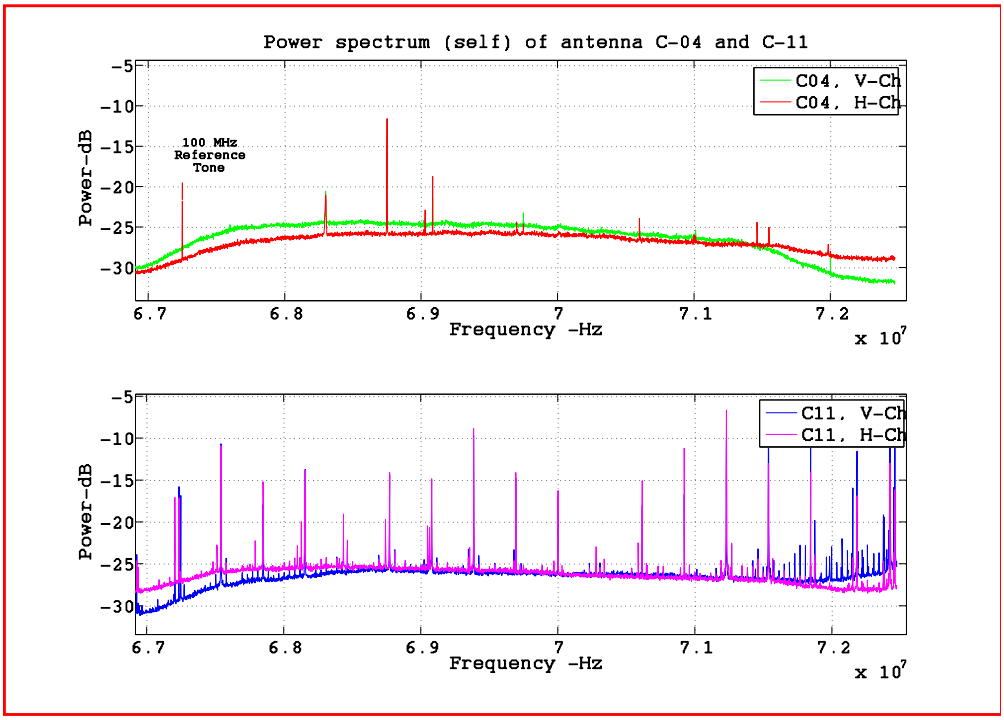

Figure 4-6: Bandshapes obtained from C-04 and C-11 with the new set up.

result of a test scan taken across the astronomical source, Cygnus-A, after including the first-stage GMRT IF system. The plot shows a clear deflection when the two antennas are on-source and off-source.

Figure 4-6 shows a plot of bandshapes (self-power spectra) obtained from C-04 and C-11. The red-colored plot clearly shows the reference tone injected in to the V-channel of C-04. Since the sampling clock to ADC is maintained at 11.15 MHz, the tone at 100 MHz folds back in to the band of interest ranging from 66.9 MHz to 72.475 MHz, and appears at 67.25 MHz. From figure 4-5, it is obvious that even though the bandshape in C-11 is smoother compared to E-02, antenna C-11 is also affected by RFI. The reference tone in the V-channel of C-11 (blue colored plot) is not seen clearly because of RFI around it. Figure 4-4 clearly illustrates the exact place where the 100 MHz reference tone is injected into the direct voltage recording system.

4.2 The 50 MHz test observations

After successfully integrating the two direct voltage recording systems developed by RRI (RRI-DS), and carrying out functionality tests to validate them, what followed was a 50

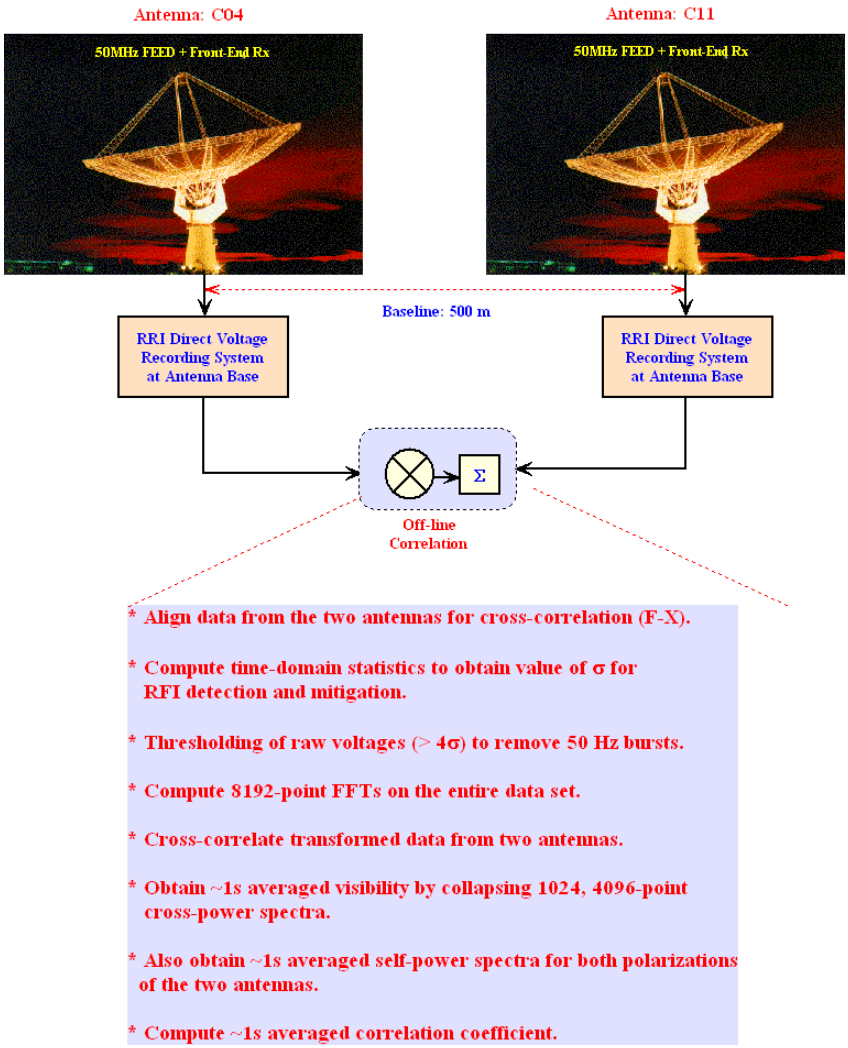

Figure 4-7: Steps involved in cross-correlating signals from the two antennas.

MHz observation campaign in which the two systems installed at C-04 and C-11 were operated in interferometric mode. As mentioned earlier, the two systems digitized a signal of 5.5 MHz bandwidth using a sampling clock of 11.15 MHz and recorded the raw voltages. They were synchronized using signals from GPS-disciplined Rubidium oscillators. The test observations were carried out on astronomical sources simultaneously using the GMRT hardware correlator (GMRT-HC), software correlator (GMRT-SC), and the RRI-DS. The Subsection 4.2.1 describes the procedure to generate visibilities from the acquired data and also illustrates the major steps involved, using relevant plots. Subsection 4.2.2 presents the RFI scenario at 50 MHz and also describes the steps involved in the preliminary RFI mitigation strategy. The Subsection 4.2.3 explains the steps involved in estimating the SNR as a function of channel bandwidth

4.2.1 Computing visibilities

For RRI-DS ~1s averaged visibilities are computed offline by averaging 1024, 8192-point FFT frame. While Figure 4-7 shows the major steps involved in obtaining the ~1s averaged visibilities, the detailed procedure that has been followed to obtain the averaged visibilities for the entire data set is described below:

1. The acquired data from the two antennas are brought to a processing computer where the processing software-a C-program running on Linux platform, developed for the 50 MHz observations-checks for data integrity by picking up all the Rb_PPS and SCLK markers in the data set. Then, from the first 1 GB files belonging to the two antennas, data is picked up in bunches of 8192 points and Fourier transformed. After each 8192-point transform, only a user-specified FFT bin is written out to a file called "FFTchannelOutput.txt". A Matlab program was developed to estimate the delay that needs to be inserted into one of the data streams, before cross-correlation. The Matlab program reads the FFT channel data corresponding to the two antennas from the file "FFTchannelOutput.txt" into two arrays and computes a cross-correlation for various positive and negative delays. The cross-correlation value has a peak value only for one particular delay and for other delays, it is nearly zero.
2. Depending on the value of the delay obtained, the main C-program skips a specified number of data points beginning from the first data point from one of the antenna files and aligns the data for cross-correlation.
3. In the aligned data sets, any data point which is above 4σ is replaced with a data randomly chosen from the acquired data stream. Similarly, the data points corresponding to Rb_PPS and SCLK markers are replaced with a randomly chosen data from the acquired data set itself. Then, statistics like mean value, variance and RMS are computed for every data set of ~1 s duration.
4. From the aligned data set, chunks of 8192 points are read out sequentially and Fourier transformed (using the FFTW package) to obtain two sets of vectors: $\mathbf{V_1}$ and $\mathbf{V_2}$. The cross-product, $\mathbf{V_1 x V_2^*}$, produces an FFT bin-wise cross-correlation of the two data sets. Since a single 8192-point FFT frame corresponds to ~0.734ms averaging, by vector accumulating 1024 such cross-correlations, a ~1s averaged visibility function is obtained. Also, after every 8192-point Fourier transform, $|\mathbf{V_1}|^2$ and $|\mathbf{V_2}|^2$ corresponding to self-

power-spectrum of each antenna, are computed. Finally, a ~1s averaged self-power-spectrum for each antenna is produced.

5. From the ~1s averaged cross-products and self-products, the measured correlation coefficient ρ_{meas} is obtained from equation (4.1):

$$\rho_{meas} = \frac{\left\langle \mathbf{V_1 x V_2^*} \right\rangle}{\sqrt{\left|\mathbf{V_1}\right|^2 \mathbf{x} \left|\mathbf{V_2}\right|^2}} \tag{4.1}$$

6. The ~1s averaged visibilities, self-powers, correlation coefficient are computed for the entire data set and written out on to a file further analysis. RRI-DS maintains an integration period of ~1s so that it is comparable to the 1s averaged visibilities generated by both GMRT hardware correlator and software correlator. However, RRI-DS has the provision to generate visibilities with integration period varying from a minimum of 0.73 ms to a maximum value which is limited only by the size of the acquired data set.

The C-program which is used to process the acquired data from the two antennas, and generate the visibilities for a particular observation date and observation number, arranges the ~1s averaged visibilities for the entire data set as per the structure shown in Figure 4-8.

The first step involved in generating the visibilities from the acquired data set is to

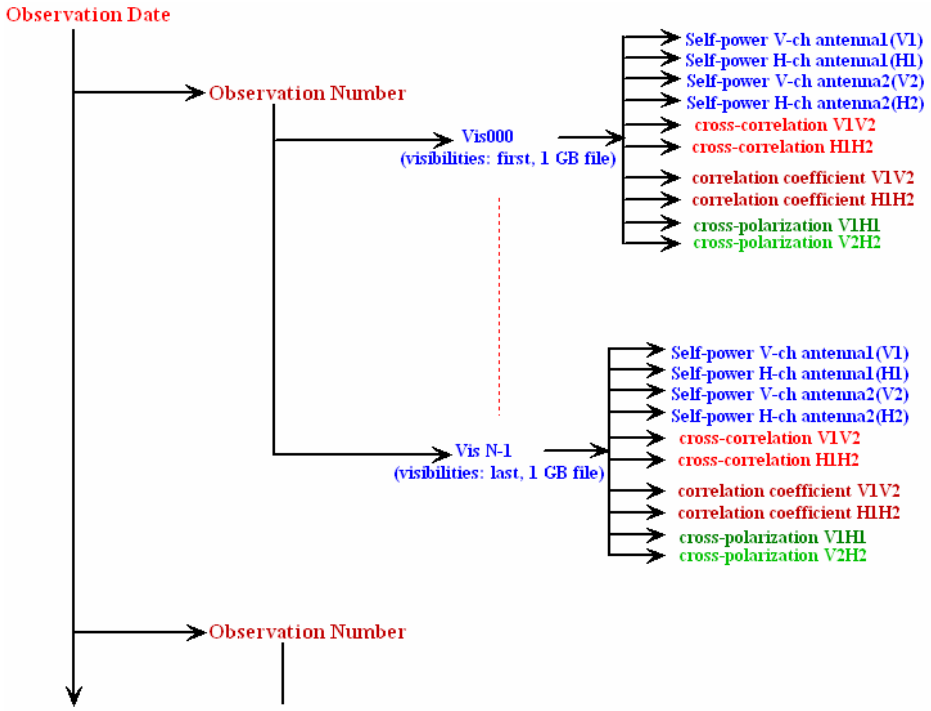

Figure 4-8: Visibility output file structure.

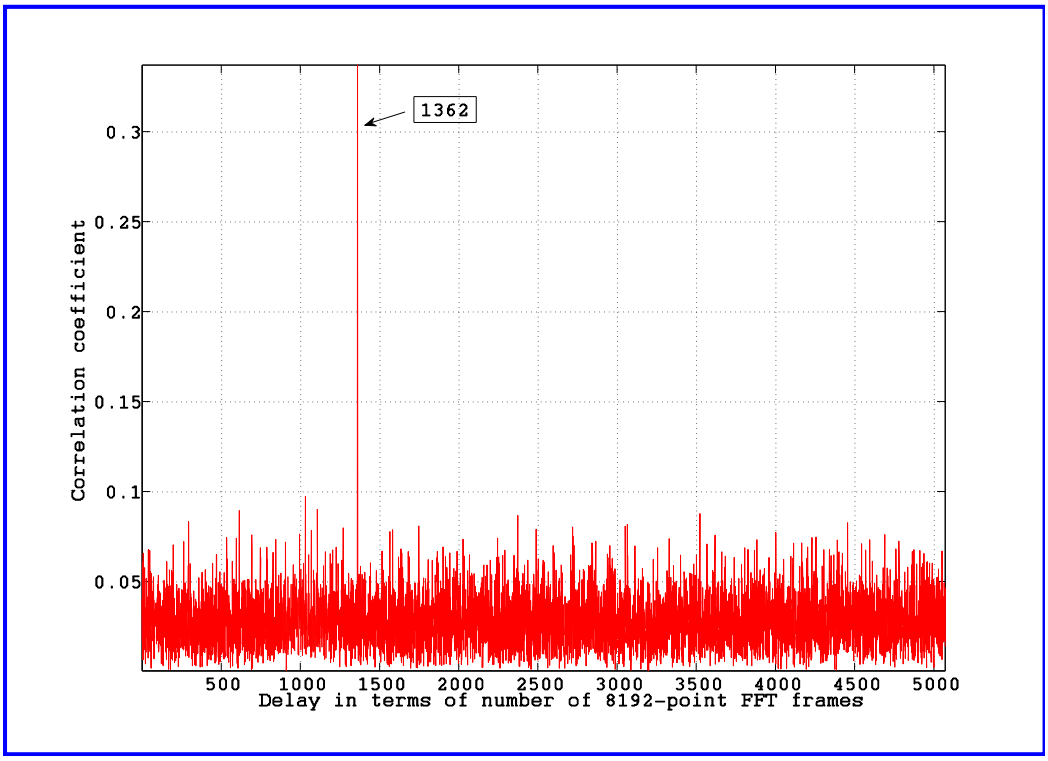

Figure 4-9: A plot of correlation coefficient of an FFT channel as a function of delay. (Corelation coefficient peaks for a delay of 1362 units).

align the data set so that cross-correlations can be computed. From the data acquired during Cygnus observation, a plot of ~1s averaged correlation coefficient of an arbitrarily chosen frequency channel, plotted as a function of delay is shown in Figure 4-9. Here, the delay is measured in terms of number of 8192-point FFT frames. From the plot it is clearly seen that the correlation-coefficient peaks (~0.35) for a delay value corresponding to 1362, whereas, it is nearly zero for other delays implying that the data sets are not aligned. In this case, a positive delay of 1362 units implies that the number of data samples that needs to be skipped from C-04 data file are 1362*8192=11157504, which corresponds to a delay of about one second considering that the sampling rate is 11.15 MHz. However, it must be emphasized that the time resolution with which delay can be estimated is 8192*89.68ns = 0.73 ms. By skipping the first 11157504 samples in the data set obtained from C-04, the data samples from C-04 and C-11 can be cross-correlated.

However, before computing the correlations on Cygnus A data, any data in the data set which is above a fixed threshold of 4σ is replaced with a randomly chosen data from the acquired data set. In order to obtain a representative value for σ to be used in computing the 4σ threshold, beginning with 1σ obtained from the raw ADC counts, σ is computed

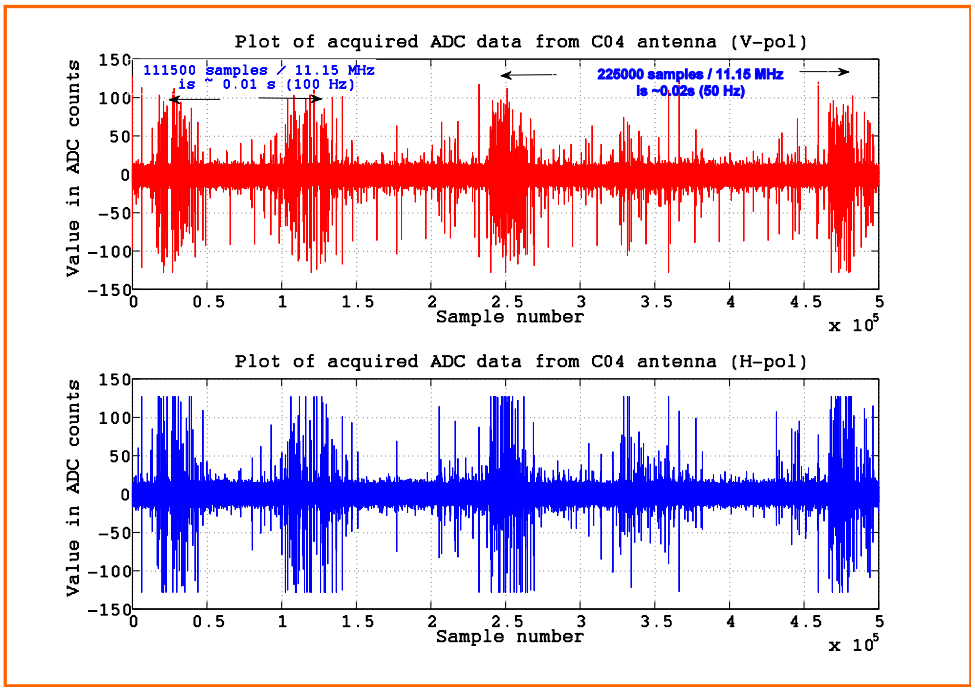

Figure 4-10: A plot of raw ADC data acquired from antenna C-04.

iteratively by removing any ADC data which is above 4σ, until 1σ does not reduce any further. Using this procedure on the Cygnus A data set, 1σ in terms of raw ADC counts is ~5.

While Figure 4-10 shows a plot of raw ADC data obtained from C-04, Figure 4-11 shows the number of samples greater than or equal to 4σ, as a function of data blocks with each block containing 524288 samples. The effect of radio noise (RFI) due to gap-discharges in the high-voltage power line is clearly seen affecting the raw ADC data at the power-line frequency of 50 Hz and its harmonics. In Figure 4-10, it is clearly seen that the bursts occur regularly at spacings of 0.01 seconds (100 Hz) and 0.02 seconds (50 Hz) in both V-pol and H-pol data set. As per the data sheet of the ADC, the peak-to-peak swing of the input voltage to the ADC should be limited to 1 V, exceeding which, the data gets clipped. Considering the problems posed by the power-line RFI, the total power input to the ADC is maintained at -20 dBm in an attempt to prevent the ADC input signal getting clipped. Since we are using an 8-bit ADC, the ADC step size (1 LSB) is given by $1/256 = 4$ mV. Since the value of 1σ for the data set under consideration is around 5 when expressed in terms of ADC counts, the number of ADC bits available to represent the astronomical signal is at least four bits.

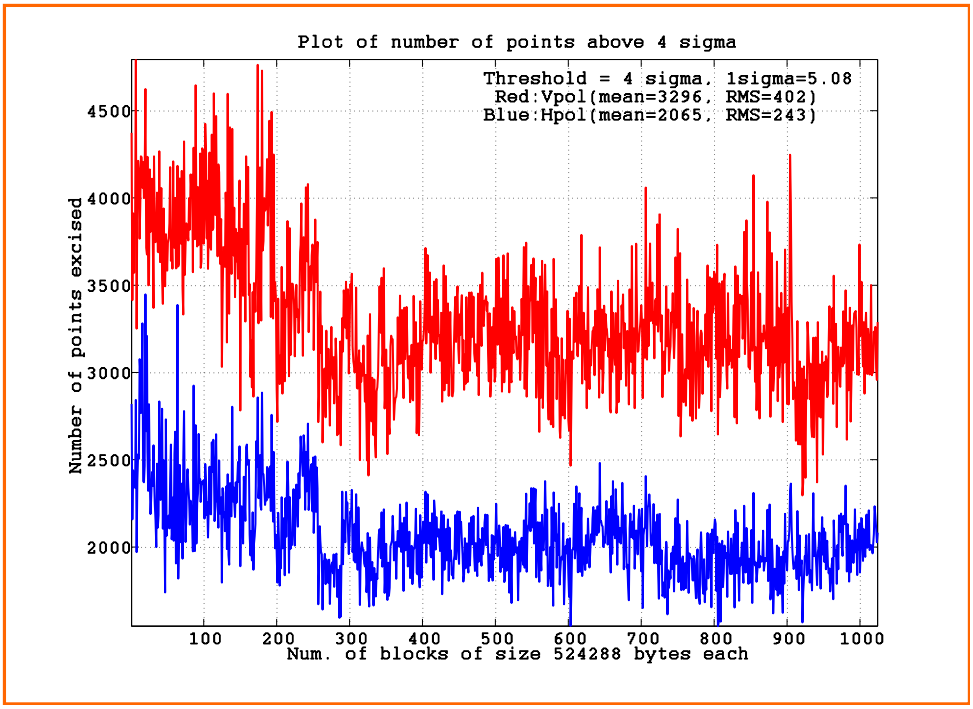

Figure 4-11: A plot of number of points above 4σ threshold.

Figure 4-11 shows a plot of number of ADC data samples which are above a threshold of 4σ, with 1σ ≈ 5 ADC counts. On the average, about 3000 data samples from each block containing 524288 data samples, are above the threshold implying that about 1% of the acquired data is >4σ threshold.

After thresholding, the data sets from the two antennas are cross-correlated and the correlation coefficient as a function of frequency is computed. The expected correlation coefficient for Cygnus A can be computed from equation (4.2):

$$\rho_{source} \cong \frac{\eta T_{source}}{T_{source} + T_{bck} + T_{rx}} \tag{4.2}$$

where,

T_{source} : is the source temperature = 11, 600 K for Cygnus A at 50 MHz,

T_{bck} : is the background temperature = 10,300 K at 50 MHz,

T_{Rx} : is the receiver temperature = 250 K, and

η : is the efficiency of GMRT antenna at 50 MHz = 0.65. At the time of installation of the V-dipoles, the efficiency of GMRT antennas, at 50 MHz, was measured to be around 65%.

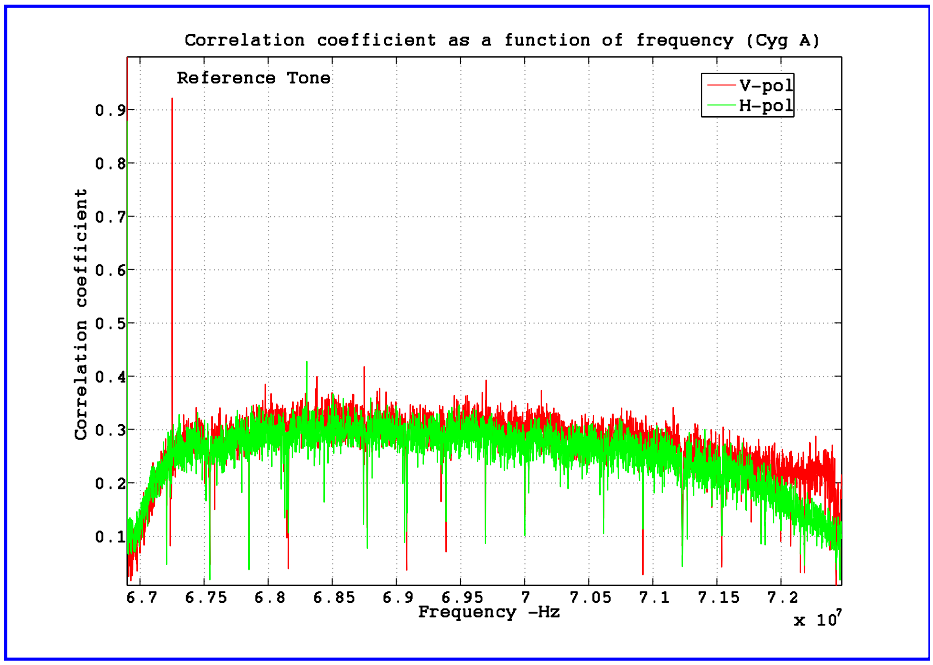

Figure 4-12: Correlation coefficient as a function of frequency for Cygnus A.

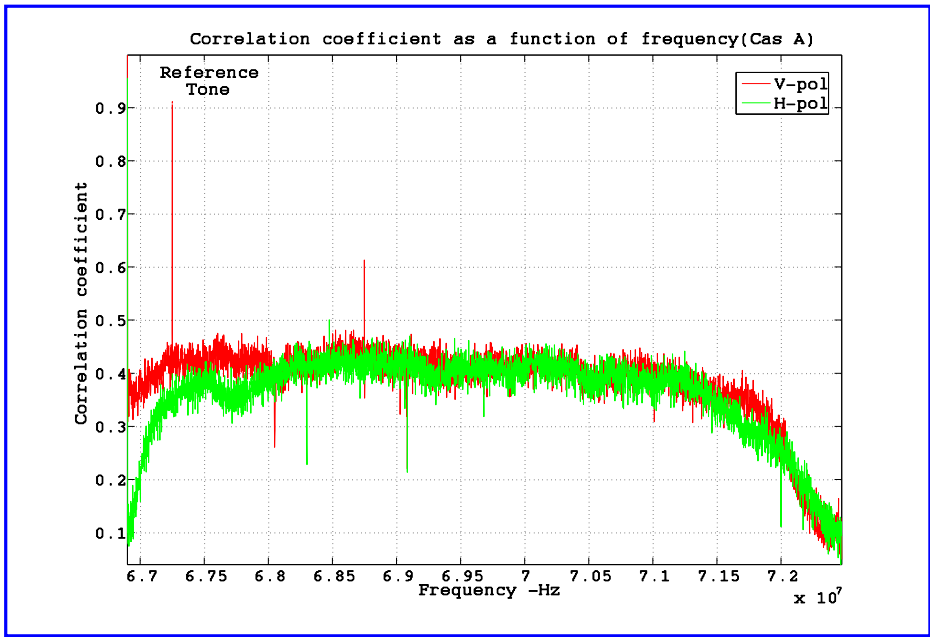

Figure 4-13: Correlation coefficient as a function of frequency for Cas A.

The values for $T_{source} = 11600\text{K}$ and $T_{bck} = 10300\text{K}$ are obtained from Baars *et al.* [26], the expected correlation coefficient (using equation (4.2)) is

$$\rho_{\text{exp}} \cong \frac{0.65*11600}{11600+10300+250} = 0.34$$

A plot of normalized correlation coefficient as a function of frequency obtained for Cygnus A, using the RRI-DS, is shown in Figure 4-12. A correlation coefficient of ~0.32 is obtained

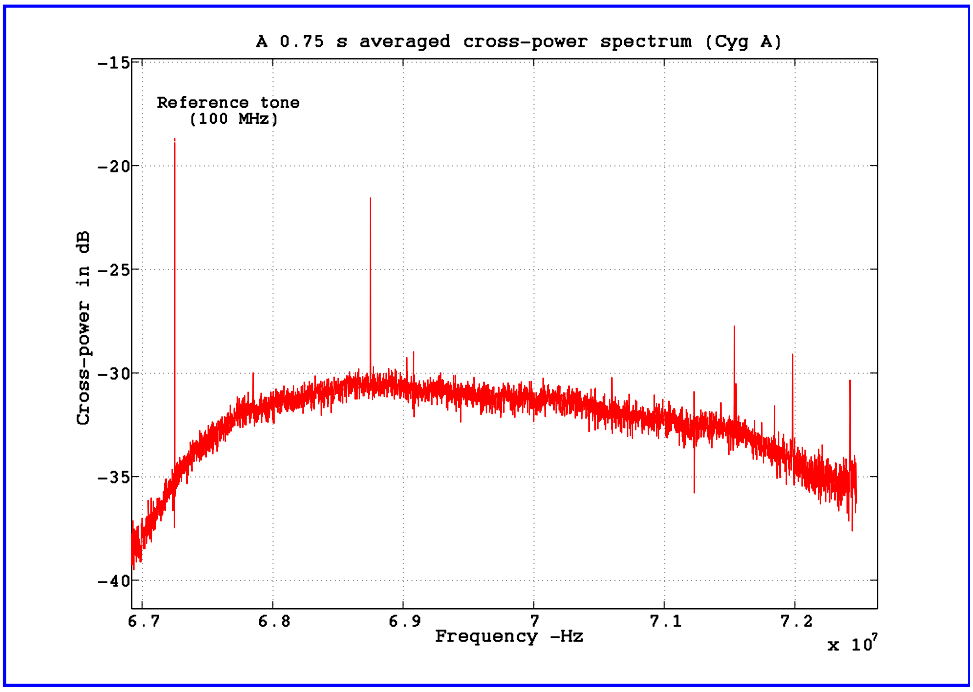

Figure 4-14: A ~1s averaged cross-power spectrum (Cygnus A).

(within the 3-dB passband of the spectrum) which is consistent with that obtained from the above equation (4.2). For the phase coherent 100 MHz reference tone, a correlation coefficient of 0.925 is obtained.

From Baars *et al*. [26], the equivalent values of T_{source} and T_{bck} for Cas A are 16300 K and 9100 K, respectively, which provides an expected correlation coefficient, $\rho_{source} \cong 0.41$. A plot of normalized correlation coefficient as a function of frequency obtained for Cas A, using the RRI-DS, is as shown in Figure 4-13. A correlation coefficient of ~0.4 is obtained (within the 3-dB passband of the spectrum) which is consistent with that obtained using equation (4.2). For the phase coherent 100 MHz reference tone, a correlation coefficient of 0.91 is obtained.

The FFT bin-wise cross-correlation of time-aligned signals from the two antennas produces a complex output signal. While Figure 4-14 shows a ~1s averaged cross-power spectrum, Figure 4-15 shows a plot of the unwrapped phase across the central 2048 spectral channels. A linear fit to the unwrapped phase values for the entire band shows a gradient of 0.53 radians per channel (30.36°) and a *y*-intercept of 0.61 radians. So, the number of complete 360° cycles present in the entire 5.575 MHz band is

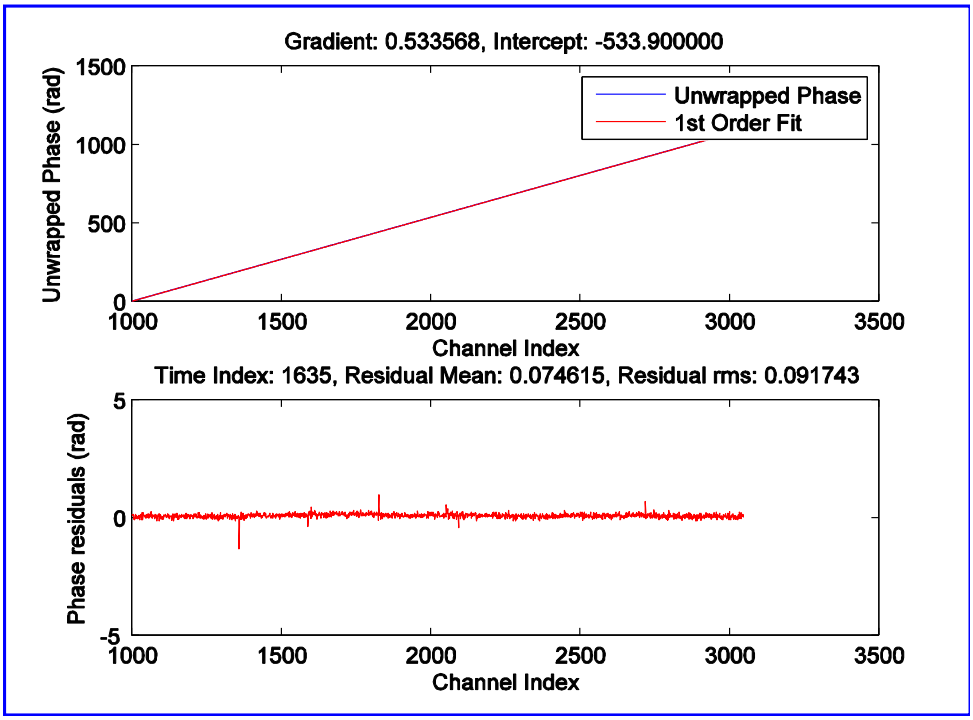

Figure 4-15: A plot of unwrapped phase as a function of frequency (top) for the central 2048 spectral channels and phase residuals after linear fit (bottom) for the ~1s averaged cross-power signal.

$$\frac{30.36*4096}{360} = \frac{1.2438*10^5}{360} = 345.5$$

Time period of a signal (one cycle) is the time taken by that signal to undergo a total phase change of 360°. One cycle of 360° for a bandwidth of 5.575 MHz is $\frac{1}{5.575*10^5} = 0.179\mu s$. Therefore, the total time delay due to 345.5 cycles is $345.5*0.179\mu s = 61.97\mu s$. This delay of $61.97\mu s$ corresponds to a delay which has not been compensated before cross-correlation. Figure 4-15 also shows a plot of the phase residuals after a linear fit to the unwrapped phase, again for the central 2048 spectral channels (1001 to 3048 spectral channels).

4.2.2 RFI Detection and Mitigation

Astronomical signals are typically very weak and signal processing is required both to improve their sensitivity and to enable astronomers to extract meaningful information from them. As is evident in the description of various receivers for radio astronomy, the signal processing involved in improving the signal-to-noise ratio of the collected signal are: sampling, quantization and correlating the signal. With rapid improvements in aspects related to design of antennas and receiver parameters, high-sensitivity modern radio telescopes are

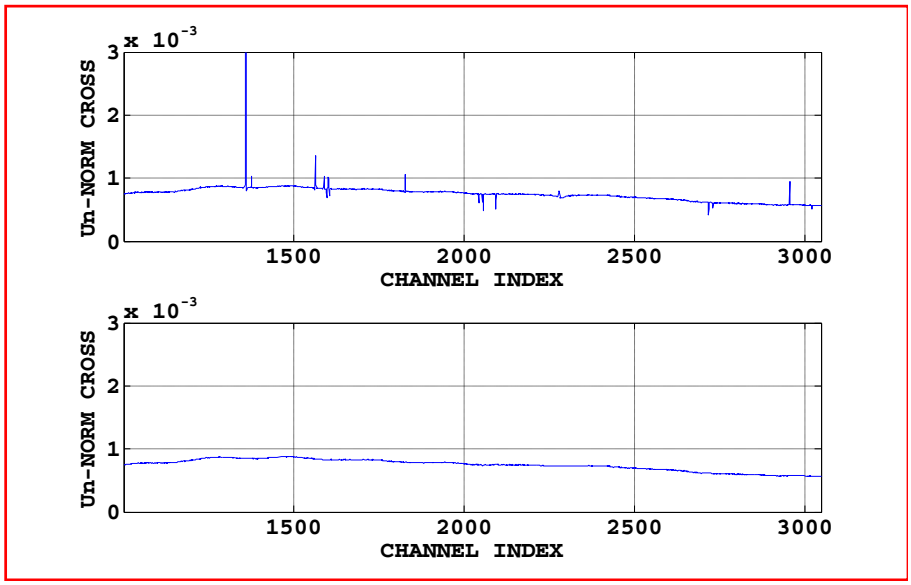

Figure 4-16: A plot of ~4m averaged cross-power spectral density before and after median filtering.

geared up to lower the detection levels. However, it has become difficult to attain the full sensitivity of a radio telescope, particularly at low frequencies (< 1GHz), because of their vulnerability to man-made radio frequency interference originating from various telecommunication systems. While it is difficult to avoid RFI altogether, its enormity can be reduced to a large extent by locating sensitive radio telescope in isolated, radio-quiet zones. Signals from satellites can leak into protected radio astronomy bands, and the problem is likely increase as more satellites are put into orbit. Low Earth-orbit satellites (LEOs) create an RFI problem no matter where on Earth a radio telescope is located.

Given the scenario, radio astronomers are left with no other options apart from developing RFI mitigation methods for astronomy. There is no universal method of RFI mitigation in radio astronomy. The methodology for RFI mitigation depends on type of radio telescope, type of observation and importantly on the type of RFI. RFI can be impulse-like burst, narrowband or broadband. RFI mitigation methods shall be more effective with stronger signals while it becomes increasingly difficult to detect and mitigate weaker RFI signals in the astronomical data. However, the efficiency of the mitigating technique (algorithm) is related to the quality of the acquired data. The receiver systems that provide the astronomical data must be linear enough to prevent any spread of strong interferences and must have sufficient spectral resolution to extract radio astronomical information between

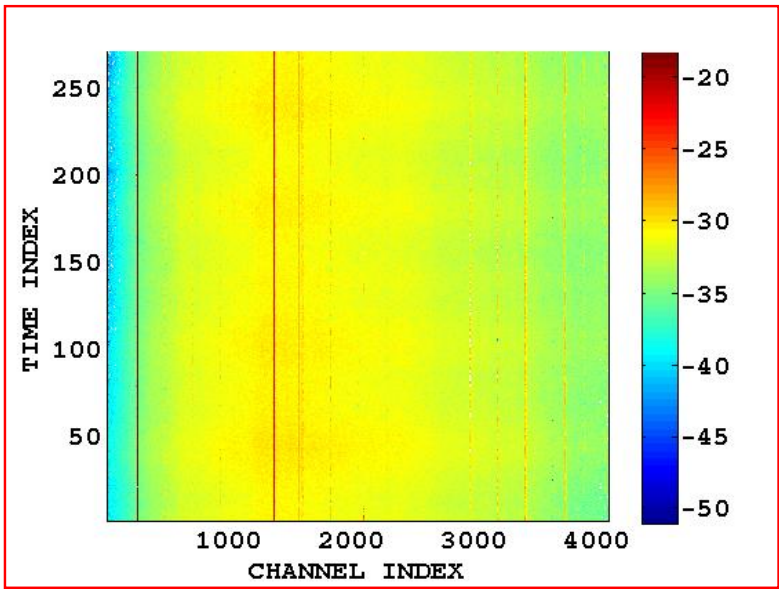

Figure 4-17: A dynamic spectra of ~1 s averaged cross-power spectrum from $\mathbf{V_1 x V_2^*}$.

interference lines. So, receivers for radio astronomical applications should have the capability to process wider bandwidth with high dynamic range and spectral resolution.

The methodology followed in detecting and excising RFI in the data acquired from observations at 50 MHz are two-fold: thresholding of time-domain data and suppression in the spectral-domain. Excising interference signals in the temporal domain is most effective when the acquired data contains "spiky" burst of RFI, which is the case with the 50 MHz data shown in Figure 4-10. Any data sample above a certain threshold can be considered to be RFI and is therefore eligible for suppression. From Figure 4-11, we can note that only about 1% of the acquired data set contains such spiky signals (RFI).

However, a weak underlying structure which is also slow-varying is difficult to detect using this thresholding method. Such signals are better suppressed in the spectral domain where a channelization algorithm splits the entire receiver bandwidth into spectral channels, and channels with RFI are suppressed. The procedure that was adopted in processing data acquired from observations carried out at 50 MHz is described in Section 4.2. The first step is to obtain a bandpass template for RFI removal by median filtering ~4 m averaged cross-power spectrum. Figure 4-16 shows a plot of the 4m averaged spectrum before median filtering (top plot) and after median filtering (plot at the bottom). It may be noted that the plots shown in Figure 4-16 contain only the central 2048 spectral channels, ranging from

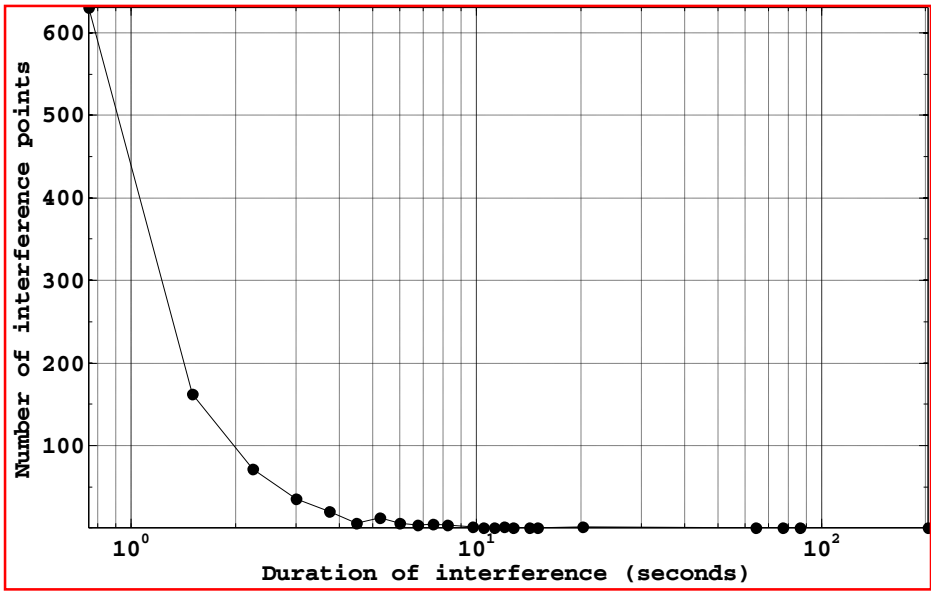

Figure 4-18: A plot of number of interference points versus duration of interference.

1001 to 3048 in the original 4096-point spectrum. The central 2048 spectral channels correspond to the spectral channels within the 3-dB bandwidth of the 5.575 MHz bandpass signal.

Figure 4-17 shows a top-view of the dynamic spectra of ~1s averaged cross-power spectral density obtained from $\mathbf{V_1 x V_2^*}$. The above plot is sometimes referred to as the time-

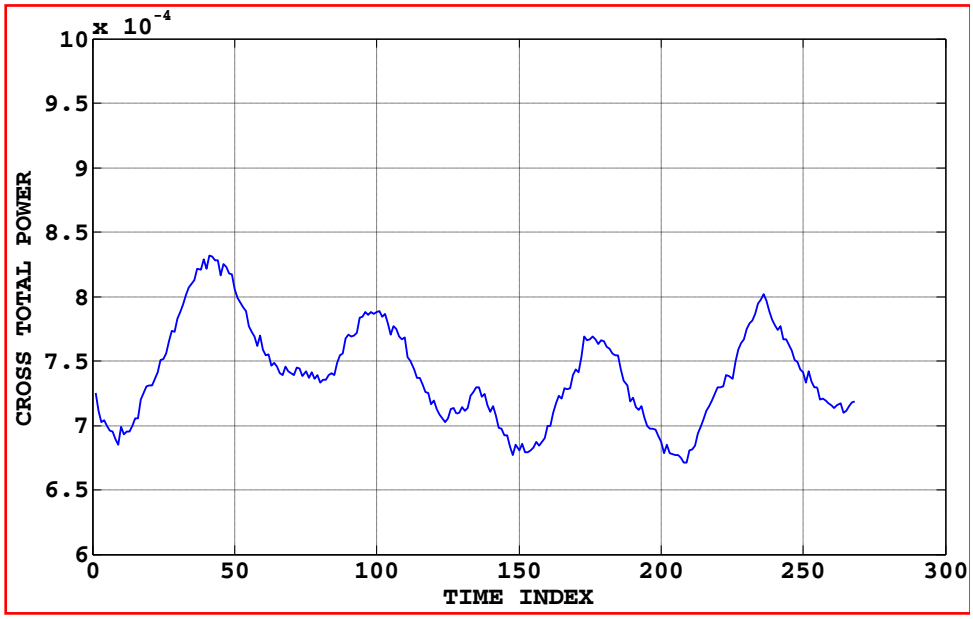

Figure 4-19: A plot of variation in total power in the ~1 s averaged cross-power spectra.

frequency plot. The vertical lines (parallel to the y-axis) seen in the plot correspond to RFI channels present within the 3-dB bandwidth. If a vertical line is continuous along the time index it implies that RFI was present all along for the entire 270 cross-power spectra. On the other hand, a broken vertical line along the time index implies that the RFI was intermittent. The intensity of the spectral channels range from about -50 dB to -20 dB

Figure 4-18 shows a plot of number of RFI points versus the duration for which they were present for the entire time index of 270, 1s averaged cross-power spectra. From the plot it can clearly seen that there are less than about 10 interference points that are present continuously for 10 seconds or more. Figure 4-19 shows a plot of variation of the total power in each of the 270, 1 second averaged cross-power spectra. It is clearly seen that there is a very low-frequency underlying structure with a periodicity of about 45 seconds. This underlying structure is seen at the output of all three correlators: the GMRT-HC, GMRT-SC and the RRI-DS.

4.2.3 Data Analysis for SNR measurement

The visibilities generated by the C-program are further processed by a Matlab routine for excising RFI in the output visibilities and estimating the improvement in signal-to-noise (SNR) as a function of increasing bandwidth (β) and integration time (τ), which is one of the primary objectives of this thesis. The procedure which has been followed in estimating the improvement in SNR is described below:

a) Read the entire visibility data from the visibility output data structure into the Matlab analysis routine. Let $A_i[n]$ be a set of ~1s averaged visibilities read into the data analysis routine, with '*i'* ranging from 1 to N and N being the last visibility in the data set and 'n' is the number of spectral channels in each A_i, which is 4096.
b) Collapse 4096 cross-power density spectra –obtained as magnitude of $A_i[n]$-to obtain a ~4 minutes integrated spectrum, which is then median filtered to remove spiky interference channels to obtain a smoothened bandpass template 'T[n]'. This template is used for flattening the band of each $A_i[n]$ so that an effective RFI detection can be carried out.
c) The individual ~1s averaged cross-power density spectrum is read out sequentially and a zero-mean, band-flattened spectrum B_i is obtained from the equations given below:

$$B_i[n] = \frac{A_i[n] - T[n]}{T[n]} \text{ and } B_i[n] = B_i[n] - mean(B_i)$$

For each $B_i[n]$ any spectral channel which is above a threshold of 4σ is detected and recorded.

d) The phase values across individual A_i visibilities are unwrapped and the phase gradient (refer Figure 4-15) is removed by de-rotating the phases of individual spectral channels for each A_i:

$$C_i[n] = A_i[n] * e^{-j(mn+c)}$$

where, m is the phase gradient, n is the channel number and c is the *y*-intercept.

e) By using the RFI information obtained in step 'c', excise all RFI affected frequency channels in $C_i[n]$ to obtain a new set of visibilities $D_i[k]$, where $k \leq n$. From $D_i[k]$, an estimate of improvement in SNR-in the from of ratio of mean to rms-as a function of number of frequency channels collapsed and time average of visibility frames ($D_i[k]$) collapsed is obtained.

4.3 Signal-to-Noise Ratio (SNR) measurement Results

	GMRT-HC	**GMRT-SC**	**RRI-DS**
Bandwidth (MHz)	8	16	5.5
Spectral Channels	128	512	4096
Spectral Resolution (β in KHz)	62.5	31.25	1.36
Integration Period (τ in seconds)	1	1	0.00073

Table 4-1: Relevant specifications of the three correlator systems under consideration.

In this section, the improvement obtained in the estimation of SNR as a function of integration time and bandwidth from simultaneous observations at 50 MHz carried out using the GMRT hardware correlator (GMRT-HC), GMRT software correlator (GMRT-SC), and the direct voltage recording system (RRI-DS) is described. Table 4-1 compares the relevant specification of the three systems. From equation (4.2) in section 4.2, the expected correlation coefficient for the astronomical source Cygnus A (ρ_{source}) was found to be 0.34. The expected rms noise level is obtained from equation (4.3) as

GMRT-HC

Integration Time / Channel Bandwidth	1s	2s	4s	8s
62.5 kHz (1 Ch)	16.20	17.20	15.52	16.49
125 kHz (2 Ch)	16.28	17.28	15.56	16.53
250 kHz (4 Ch)	16.43	17.45	15.66	16.65
500 kHz (8 Ch)	16.92	18.06	16.05	17.15

GMRT-SC

Integration Time / Channel Bandwidth	1s	2s	4s	8s
31.25 kHz (1 Ch)	19.93	20.00	20.26	20.32
62.5 kHz (2 Ch)	20.20	20.17	20.38	20.40
125 kHz (4 Ch)	20.37	20.24	20.56	20.55
250 kHz (8 Ch)	20.73	20.62	20.96	21.07

RRI-DS

Integration Time / Channel Bandwidth	1s	2s	4s	8s
1.36 kHz (1 Ch)	13.18	16.84	20.34	23.13
2.72 kHz (2 Ch)	16.84	20.34	23.17	25.06
5.44 kHz (4 Ch)	20.31	23.09	25.11	26.31
10.88 kHz (8 Ch)	23.4	25.33	26.75	27.45

Table 4-2: Improvement in SNR when the low-frequency underlying structure is not removed.

$$\Delta\rho \cong \frac{1}{\sqrt{2\beta\tau}} \tag{4.3}$$

where, β is spectral resolution and τ is the coherent integration period. For RRI-DS, rms noise is $\Delta\rho \cong \frac{1}{\sqrt{2*1.36e3*0.75}} = 0.022.$

The expected signal-to-noise ratio for Cygnus A using RRI-DS is obtained as

$$\frac{\rho_{source}}{\Delta\rho} = \frac{0.34}{0.022} = 15.4.$$

This is similar to the SNR of 14.92 measured using RRI-DS (refer Table 4.3).

Table 4-2 shows the improvement in SNR as a function of increasing β and τ when the underlying low-frequency structure (shown in Figure 4-19) is not removed.

GMRT-HC

Integration Time / Channel Bandwidth	1s	2s	4s	8s
62.5 kHz (1 Ch)	41.54	39.05	43.49	54.73
125 kHz (2 Ch)	42.69	39.26	43.78	54.94
250 kHz (4 Ch)	43.53	39.29	44.27	55.05
500 kHz (8 Ch)	45.01	39.47	45.04	55.25

GMRT-SC

Integration Time / Channel Bandwidth	1s	2s	4s	8s
31.25 kHz (1 Ch)	60.87	66.32	80.76	79.03
62.5 kHz (2 Ch)	67.70	72.03	86.07	82.94
125 kHz (4 Ch)	75.15	77.29	88.25	85.28
250 kHz (8 Ch)	75.48	75.91	86.89	83.63

RRI-DS

Integration Time / Cannel Bandwidth	1s	2s	4s	8s
1.36 kHz (1 Ch)	14.92	21.07	29.40	41.14
2.72 kHz (2 Ch)	21.09	29.57	41.09	56.42
5.44 kHz (4 Ch)	29.66	40.96	56.34	76.03
10.88 kHz (8 Ch)	40.89	55.9	74.69	96.93

Table 4-3: Improvement obtained in SNR when the underlying structure is removed.

From Table 4-2, it is clearly seen that without removal of the underlying structure, improvement in SNR as function of β and τ in the case of GMRT-HC and GMRT-SC does not proceed on expected lines. In case of GMRT-HC, the SNR improvement for 8 timeframes and 8 spectral channels collapse should have been $\sqrt{8*8}=8$ times the SNR for one time frame and one channel, i.e., $8*16.20=129.6$, but it is only 17.15, down by a factor of about 7.5. The expected SNR improvement in the case of GMRT-SC for 8 timeframes and 8 channels collapse is down by a factor of 7.56. In the case of RRI-DS, the SNR improvement factor is off only by a factor of 3.85. Table 4-3 shows the improvement obtained in SNR when the underlying structure is removed before collapsing channels and timeframes.

Time frames Integrated	GMRT-HC				GMRT-SC				RRI-DS			
	Channel BW – kHz				Channel BW – kHz				Channel BW – kHz			
	62.5	125	250	500	62.5	125	250	500	62.5	125	250	500
1	41.5	39.0	43.4	54.7	66.3	80.7	79.0	115.5	87.8	114.0	150.7	175.4
2	42.6	39.2	43.7	54.9	72.0	86.0	82.9	118.8	109.2	143.3	173.1	190.7
4	43.5	39.2	44.2	55.0	77.2	88.2	85.2	114.8	129.4	173.1	187.2	206.7
8	45.0	39.4	45.0	55.2	75.9	86.8	83.6	105.8	148.6	189.3	198.6	215.2

Table 4-4: Comparison of SNR measurements for all three correlator systems.

From Table 4-3, it is seen that with the removal of the underlying low frequency structure, improvement in SNR as function of β and τ in the case of GMRT-HC and GMRT-SC is better when compared to Table 4-2, although it still does not provide the improvement in SNR on expected lines. However, it must be noticed that in the case of GMRT-HC and GMRT-SC, even though improvement in SNR as a function of β and τ is not on expected lines, there is a significant improvement in the values of individual SNRs. In case of GMRT-HC, the SNR improvement for 8 timeframes and 8 spectral channels collapse should have been $8 * 41.54 = 332.32$, but, it is only 55.25, down by a factor of about 6. The expected SNR improvement in the case of GMRT-SC for 8 timeframes and 8 channels collapse is down by a factor of 5.8. In the case of RRI-DS, the SNR improvement factor is off only by a factor of 1.23. This factor of 1.23 is much lower than the corresponding value of 3.85 obtained when the underlying low frequency variation is not removed.

As mentioned in Table 4-1, the spectral resolution of GMRT-HC is 62.5 kHz, GMRT-SC is 31.25 kHz and that of RRI-DS is 1.36 kHz. Table 4-4 compares the SNR measurements by bringing all three correlator systems to common platform in terms of number of channels collapsed β and timeframes integrated τ. The SNR values are computed after removing the underlying low frequency structure. For example, to compare the SNR obtained from GMRT-SC with that of GMRT-HC for a single timeframe of 1s and a spectral channel, two adjacent spectral channels of GMRT-SC are collapsed in order to make the spectral resolutions of the two correlator systems identical. Similarly, in order to compare the SNR obtained from RRI-DS with that GMRT-HC for a single timeframe of ~1s and a

spectral channel, $\frac{62.5*10^3}{1.36*10^3} \approx 46$ spectral channels of RRI-DS are collapsed. From Table 4-4, it is seen that the value of SNR for GMRT-HC varies from 41.5 (1 spectral channel, 1 timeframe) to 55.2 (8 spectral channels and 8 timeframes collapsed), which is an improvement only by a factor of 1.33 as against an expected SNR improvement factor of 8. The corresponding SNR values for the GMRT-SC are: 66.3, 105.8, measured SNR improvement factor of only 1.6 as against an expected improvement factor of 8. For the RRI-DS, the corresponding SNR values are: 87.8 and 215.2, measure SNR improvement factor of only 2.45 as against an expected improvement factor of 8. The factor of 2.45 obtained for RRI-DS as against a factor of 1.33 obtained for GMRT-HC and 1.6 obtained for GMRT-SC clearly suggests that there is an advantage in digitizing RF/IF signals at the antenna base itself as was done with RRI-DS. As mentioned earlier, for the RRI-DS, not only is there an improvement in SNR as function of β and τ, it is clearly seen that the individual SNR values itself for various β and τ are better compared to that of GMRT-HC and GMRT-SC.

4.4 Summary of the 50 MHz observations carried out at GMRT

This section presents a review of the results obtained from simultaneous observation of astronomical sources using all three correlators: GMRT-HC, GMRT-SC and RRI-DS. It may be recalled that RRI-DS digitized and recorded voltages right at the antenna base while the other two correlators processed signals at the central electronics building after being transported on an analog optic fiber link from the antenna base. From the results tabulated in Table 4.3, it is clearly seen that the removal of the low-frequency underlying structure helps in obtaining a better SNR with all three correlators than when the underlying structure is present (Table 4.2). However, in spite of removing the underlying low-frequency structure (whose periodicity is about 45 s), all three correlators do not show the expected improvement in SNR for time-frame and channel collapse. There is a clear indication of saturation of SNR in all correlator systems. Table 4-4 which compares the SNR measurements of all three correlator systems by bringing them on to a common platform in terms of channel bandwidth and time-frames collapsed, it is clear that there is approximately a factor of $\sqrt{2}$ improvement in SNR going from GMRT-SC to RRI-DS. Likewise, there is a factor of 2 improvement in SNR going from GMRT-HC to RRI-DS. The factor of 2 and $\sqrt{2}$ improvements in SNR is quite significant from the point of view of telescope time required to reach a given

sensitivity. The available observation time at any telescope is always at a premium. Considering this, even a factor of 2 improvement in SNR going from GMRT-HC to RRI-DS, can significantly reduce the observation time to reach a given sensitivity. Clearly, it is advantageous to digitize data right at the antenna base and transport digitized data to a central processing station. But this calls for a developmental activity involving optical fibers, digital data transmission, which can be involved, both cost-wise as well as from the human resources point of view. However, the viability of digitizing signals right at the antenna base may be considered whenever GMRT plans to go in for a system upgrade

Chapter 5

Chapter 5

Conclusion

5.1 Thesis Summary

In Chapter 1, beginning with a brief introduction to radio astronomy, various digital correlation receivers for single-dish and antenna arrays for radio astronomy were presented in order to lay the groundwork for the two major objectives of this thesis: design and development of a 320 MHz autocorrelation spectrometer for the RRI 10.4m radio telescope, and development of a direct voltage recording system for 50 MHz observations at GMRT to test the feasibility of digitizing RF/IF signals at the antenna base.

The spectrometer for the RRI 10.4m radio telescope is built around 2-bit correlator ASIC from NASA. This instrument in its narrow bandwidth, high spectral resolution mode served as the back-end receiver for Methanol maser survey.

These days, there is a renewed interest in pursuing observations at low frequencies with new state-of-the-art ground-based arrays. However, low-frequency radio astronomy encounters a great number of challenges like: achieving higher angular resolution given the fixed aperture and baseline, building high dynamic range receivers so that observations can be carried out in the presence of radio frequency interference (RFI) with intensities much higher than the radio emission from the astronomical source. The Giant Metrewave Radio Telescope (GMRT), which is located near Pune in India, is the world's largest array of radio telescopes at metre wavelengths. Observations carried out at GMRT showed that $\sqrt{\beta\tau}$ improvement was not forthcoming when observed using the existing GMRT receiver chain. So, a direct voltage recording system was developed to study the improvement obtained in signal-to-noise ratio (SNR) as a function of bandwidth and integration time, by digitizing RF/IF signal right at the antenna base. This was a part of RRI's involvement in designing and developing a 50 MHz receiver system for GMRT.

The Section-A of Chapter 2 contains a detailed description of the aspects that went into the design and development of a hybrid wideband (320 MHz) autocorrelation spectrometer. Additionally, it also details the integration of the spectrometer with other sub-systems of the 10.4 radio telescope, for carrying out methanol maser-line survey in the Galactic plane. Chapter 2 also contains illustrations of functioning of the spectrometer in high-resolution narrow band mode and coarse resolution broadband mode by carrying out actual observations of astronomical sources (maser-line sources from the ultra compact HII region). Later, Section-B of Chapter 2 describes the realization of the concept of direct digitization of RF signal in the L-band. An ADC capable of digitizing analog signals in the L-band was interfaced directly to the correlator section of the hybrid wideband spectrometer, there by, doing away with a couple of analog downconversion stages. Section-B also describes the considerations that go into choosing an ADC for high-speed applications.

Major considerations that go into the design of a digital recording system have been described in detail in Chapter 3, especially, the crucial synchronization of the two recording systems which are physically separated by a few kilometers. The main motivation for conducting this experiment was to understand the improvement that can be obtained in SNR- as a function of bandwidth and integration time- by digitizing signals at the antenna base. Additionally, we wanted to understand the requirements of a low-frequency receiver system for GMRT considering the RFI environment at low frequencies. The results obtained from the direct voltage recording system were compared with those obtained from two other existing GMRT backend receivers housed at the central electronics building. In addition to digitization of signals right at the antenna base, the recording of raw voltages and processing them in software turned out to be advantageous as we could carry out RFI mitigation in time-domain and frequency-domain at various stages of processing. Once the presence of an underlying structure with a periodicity of ~45s was detected, processing of recorded voltages in software allowed us to remove it at the basic integration level of ~1s before collapsing channels and time-frames to obtain an improvement in SNR. For the first time, we could see visibility structures at GMRT with unprecedented time and spectral resolution, in spite of the presence of strong RFI. Also, as is evident from Table 4.4 in which the SNR obtained from the three correlators are compared, the signals recorded at the antenna base seem to be least affected by external factors than the signals processed at the central electronics building. This

study has opened up the possibility of digitizing signals right at the antenna base in the new upgrade for GMRT.

5.2 Looking ahead

5.2.1 Multi-Resolution RFI Detection and Mitigation Strategy

Radio astronomy at low frequencies (typically, less than 1 GHz) is increasingly witnessing pollution due to man-made radio frequency interference (RFI). The nature of RFI varies from intense and short bursts (spiky) to low-lying and continuous, in time-frequency domain. While there may not be sufficient SNR to clearly identify an RFI affected channel at low time integrations, too high an integration period can average out the RFI in a spectral channel if the RFI is intermittent. So, it is difficult to prescribe a time resolution δt and/or spectral resolution δf for detection of all possible types of RFI in the data. So, a multi-resolution RFI detection and mitigation strategy will be useful to process data acquired from two GMRT dishes in which the optimal time-resolution and spectral resolution in terms of the best SNR obtained can be arrived at. A scheme based on such an optimal filtering similar to "matched filtering" is under development. This will concepts in decision based filtering theory.

5.2.2 A Hybrid FX Correlator

Correlators which have traditionally been built around ASICs are being replaced with FPGAs. An alternative to customized hardware has been to develop software which carries out correlations on non-application specific hardware. An intermediate approach consisting of a software framework with hardware-specific optimized plug-in, referred to as a hybrid correlator, is being tried out. The idea here is to implement the Fourier transform (F) portion on an FPGA and realize the cross-multiplication (X) portion in software. Such a hybrid correlator is being increasing used by the radio astronomy community.

Appendix A

Appendix B

This thesis contains an accompanying Compact Disc (CD-ROM), containing software that has been developed as part of the thesis work. The CD contains three sub-directories:

1) Software: contains programs that have been developed as part of the thesis work, along with a read-me file describing the procedure to compile the listed programs. The read-me file also contains details of the computer hardware/software requirements to execute the programs.
2) Hardware: contains schematics of all the boards/modules mentioned in Appendix A, along with detailed datasheets of major components used in the circuit.
3) References: contains soft copy of some of the references listed in the bibliography section of this thesis.

Finally, a soft copy of the entire thesis is available in a Portable Document Format (PDF) titled “BSG_MScThesis.pdf.”

Bibliography

1. J.D. Krauss, "Radio Astronomy," McGraw-Hill Book Company.
2. J.N. Chengalur, Y. Gupta and K.S. Dwarakanath, "Low frequency Radio Astronomy," Third edition, National Centre for Radio Astrophysics, Tata Institute of Fundamental Research, Pune, India, 2007.
3. B.F. Burke and F. Graham-Smith, "An Introduction to Radio Astronomy," Second edition, Cambridge University Press, 2002.
4. J. Hagen, "Spectrometry and Autocorrelation", *ASP conference Series*, Vol. 278, 2002.
5. J.B. Hagen, D.T. Farley, "Digital Correlation techniques in radio science," *Radio Science*, Vol. 8, No. 8,9, pp. 775-784, Aug-Sep, 1973.
6. J.H. Van Vleck and D. Middleton, "The Spectrum of Clipped Noise," *Proceeding of the IEEE*, Vol. 54, No.1, January 1966.
7. J.B. Hagen, "Applications of Correlator Chips in Radio Science,**"** *4th NASA symposium on VLSI design*.
8. J.A. Wepman, "Analog-to-digital converters and their applications in radio receivers," *IEEE Communications Magazine*, Vol.33, pp. 39-45, May 1995.
9. A.R. Thompson, J.M. Moran, G.W. Swenson, "Interferometry and Synthesis in Radio Astronomy," John Wiley and sons, Inc., 2001.
10. Marcello Felli and Ralph E. Spencer, "Very Long Baseline Interferometry: Techniques and applications," *NATO Advanced Science Institute series*, 1988.
11. J.D. Bunton, "Implementing Correlators for the SKA," *Proceedings of workshop on application of radio science (WARS-2002)*, Australia.
12. A.T. Deller, S.J. Tingay, M. Bailes and C. West, "DiFX: A Software Correlator for Very Long Baseline Interferometry Using Multiprocessor Computing Environments,**"** *Publications of the Astronomical Society of the Pacific*, 119: 318–336, 2007 March.
13. S. Weinreb, "Analog-Filter Digital-Correlator Hybrid Spectrometer," *IEEE transactions on Instrumentation and Measurement*, IM-34, No. 4, December 1985.
14. L.R. D'Addario, A.R. Thompson, F.R. Schwab and J. Granlund, "Complex cross-correlators with three-level quantization," *Radio Science*, Vol.19, No. 3, pp. 931-945, May-June 1984.

15. F.K. Bowers and R.J. Klinger, "Quantization noise of correlation spectrometers," *Astron. Astrophys. Suppl.*, 15, pp. 373-380, 1974.
16. High Performance CMOS correlator, *Product specification, NASA SERC for VLSI systems design*, Univ. of New Mexico, Albuquerque, NM. http://www.naic.edu/~astro/general_info/correlator/cmos.html
17. F. J. Harris, "On the Use of Windows for Harmonic Analysis with the Discrete Fourier Transform," *Proceedings of IEEE*, 66, pp. 51-83, January 1978.
18. FFTW software, www.fftw.org.
19. S.R. Kulkarni and C. Heiles, "How to obtain true correlation from a 3-level digital correlator," *The Astronomical Journal*, Vol. 85, No. 10, October 1980.
20. J. Tsui, "Digital Techniques for Wideband Receivers." Prentice-Hall of India, Second Edition 2005.
21. B. Brannon, "Sampled Systems and the effects of clock phase noise and jitter," *Application Note AN-756*, Analog Devices Inc.
22. R.G. Vaughan, N.L. Scott, and D.R. White, "The theory of bandpass sampling," *IEEE Trans. Signal Processing*, Vol. 39, pp 1973-1984, September 1991.
23. B. Brannon and J. Hall, "Understanding state-of-the-art in ADCs," Ananlog Devices, 2007, www.analog.com/everywhere.
24. N. Gray, "ABCs of ADCs," National Semiconductor, August-2004.
25. GMRT: www.gmrt.ncra.tifr.res.in
26. J.W.M. Baars, R. Genzel, I.I.K. Pauliny-Toth and A. Witzel, "The Absolute Spectrum of Cas A; An Accurate Flux Density Scale and a Set of Secondary Calibrators," *Astronomy and Astrophysics*, 61, 99-106, 1977.
27. H. Johnson and M. Graham, "High-speed digital design: A handbook of black magic," Prentice Hall, 1993.
28. E. Oran Brigham, "Fast Fourier Transform and its applications," Prentice Hall, 1988.
29. R.G. Lyons, "Understanding Digital Signal Processing," Addison-Wesley Publishing Company, 1997.
30. K. Rohlfs and T.L. Wilson, "Tools of Radio Astronomy," Fourth revised edition, Springer.
31. J. Ball, "Radio astronomical data acquisition," *Haystack Radio Astronomy notes*. http://www.haystack.mit.edu/edu/undergrad/materials/NotRA4.pdf